CHARACTERIZATION OF DYNAMIC AND FUNCTIONAL NUCLEIC ACID BASED SYSTEMS

by

Damian Beasock

A dissertation submitted to the faculty of
The University of North Carolina at Charlotte
in partial fulfillment of the requirements
for the degree of Doctor of Philosophy in
Nanoscale Science

Charlotte

2023

Approved by:

_____
Dr. Kirill A. Afonin

_____
Dr. M. Brittany Johnson

_____
Dr. Jerry Troutman

_____
Dr. Juan Vivero-Escoto

_____
Dr. Yuri Nesmelov

ABSTRACT

DAMIAN BEASOCK. Characterization of Dynamic and Functional Nucleic Acid Based Systems. (Under the direction of DR. KIRILL A. AFONIN)

Nucleic acids are highly integrated into molecular biology and exhibit very interesting character. They have immense engineering potential to improve human health and influence molecular systems. Consequently, these biopolymers are the quintessential material for facilitating natural and therapeutic functions in basic research, biomedicine, and biological sciences. Life demonstrates many phenomena of nucleic acids and leaves researchers with tools, challenges, and inspiration. The field of nucleic acid nanotechnology is a massive research endeavor to understand and take advantage of DNA and RNA. Progression of the field is evident with an increasing amount of therapeutic nucleic acids (TNAs) approved for clinical use. Several TNAs such as rationally designed mRNA vaccines, proved to be highly efficient to address the SARS-CoV-2 pandemic. Nucleic acid nanoparticles (NANPs) are an innovative class of structures with novel functional promise. Herein, a review of the field of nucleic acid nanotechnology is given to summarize the potential of the field. The experimental approach aims to contribute versatility and functionality options for NANP based platforms. A novel assembly method of NANPs via selective nuclease degradation of RNA/DNA hybrids is introduced. DNA templated silver nanoclusters, as a new class of therapeutics, are characterized to optimize their antibacterial function. These studies advance the development of functional nucleic acids for the treatment of diseases and the improvement of human health.

ACKNOWLEDGMENTS

I would like to express my sincere gratitude to my mentor, Dr. Kirill Afonin, for his guidance and support throughout my time in this lab. His expertise and insights were invaluable, and I am grateful for the opportunity to be a part of the lab. I would also like to thank my committee members, Dr. Brittany Johnson, Dr. Jerry Troutman, Dr. Juan Vivero-Escoto, and Dr. Yuri Nesmelov, for their thoughtful feedback and suggestions. I am grateful for their guidance and direction in my work.

I am also grateful to my family and friends for their support throughout this process. My parents, Dad and Mom, and my brother, Ben, have always been there for me, and I am so thankful for their love and encouragement. My good friends, Chris and Ciara, have been like a second family to me, and I am so grateful for their support and friendship. I would also like to thank Dr. Martin Panigaj for his support and comical relief.

I am also grateful to Dr. HaiTao Zhang, Dr. Stuart Smith, Dr. Terry Xu, Dr. Yong Zhang, and Dr. Youxing Chen for their assistance and advice. Their expertise was invaluable, and I am grateful for their openness to help. I would like to thank Devin Collins, Jenny Jackson, Laura Smailes, and Paul Wetenhall for the invaluable mentorship in entrepreneurship. I'm forever thankful for Margaret, Kristen, and Tom for the NSF-iCorps experiences as a part of team #1744. The Fort Worth detour was one of our finest moments. I am also grateful to Adam, Anh, Dr. Martins, April, Cat, Dr. Moore, Jessica, and Michael for the amazing experience of being a part of the testing lab and RED team. I learned so much from them, and I am grateful for everything that I learned. From the Chemistry, Engineering, and Optics Departments I would like to thank Dr Adam Fessler, Argjira Rizvanolli, Dr Bernadette Donovan-Merkert, Brenda Fandrey, Cindy Honegger, Frank Green, Geoff

Heacock, Dr Jay Troutman, Dr Jeff Raquet, Dr Josh Tarbutton, Dr Jordan Poler, Dr Konstantinos Falaggis, Dr Lou Deguzman, Dr Mike Mazzola, Nancy Queen, Nataly Tapper, Paul Bainbridge, Rebecca Hawes, and Sam Coleman for all of their much-needed help along the way.

I am also grateful to my fellow graduate students and lab mates, Alex, Corbin, Elizabeth, Jessica, Jim, Jose, Justin H., Justin Z., Lane, Laura, Leyla, Maddy, Manira, Mike, Morgan, Pavi, Pooya, Oleg, Pedram, Rafi, Sabina, Sandra, Sean, Suji, Tang, Varsha, Weina, Yasmine, and Yelixza. I am grateful for the camaraderie.

I would like to thank Anas, Haris, Imam John, Mohamed, Omar E., Omar S., Razak, and Salah for helping me find my way. I am grateful to UNCC Toastmasters members Amrit, Ian, Laria, Lilly, and Kyra for their advice and challenge. Finally, I would like to thank the 5 am Fitness Connection squad for the motivation and encouraging words. Everyone's tenacity was inspiring and motivated me to stay on track. I'll always appreciate the sauna conversation and endless affirmation.

DEDICATION

In loving memory of Raymond M Smith.

TABLE OF CONTENTS

LIST OF FIGURES

CHAPTER 1

CHAPTER 2

LIST OF TABLES

CHAPTER 1

CHAPTER 4

LIST OF ABBREVIATIONS

°C	Degrees Celsius
1D	One dimensional
2D	Two dimensional
3D	Three dimensional
3p-hpRNA	3p-hpRNA 5’ triphosphate hairpin ribonucleic acid
A	Adenine
AA	Acrylamide bisacrylamide
AeL	Wild-type aerolysin
AFM	AFM Atomic force microscopy
Ag	Silver
AgNC	Silver nanocluster
ANOVA	Analysis of variance
AR	ankyrin repeat
ATP	Adenosine triphosphate
AU	Adenine-uracil
bp	Basepair
BRAF	B-Raf gene
C	Cytosine
C11	11 cytosine DNA hairpin
C13	13 cytosine DNA hairpin
C7	7 cytosine DNA hairpin
C9	9 cytosine DNA hairpin

Cl	Chlorine
cm	Centimeter
CO2	Carbon dioxide
CpG	Cytosine-phosphodiester bond-guanine
CRISPR	Clustered regularly interspaced short palindromic repeats
Cryo-EM	Cryogenic electron microscopy
DAMP	Damage-associated molecular pattern
ddiH_2O	Double-deionized water
DLS	Dynamic light scattering
DMEM	Dulbecco's Modified Eagle Medium
DNA	Deoxyribonucleic acid
DNase	Deoxyribonuclease
dsRNA	Double-stranded ribonucleic acid
DTT	Dithiothreitol
EDS	Energy dispersive spectroscopy
EDTA	Ethylenediaminetetraacetic acid
EEM	Excitation-emission matrix spectroscopy
EMSA	Electrophoretic mobility shift assay
EtBr	Ethidium bromide
EtOH	Ethanol
FBS	Fetal bovine serum
FDA	Food and drug administration
FES	Free energy surface

FRET	Förster resonance energy transfer
FSE	Frameshift stimulating elements
G	Guanine
g	Gram
GC	Guanine-cytosine
GFP	Green fluorescent protein
GTP	Guanosine triphosphate
h	Hours
H2O2	Hydrogen peroxide
HEK	Human Embryonic Kidney
HEPES	4-(2-hydroxyethyl)-1-piperazineethanesulfonic acid
IDT	Integrated DNA Technologies
IFN-α	Interferon alpha
IL-12	Interleukin 12
IL-1β	Interleukin one beta
INF	Interaction network fidelity
IRF3	Interferon regulatory factor 3
K	Potassium
kcal	Kilocalorie
keV	Kiloelectron volts
KL	Kissing loop
KOH	Potassium hydroxide
L2K	Lipofectamine 2000

LB	Luria broth
LH	Linker helix
M	Molar
MD	Molecular dynamics
MDR	Multi drug resistant
Mg^{2+}	Magnesium cation
min	Minutes
MIP-1α	Macrophage inflammatory protein-1
mL	Milliliter
mM	Millimolar
mol	Mole
mRNA	Messenger RNA
ms	Millisecond
MTDB	1,4-diazepane derivative 10
MTS	3-(4,5-dimethylthiazol-2-yl)-5-(3-carboxymethoxyphenyl)-2-(4-sulfophenyl)-2Htetrazolium,
MW	Molecular weight
NaCl	Sodium chloride
NANP	Nucleic acid nanoparticle
NAP	Nucleic acid purification
NF-κB	Nuclear factor kappa-light-chain-enhancer of activated B cells
ng	Nanogram
nm	Nanometer

nM	Nanomolar
nm	Nanometer
NMR	Nuclear magnetic resonance
NPT	Isothermal–isobaric
nt	Nucleotide
NUPACK	Nucleic Acid Package
OD	Optical density
ODN	Oligodeoxynucleotide
OH	Hydroxyl
OL3	Olomouc force field 3
ORF	Open reading frame
p	Phosphate
PAGE	Polyacrylamide gel electrophoresis
PAMP	Pathogen-associated molecular pattern
PBMC	Peripheral blood mononuclear cell
PBS	Phosphate-buffered saline
PCR	Polymerase chain reaction
PDB	Protein data base
pN	Piconewton
PRF	Programmed ribosomal frameshifting
PRR	Pattern recognition receptor
ps	Picosecond
QSAR	Quantitative structure-activity relationship

R848	Resiquimod
RAG	RNA-As-Graphs
rcf	Relative centrafugal force
REES	Red edge emission shift
RIG-I	Retinoic acid-inducible gene I
RISC	Ribonucleic acid-induced silencing complex
RMSD	Root mean square deviation
RNA	Ribonucleic acid
RNAi	RNA interference
RNase	Ribonuclease
rNTP	Ribonucleotide triphosphate
RPMI	Roswell Park Memorial Institute
RQ1	RNase quantified
s	Second
S	Entropy
SARS-CoV-2	Severe acute respiratory syndrome coronavirus 2
SAXS	Small angle x-ray scattering
SEAP	Secreted alkaline phosphatase
SEM	Scanning electron microscopy, Standard error of the mean
SHAPE	Selective 2'-Hydroxyl Acylation by Primer Extension
siRNA	Short interfering ribonucleic acid
ssDNA	Single-stranded deoxyribonucleic acid
ssRNA	Single-stranded ribonucleic acid

T	Thymine, Temperature
TIP3P	Transferable intermolecular potential 3P
TLR	Toll-like receptor
TMSD	Toehold mediated strand displacement reaction
TNA	Therapeutic nucleic acid
tRNA	Transfer ribonucleic acid
TRP	Transient receptor potential
Tyr-AARS	Tyrosyl-aminoacyl tRNA synthetase
U	Uracil
UV	Ultraviolet
V	Volts
WAXS	Wide angle x-ray scattering
μg	Microgram
μL	Microliter
μm	Micrometer

1 CHAPTER 1: INTRODUCTION: THE FIELD OF NUCLEIC ACID NANOTECHNOLOGY AND THE POTENTIAL OF NUCLEIC ACID NANOPARTICLES

1.1 Introduction

Nucleic acid nanotechnology is a rapidly growing field that has the potential to provide highly versatile molecular systems with a wide range of functions[1]. Therefore, this potential drives a massive research effort to discover the intricacies of nucleic acids and engineer ingenious solutions that improve the quality of human life. Nucleic acids have the ability to participate in many cellular functions and efficiently regulate them across biological systems. Most are familiar with nucleic acids and their role in the central dogma of molecular biology[2]. DNA is primarily used for the storage and transmission of genetic information in all organisms[3]. RNA is known to arbitrate this stored information for the translation of proteins and regulation of their production. However, the capabilities of these nucleic acids extend beyond these roles, especially for RNA. Most transcribed RNA is not translated into protein. The amount of non-coding RNA is highly correlated with the complexity of an organism. RNA is able to influence and participate in sophisticated interactions with living systems[4, 5]. Both RNA and DNA are essential to the existence and propagation of life[6].

The molecular structure of DNA and RNA defines their chemistry in the functions they carry out. All nucleic acids in general are comprised of the same major components: ribose sugars, negatively charged phosphate groups, and nitrogenous bases[7, 8]. These components are illustrated in Figure 1 The sugar phosphate backbone consists of alternating sugar and phosphate groups that are linked by phosphodiester bonds[9]. The phosphodiester

bonds link the 3' carbon of one sugar molecule to the 5' carbon of the next sugar molecule. The sugar phosphate backbone is a repeating structural element that extends along the entire length of the nucleic acid molecule providing connectivity[10]. The arrangement of the sugar and phosphate groups implies important directionality of nucleic acids by differentiating a 5' end and a 3' end[11]. The phosphate groups contribute a uniform negative charge along the entirety of a single strand. This is the only repulsive force exhibited in the dimer[8]. For nucleic acid in a helical conformation, this is the most apparent factor in electromagnetic interactions in solution at relevant pH values[12].

The sugar phosphate backbone provides a varying degree of mechanical properties and stability depending on its constituents[13]. The backbone alternates between sugar and phosphate and extends for the length of the strand via phosphodiester bonds. The pentose sugar provides connectivity for the attachment of the nitrogenous base. The most prominent variation in nucleic acids is the presence or absence of a hydroxy group at the 2` position; RNA possesses hydroxyl (OH) group while DNA bonds a hydrogen (H)[8]. DNA maintains a stiff helical backbone and a more elastic core relative to RNA[14, 15]. DNA inherently has a high degree of chemical stability, which is congruent with its primary function to preserve genetic information. In contrast, RNA is allowed to be more reactive and flexible. The 2’ hydroxyl can participate in base pairing via C2’ exo conformation[16]. In general, RNA forms an A form helix to minimize steric instability around the hydroxyl group. DNA is most stable in a B form helix. These differences enable RNA to take part in many more functions and biological interactions[17]. The 2' hydroxyl in ribose can form hydrogen bonds with other nucleotides, leading to the formation of RNA secondary structures such as loops and bulges[18]. These structures can act as binding sites for RNA-binding proteins or other RNA

molecules, enabling RNA to regulate gene expression and perform other biological functions[11]. The 2' hydroxyl group also makes RNA more susceptible to hydrolysis of its own phosphodiester by acting as both an intramolecular and intermolecular nucleophile[19]. This likely contributes to RNA's relatively short lifespan compared to DNA. However, this implies that RNA is a highly active molecule and has capabilities beyond passive translation of information. The added complexity and instability make the behavior of RNA much more difficult to predict than DNA[20].

A nitrogenous base is connected to each sugar group of the sugar phosphate backbone. These bases are derivatives of pyrimidine or purine, which are planar nitrogen containing heterocyclic molecules. The nucleobase in nucleic acid is not charged at neutral pH. Available bases differ between DNA and RNA; DNA contains thymine and RNA contains uracil. A typical type of nucleic acid damage is oxidation. A cytosine can spontaneously oxidatively deaminate in water[21, 22]. In this case cytosine is converted into a uracil. Since DNA does not contain uracil, repair mechanisms can identify the damage and the sequence is preserved[23]. Many, but not all noncovalent bonding occurs at this facet of the molecule. Electronegative atoms in the nucleobases act as hydrogen bond acceptors or donors. Atoms with a lone pair can act as a donor and atoms with a covalently bound hydrogen can act as an acceptor[24]. In Watson-Crick base pairing, thymine (T) (or uracil (U) in RNA) and adenine (A) bind with two hydrogen bonds. Cytosine (C) and guanine (G) are more tightly bound, having three hydrogen bonds. Helixes with sequences abundant in GC base pairs have higher melting points due to the higher number of hydrogen bonds[25]. This trend in temperature change is highly consistent in a limited range and can be accurately quantified with the Wallace rule[26]. The nucleobases can absorb light in the ultraviolet (UV)

range. Each base absorbs a spectrum of UV wavelengths and the combined absorption spectrum is centered around a peak near 260 nm[27]. This absorption involves an electron transfer of a nonbonding electron in an aromatic ring to an antibonding orbital known as a π → π* transition[28]. The atomic structure gives nucleic acids their complex properties and allows these macromolecules to take part in very interesting phenomena and functions.

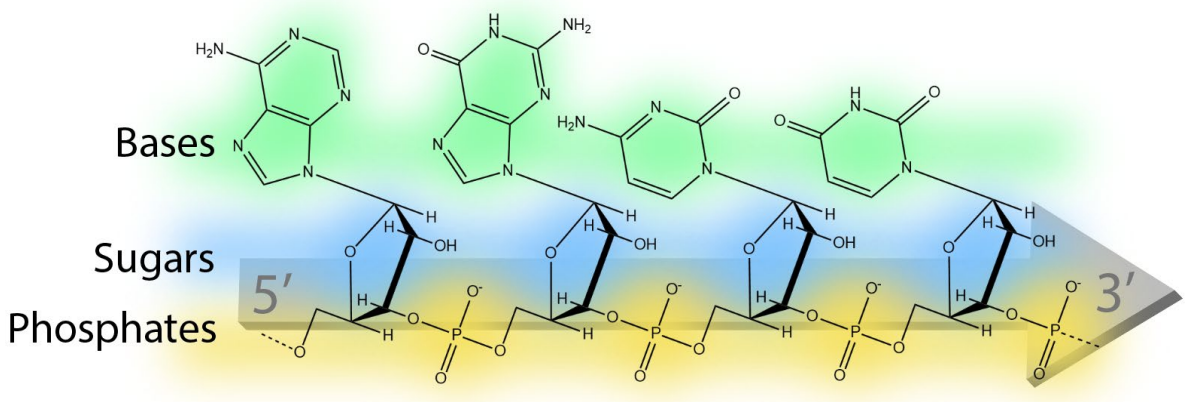

Figure 1. Basic components in RNA. Green bases can consist of nucleotides A, G, C, or U. The sugar (blue) of RNA contains a hydroxyl group at the 2' position and are linked by phosphates (yellow) at the 5' and 3' positions.

1.2 Interaction Forces

Annealing forces are the weak non-covalent interactions between complementary nucleic acid strands. They influence the structure of the molecule and peripheral interactions. The annealing forces that are present in nucleic acid structures include hydrogen bonds, hydrophobic interactions, electrostatic interactions, and Van der Waals forces[29]. The annealing forces in RNA play an especially important role in determining structure, kinetics, and biological function. RNA structures can range from simple monomers to multi-domain structures. Higher order assemblies are enabled by palindromic or complementary sequences that are accessible and stable[30]. RNA annealing can occur between separate molecules within the same strand. The structure determines RNA function as it facilitates the interaction with other molecules, including DNA, proteins, and small molecules[31].

The most distinguishing annealing force in RNA and DNA is hydrogen bonding. The dimerization of nucleic acid is facilitated by hydrogen bonds between the complementary base pairs[32, 33]. Having relatively weak noncovalent interactions in base pairing leave the option for separation of the two complements when needed in cell processes. This feature is also highly advantageous when engineering dynamic assemblies from nucleic acids.

1.3 RNA base pairing

Canonical Watson-Crick base pairing in RNA occurs between A and U or between G and C and follow a set of rules. However, less stable noncanonical base pairing may occur in nucleic acid through combinations of hydrogen bonding and van der Waals interactions[34]. Noncanonical base pairing in RNA enables many functional structures[35]. RNA base pairing can be described using twelve geometric families. Each classification is differentiated by interaction of the base edges and orientation of the glycosidic and hydrogen bonds[34, 36]. The base edges involved shown in Figure 2 are the Watson-Crick edge, the Hoogsteen edge, and the sugar edge. All geometric relationships in RNA base pairing can be summarized with isostericity matrices[37].

These different types of base pairs diversify the possibility of stable structures of RNA. G-U wobble base pair, which occurs when a guanine nucleotide base pairs with an uracil nucleotide. This base pair is highly common in naturally occurring functional RNA molecules and has comparable stability with canonical base pairs. The G-U wobble base pair is commonly found functional RNA structures, including tRNA and rRNA. The G-U wobble base pair is also important for the formation of RNA-protein complexes, where G-U base pairs mediate interactions between RNA and proteins. G and A base pairing is another noncanonical base pair that aids in structure and function of globular RNA molecules[35, 36].

Another common type of noncanonical base pairing is the Hoogsteen base pair. This occurs when there is hydrogen bonding between the purine base and the sugar phosphate backbone and can occur in RNA or DNA[38]. Noncanonical base pairing in RNA allows the stability of many important RNA structures for cellular functions.

Specific RNA sequences allow for a multitude of secondary structures. Many motifs or conserved sequences in nature are employed for functional RNA structures. Hairpins are one of the most common RNA motifs. In a hairpin, single stranded RNA segment anneals with a complementary sequence downrange of the same molecule. This complementary portion forms a stem and the unbound sequence makes up the loop[39]. Bulges, internal loops, and pseudoknots are more complex RNA motifs that assist in and enable RNA functions in biology[40]. Mg^{2+} ions are the most important cations that stabilize many RNA structures by nonspecifically binding to the phosphate backbone and promotes the formation of noncanonical base pairs and secondary structures[24]. The average lifespan of RNA is much shorter than DNA, but it's diversity of functions is immense[41]. The depth of RNA capabilities warrants current research investment.

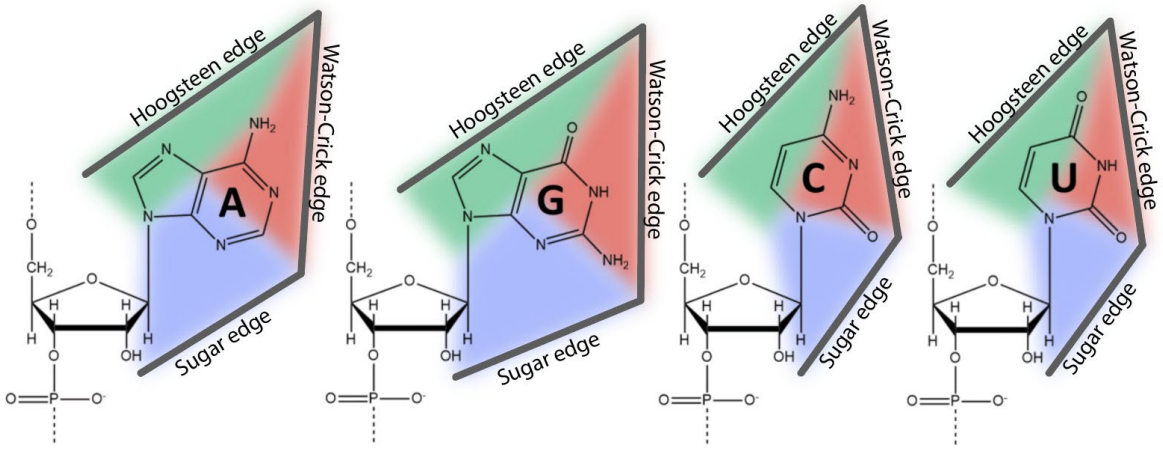

Figure 2. Available edges of RNA that can be involved in base pairing. The flexibility in base pairing enables many stable RNA secondary structures.

1.5 Natural functions of RNA and biomedical potential

The variety of structures of RNA allows for many functions carried out in living systems. RNA naturally is involved with gene regulation, catalytic activity, and cell communication[1, 42-44]. Its ubiquitous use and compatibility in living systems evokes potential in therapeutics.

An RNA molecule is capable of catalyzing the cleavage of its own phosphodiester backbone[45]. A region of the RNA molecule serves as a catalytic site to cleave another region leaving fragments. Hydrolysis of the backbone occurs when a deprotonated hydroxyl group acts as a nucleophile and attacks a phosphorous in a phosphodiester bond. Rate of self-cleavage is dependent on Mg^{2+} ions which aid in the stabilization of the autocatalytic structure confirmation. Self-cleavage can be a form of regulation, used to remove intronic sequences, or release functional RNA sequences from precursors[45].

Ribozymes are functional RNA molecules that catalyze a wide range of chemical reactions. For example, the hammerhead ribozyme is found in viruses and plants and can perform site specific reversible cleavage and ligation reactions[46]. The protein production performed by the ribosome is enabled by the catalytic activity of ribozymes to join amino acids together[47]. Ribozymes are similar to protein enzymes and are specific to substrates but can be much smaller in size. Ribozymes can also catalyze intramolecular cleavage to self-regulate its own activity. Self-splicing introns catalyze their own excision for gene editing and gene regulation[45].

Aptamers are generally short RNA or DNA sequences that are *in vitro* selected to bind specifically to targets, including proteins, small molecules, cells, and bacteria. These molecules have high affinity to specific molecules similar to antibodies[48-50]. From a

therapeutic design perspective, aptamers can be precisely designed, readily produced, and could be compatible with many existing applications[51, 52].

RNA interference (RNAi) is a process in where RNA molecules drive the inhibition of gene expression. Specific mRNA sequences can be targeted for degradation and protein production inhibited[53]. RNAi is mediated by siRNA that is processed from longer RNA precursors by Dicer processing[54, 55]. The siRNA is incorporated the RNA-induced silencing complex (RISC) and used as a guide for specific mRNA molecules with complementary sequences[56]. The mRNA molecule is degraded, and protein expression is inhibited[57]. The versatility of RNA is diverse and highly congruent for developing medical applications.

1.6 Immunorecognition of nucleic acids

One of the most challenging barriers preventing widespread use of functional nucleic acids is the body's immune response to foreign nucleic acids[58-60]. The persistent threat of pathogens required humans to evolve defenses to detect and combat infections. Certain nucleic acids are perceived as an indicator of infection, and this can trigger the immune response in an unproductive or harmful manner[61, 62].

Pattern recognition receptors (PRRs) are a class of receptors that can recognize molecular patterns associated with pathogens or damage to host cells[63, 64]. Pathogen-associated molecular patterns (PAMPs) are foreign molecules that are associated pathogens. Damage-associated molecular patterns (DAMPs) are molecules that are released from damaged or stressed host cells[44, 63, 65-67]. PRRs are expressed on the surface of cells and endosomes throughout the human body. Binding of PRRs to PAMP or DAMP molecules triggers a cascade of events that lead to the activation of an immune response. An important role of the innate immune system is the detection of molecules indicative of abnormalities.

Toll-like receptors (TLRs) are a family of PRRs that are expressed on the surface of cells or on endosomes in the cytoplasm[68]. TLRs recognize a variety of PAMPs, including foreign nucleic acids indicative of pathogens. Detection initiates pathways that cascade to the activation of the innate immune response[69, 70]. The immune system recognizes dsRNA via TLR3[71]. dsRNA is a common intermediate in the replication cycle of many RNA viruses, however some viruses actively prevent immune detection[72]. Viruses such as influenza B that sequester dsRNA are able to mitigate host IFN-β and protein kinase R activation and therefore immune response relies on the detection of ssRNA[73, 74]. TLR7 specifically recognizes ssRNAs which are also characteristic of many RNA viruses[75]. Sequences with successive uridines are correlated with an increase in TLR7 activation[76]. TLR8 also detects ssRNA, this TLR is phylogenetically and structurally similar to TLR7[77]. However, each activates a different response profile[78]. TLR7 agonists more effectively induce IFN-α and IFN-regulated chemokines. TLR8 agonists are more effective for the induction of proinflammatory cytokines and chemokines including MIP-1α, TNF-α, and IL-12[79]. TLR9 detects unmethylated CpG motifs which are found in prokaryotic DNA while not present vertebrate genomes[80, 81]. RIG-I is activated by dsRNA and ssRNA and can differentiate between foreign RNA from natural[82].

Cystolic receptor cGAS is responsible for detecting DNA and stimulates the production of IFN-β. It is typically located in the cell nucleus[83]. RIG-I leads to the activation of transcription factors IRF3 and NF-κB[5]. The detection of foreign nucleic acid initiates signaling pathways where cytokines and chemokines are produced downstream. The production type I interferons and pro-inflammatory cytokines such as interleukin-1β (IL-1β) and tumor necrosis factor-alpha (TNF-α), initiation inflammation and leads to the recruitment

of immune cells to the site of infection and the [63, 84]. The immunorecognition of NANPs is an important factor for the intended application. NANPs are made of nucleic acid molecules much less than 100 nucleotides. The relevant PRR are summarized in table 1[5].

Table 1. Pattern recognition receptors relevant to the immune recognition of NANPs and the activating nucleic acid type.

PRR	cGAS	RIG-I	TLR3	TLR7	TLR8	TLR9
Nucleic Acid	dsDNA, DNA/RNA hybrid	dsRNA	dsRNA	ssRNA dsRNA	ssRNA dsRNA	dsDNA

1.7 Research Approach of Nucleic Acid Nanoparticles

NANPs are a novel class of TNAs that proposes unique advantages and versatility[57, 85, 86]. Complex structures inspired by nature and engineered features can be combined to elicit desired responses and enable functionalities. Some relevant NANP structures are outlined in Figure 3. Therapeutic nucleic acids are a novel form of medicine and have complex interactions in living systems. NANP research takes on many approaches to optimize molecular function, determine safety, develop foundational knowledge, and expedite the translation process[59, 60].

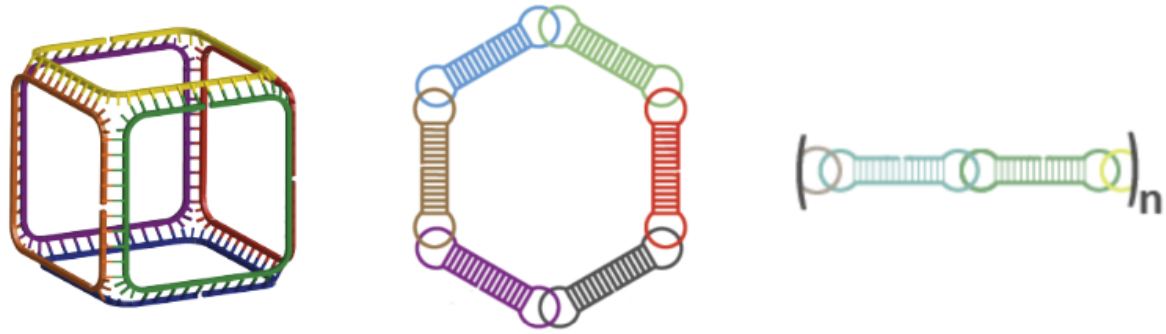

Cubes:
- 3 dimensional
- 6 monomers
- intermolecular bonding

Rings:
- 2 dimensional
- 6 monomers
- inter and intramolecular bonding

Fibers:
- 1 dimensional
- 2 monomers
- inter and intramolecular bonding

Figure 3. Comparison of NANP scaffolds and key differences in structure.

RNA polymers with 2' hydroxyl group enables greater complexity and structure possibilities and therefore is a highly advantageous building material for NANPs. RNA tectonics is a building block approach to designing self-assembling nanostructures out of modular components. RNA units consist of motifs inspired by nature and structures are built in a similar fashion to toy bricks[87]. With developing calculation methods and computational power, software tools have become an increasingly reliable approach to explain and predict RNA structures for NANP design[88, 89]. For example, RNA cubes as therapeutics scaffolds have been designed in silico consisting of 6 or 10 monomers utilizing Watson-Crick base pairing. The design intended a monodisperse solution of self-assembling structures stable at physiological conditions. Proper sequence design mitigates cross talk and ensures thermodynamic stability. Experimental characterization confirmed the successful assembly and validated the computational design approach[90].

RNA rings are a nanoscaffold that offers an array of structure options that enable coordination of multiple functionalities[91]. The scaffold structure involves 6 monomers where each strand holds a functional molecule. The overall structure can offer multiple copies of the

same functional or a unique function for each monomer. Extensive characterization of structures showed successfully assembled and monodispersed solutions of structures[86]. These structures offer nanoscale precision and control. Compatible moieties could include any molecule that is able to bind to an RNA toehold. These include siRNAs, aptamers, and fluorophores[51, 92]. Redundancy of an siRNA sequence on the scaffold significantly increased the silencing capability by increasing the concentration of transfected material. Combining multiple functions on a single scaffold offers capabilities to simultaneously suppress multiple genes or combine therapeutic delivery and targeted delivery into the same platform. Incorporation of fluorophores can enable tracking of and efficiency of delivery methods of treatments[49, 86, 93].

RNA fibers provide low immune response while offering a variety of molecular capabilities[57]. Their utility as a scaffold includes stoichiometric and concentration control of moieties. In addition, the functionalization options encompass many molecules with therapeutic potential. Fibers are made of monomers that fold into dumbbell structures via palindromic sequences. Although these sequences are conserved in all monomers, snap cooling during the assembly process adequately prevents cross talk between monomers in these regions of the sequence[94]. The quaternary structure of fibers is allowed by intermolecular forces in the kissing loop portions of the monomer sequence. These sequences are designed to specifically interact with a compatible complementary loop at a straight angle[95]. Resulting in fibers with alternating monomers and an overall linear structure. If a toehold is introduced, the monomer sequence is extended from the 3’ end after a single stranded 3 uracil linker to mitigate alternative stacking. These structures were successfully functionalized and transfected. Significant knockdown of GFP and mutated BRAF confirmed

the therapeutic viability of a continuous linear assembly. Treatment of PMBCs also indicates low immune recognition despite having an RNA composition.[57] The synergy of minimal immune response and functional programmability indicates profound potential for therapeutic applications.

Immunostimulatory trends have been identified in varied NANP structures as a result of many systematic studies[63, 65, 67]. Therefore, NANPs may be designed with available structures to produce intended immunostimulatory effects. Quantitative structure-activity relationships (QSAR) modeling has been used to determine trends in the immunomodulatory character of NANPs that is defined by physicochemical properties[67]. A set of nanoassemblies were chosen to systematically vary composition and structure. These polygons were run in parallel through an array of experiments and analyses. This effort revealed that composition was the most influential engineering choice regarding functional design; RNA was significantly more immunostimulatory than DNA. The molecule size, melting temperature, and stability showed therapeutic significance. PBMCs and immune reporter cell lines were used in a large systematic immunological assessment of a library of NANPs. This was performed to identify important facets of NANP structure and identify trends to improve the prediction of immune response[65]. The possibility of harmful inflammatory response from TNA's and the uncertainty of NANPs immune recognition prompted the need for mechanistic studies over a wide range of nanostructures[59, 61, 96]. The most probable method of administration of a future NANP therapeutic would be via injection[97]. This suggests that NANPs will interact with many cell types in the body. Cytokine production following treatment of PBMCs more closely replicates the complexity of the adaptive immune system and reveals information more relevant to the adaptive immune system[98]. Reporter cell assays

call for a more standardized environment and primarily inform about intracellular recognition by the innate immune system[98]. The immune results showed significantly different levels of recognition. From the array of data, structure, composition, and complementarity were strong predictors of immune response. Increasing the dimensionality of NANPs was correlated with increased immune response, where 3 dimensional cubes elicited the largest response. RNA NANPs proved highly immunostimulatory while DNA NANPs were more immunoquiescent[5, 43, 63, 65]. Observing trends in NANPs variations provides important insight into safety and more relevant approaches through design.

NANPs have been deployed as a functional system by exploiting the thermodynamics of nucleic acid. Shape switching cubes have been used as a novel strategy to activate multiple biological functions[99]. NANPs were designed where the sequences of structural components for one assembly were complementary to a separate assembly. This scheme coordinated the specific thermodynamic reassociation. An even deeper dimension of design provided consequent functions. Newly materialized structures were capable of RNAi, aptamer functionality, initiating transcription, and FRET. Significant control over the immune stimulation was determined based on the RNA and DNA content of the reciprocal system[99].

Multiple reconfigurable nucleic acid structures have been developed and applied as systems with a therapeutically relevant approach. NANPs can contain split functionalities that may be conditionally activated upon reassociation in the cytoplasm. Functions include RNAi, NF κB decoys, and transcription factors[92]. FRET pairs, quantum dots, or fluorescent aptamers are able to indicate target molecule presence and structure integrity[49, 100, 101]. The presence of target sequences can displace strands and alter fluorescence signals. Aptamers as moieties enable specific binding of target molecules while retaining reversibility functions.

Thrombin can be disabled without denaturation using RNA/DNA hybrid structures. The same structure can also be reversed upon interaction with complementary stands administered as needed[102].

Given the encouraging progress with NANP technology, many barriers remain. Personalized therapeutic approaches are currently limited by safety, functional effectiveness, and availability. The generation of value from TNAs is limited by delivery, storage stability, production costs, and harmful side effects[59, 103].

1.8 Future Directions

Nucleic acids are involved with many diseases and opens the possibility to intervene with TNAs. Many drugs are already approved for clinical use or in clinical trials. Some of these include: Mucagen for age-related macular degeneration (aptamer)[104], Kynamro for familia hypercholesterolemia (antisense oligonucleotide)[105], Givlaari for AHP porphyri[106], Leqvio for LDL-D reduction (siRNA)[107], Covid-19 vaccines (mRNAs)[108], and Amvuttra for TTR polyneuropathy (siRNA)[109]. Personalized medicine entails multifunctional therapeutics with predictable and versatile options. Therefore, the field of nucleic acid nanotechnology must produce a variety of safe and adaptable molecular platforms to meet these requirements[60]. A therapeutic provides no value if the benefit from the primary effect is overshadowed by the side effects. The nature of nucleic acids requires methods to circumvent off target effects. The programmability of NANPs makes this technology a decidedly viable approach for individualized treatments[88, 110-114].

The effort herein contributes to the better therapeutic systems by promoting knowledge, innovating assembly methods to increase versatility, and optimizing moieties to diversify functional options of NANPs. The first work is a review of the field of nucleic acid

nanotechnology. This chapter is an effort to present recent innovations and advocate ideas. The second work presents a novel approach to NANP assembly via nuclease treatment. This approach aims to contribute to the versatility design options of NANPs to control immune recognition and storage stability. The third aim offers a novel antibacterial function to expand the array of available effective functions for future therapeutics. Nucleic acid inherently is a very powerful tool and its translation will require thorough understanding.

1.9 References

1. Guo, Peixuan. The emerging field of RNA nanotechnology. *Nature Nanotechnology* **2010**, *5* (12), 833-842. DOI: 10.1038/nnano.2010.231.

2. Townsend, Leroy B.; Tipson, R. Stuart. Nucleic acid chemistry: Improved and new synthetic procedures, methods, and techniques. 1978.

3. Crick, Francis. Central dogma of molecular biology. *Nature* **1970**, *227* (5258), 561-563.

4. Panigaj, Martin; Skelly, Elizabeth; Beasock, Damian; Marriott, Ian; Johnson, M.; Salotti, Jacqueline; Afonin, Kirill A. Therapeutic immunomodulation by rationally designed nucleic acids and nucleic acid nanoparticles. *Frontiers in Immunology* **2023**, *14*, 370.

5. Johnson, M. Brittany; Chandler, Morgan; Afonin, Kirill A. Nucleic acid nanoparticles (NANPs) as molecular tools to direct desirable and avoid undesirable immunological effects. *Advanced Drug Delivery Reviews* **2021**, *173*, 427-438. DOI: 10.1016/j.addr.2021.04.011.

6. Taft, Ryan J.; Pheasant, Michael; Mattick, John S. The relationship between non-protein-coding DNA and eukaryotic complexity. *BioEssays* **2007**, *29* (3), 288-299. DOI: 10.1002/bies.20544.

7. Saenger, Wolfram. Principles of Nucleic Acid Structure. 1983.

8. Villa, Alessandra. Nucleic Acid Structure. 2020.

9. Watson, J. D.; Crick, F. H. C. Molecular Structure of Nucleic Acids: A Structure for Deoxyribose Nucleic Acid. *Nature* **1953**, *171* (4356), 737-738. DOI: 10.1038/171737a0.

10. D'Atri, V.; Porrini, M.; Rosu, F.; Gabelica, V. Linking molecular models with ion mobility experiments. Illustration with a rigid nucleic acid structure. *J Mass Spectrom* **2015**, *50* (5), 711-726. DOI: 10.1002/jms.3590 From NLM.

11. Huang, M.; Giese, T. J.; Lee, T. S.; York, D. M. Improvement of DNA and RNA Sugar Pucker Profiles from Semiempirical Quantum Methods. *J Chem Theory Comput* **2014**, *10* (4), 1538-1545. DOI: 10.1021/ct401013s From NLM.

12. Šponer, J.; Mládek, A.; Šponer, J. E.; Svozil, D.; Zgarbová, M.; Banáš, P.; Jurečka, P.; Otyepka, M. The DNA and RNA sugar-phosphate backbone emerges as the key player. An overview of quantum-chemical, structural biology and simulation studies. *Phys Chem Chem Phys* **2012**, *14* (44), 15257-15277. DOI: 10.1039/c2cp41987d From NLM.

13. Naskar, Supriyo; Maiti, Prabal K. Mechanical properties of DNA and DNA nanostructures: comparison of atomistic, Martini and oxDNA models. *Journal of Materials Chemistry B* **2021**, *9* (25), 5102-5113.

14. Gore, Jeff; Bryant, Zev; Nöllmann, Marcelo; Le, Mai U; Cozzarelli, Nicholas R; Bustamante, Carlos. DNA overwinds when stretched. *Nature* **2006**, *442* (7104), 836-839.

15. Olsen, Kasper; Bohr, Jakob. The geometrical origin of the strain-twist coupling in double helices. *AIP Advances* **2011**, *1* (1), 012108.

16. Egli, Martin. Sugar Pucker and Nucleic Acid Structure. *The Excitement of Discovery: Selected Papers of Alexander Rich* **2018**.

17. Cheatham, T. E., 3rd; Cieplak, P.; Kollman, P. A. A modified version of the Cornell et al. force field with improved sugar pucker phases and helical repeat. *J Biomol Struct Dyn* **1999**, *16* (4), 845-862. DOI: 10.1080/07391102.1999.10508297 From NLM.

18. Ryan, C. A.; Rahman, M. M.; Kumar, V.; Rozners, E. Triplex-Forming Peptide Nucleic Acid Controls Dynamic Conformations of RNA Bulges. *Journal of the American Chemical Society* **2023**, *145* (19), 10497-10504. DOI: 10.1021/jacs.2c12488 From NLM.

19. Rossi, J. J.; Cantin, E. M.; Zaia, J. A.; Ladne, P. A.; Chen, J.; Stephens, D. A.; Sarver, N.; Chang, P. S. Ribozymes as therapies for AIDS. *Ann N Y Acad Sci* **1990**, *616*, 184-200. DOI: 10.1111/j.1749-6632.1990.tb17839.x From NLM.

20. Zadeh, Joseph N; Steenberg, Conrad D; Bois, Justin S; Wolfe, Brian R; Pierce, Marshall B; Khan, Asif R; Dirks, Robert M; Pierce, Niles A. NUPACK: Analysis and design of nucleic acid systems. *Journal of computational chemistry* **2011**, *32* (1), 170-173.

21. Losito, I.; Angelico, R.; Introna, B.; Ceglie, A.; Palmisano, F. Cytosine to uracil conversion through hydrolytic deamination of cytidine monophosphate hydroxy-alkylated on the amino group: a liquid chromatography--electrospray ionization--mass spectrometry investigation. *J Mass Spectrom* **2012**, *47* (10), 1384-1393. DOI: 10.1002/jms.3078 From NLM.

22. Scheinker, V. S. Tritium labelling of nucleic acids accompanied by conversion of cytosine to uracil. *Nucleic Acids Res* **1976**, *3* (3), 809-816. DOI: 10.1093/nar/3.3.809 From NLM.

23. Schormann, N.; Ricciardi, R.; Chattopadhyay, D. Uracil-DNA glycosylases-structural and functional perspectives on an essential family of DNA repair enzymes. *Protein Sci* **2014**, *23* (12), 1667-1685. DOI: 10.1002/pro.2554 From NLM.

24. Li, Rongpeng; Mak, Chi H. Quantifying Nucleic Acid Base Pairing Free Energy. *Biophys J* **2018**, *114*.

25. Belov, D. A.; Belov, Yu. V.; Kiselev, Igor G. Modeling of the DNA Melting Point Dependence on Various Analysis Factors. *2020 International Multi-Conference on Industrial Engineering and Modern Technologies (FarEastCon)* **2020**, 1-3.

26. Wang, J.; Pan, X.; Liang, X. Assessment for Melting Temperature Measurement of Nucleic Acid by HRM. *J Anal Methods Chem* **2016**, *2016*, 5318935. DOI: 10.1155/2016/5318935 From NLM.

27. Barbatti, M.; Aquino, A. J.; Lischka, H. The UV absorption of nucleobases: semi-classical ab initio spectra simulations. *Phys Chem Chem Phys* **2010**, *12* (19), 4959-4967. DOI: 10.1039/b924956g From NLM.

28. Mitra, Debarghya; Bankoti, Namrata; Michael, Daliah; Sekar, Kanagaraj; Row, T. N. Guru. C-halogen…pi interactions in nucleic acids: a database study. *Journal of Chemical Sciences* **2020**, *132*, 1-6.

29. Rissone, P.; Ritort, F. Nucleic Acid Thermodynamics Derived from Mechanical Unzipping Experiments. *Life (Basel)* **2022**, *12* (7). DOI: 10.3390/life12071089 From NLM.

30. Brambati, Alessandra; Zardoni, Luca; Nardini, Eleonora; Pellicioli, Achille; Liberi, Giordano. The dark side of RNA:DNA hybrids. *Mutation Research/Reviews in Mutation Research* **2020**, *784*, 108300. DOI: https://doi.org/10.1016/j.mrrev.2020.108300.

31. Gait, Michael J.; Grasby, Jane A.; Karn, Jonathan; Mersmann, Karin; Pritchard, Clare E. Synthetic Ribonucleotide Analogues for RNA Structure-Function Studies. *Nucleosides, Nucleotides & Nucleic Acids* **1995**, *14*, 1133-1144.

32. Kamya, P. R.; Muchall, H. M. Revisiting the effects of sequence and structure on the hydrogen bonding and π-stacking interactions in nucleic acids. *J Phys Chem A* **2011**, *115* (45), 12800-12808. DOI: 10.1021/jp203918z From NLM.

33. Zgarbová, Marie; Jurečka, Petr; Banáš, Pavel; Otyepka, Michal; Šponer, Judit E.; Leontis, Neocles B.; Zirbel, Craig L.; Šponer, Jiří. Noncanonical Hydrogen Bonding in Nucleic Acids. Benchmark Evaluation of Key Base–Phosphate Interactions in Folded RNA Molecules Using Quantum-Chemical Calculations and Molecular Dynamics Simulations. *The Journal of Physical Chemistry A* **2011**, *115* (41), 11277-11292. DOI: 10.1021/jp204820b.

34. Leontis, N. B.; Westhof, E. Conserved geometrical base-pairing patterns in RNA. *Q Rev Biophys* **1998**, *31* (4), 399-455.

35. Lescoute, A.; Leontis, N. B.; Massire, C.; Westhof, E. Recurrent structural RNA motifs, Isostericity Matrices and sequence alignments. *Nucleic Acids Res* **2005**, *33* (8), 2395-2409. DOI: 10.1093/nar/gki535 From NLM.

36. Leontis, N. B.; Westhof, E. Geometric nomenclature and classification of RNA base pairs. *RNA* **2001**, *7* (4), 499-512.

37. Leontis, Neocles B; Stombaugh, Jesse; Westhof, Eric. The non-Watson–Crick base pairs and their associated isostericity matrices. *Nucleic acids research* **2002**, *30* (16), 3497-3531.

38. Stelling, A. L.; Liu, A. Y.; Zeng, W.; Salinas, R.; Schumacher, M. A.; Al-Hashimi, H. M. Infrared Spectroscopic Observation of a G-C(+) Hoogsteen Base Pair in the DNA:TATA-Box Binding Protein Complex Under Solution Conditions. *Angew Chem Int Ed Engl* **2019**, *58* (35), 12010-12013. DOI: 10.1002/anie.201902693 From NLM.

39. Bochman, Matthew L.; Paeschke, Katrin; Zakian, Virginia A. DNA secondary structures: stability and function of G-quadruplex structures. *Nature Reviews Genetics* **2012**, *13* (11), 770-780. DOI: 10.1038/nrg3296.

40. Bindewald, E.; Afonin, K.; Jaeger, L.; Shapiro, B. A. Multistrand RNA secondary structure prediction and nanostructure design including pseudoknots. *ACS Nano* **2011**, *5* (12), 9542-9551.

41. Hahn, H. P. von. Distribution of DNA and RNA in the Brain during the Life Span of the Albino Rat. *Gerontology* **1966**, *12*, 18-29.

42. Panigaj, Martin; Dobrovolskaia, Marina A.; Afonin, Kirill A. Viral Noncoding RNAs in Modulating Cellular Defense and Their Potential for RNA Nanotechnology. In *RNA Nanotechnology and Therapeutics*, CRC Press, 2022; pp 239-250.

43. Panigaj, Martin; Dobrovolskaia, Marina A; Afonin, Kirill A. 2021: an immunotherapy odyssey and the rise of nucleic acid nanotechnology. Future Medicine: 2021; Vol. 16, pp 1635-1640.

44. Johnson, Morgan Brittany; Halman, Justin R; Miller, Daniel K; Cooper, Joseph S; Khisamutdinov, F, Emil; Marriott, Ian; Afonin, Kirill A. The immunorecognition, subcellular compartmentalization, and physicochemical properties of nucleic acid nanoparticles can be controlled by composition modification. *Nucleic Acids Research* **2020**, *48* (20), 11785-11798. DOI: 10.1093/nar/gkaa908 (acccessed 2021-01-28T18:04:55).

45. Fedor, M. J. Comparative enzymology and structural biology of RNA self-cleavage. *Annu Rev Biophys* **2009**, *38*, 271-299. DOI: 10.1146/annurev.biophys.050708.133710 From NLM.

46. Saito, H.; Inoue, T. Synthetic biology with RNA motifs. *Int J Biochem Cell Biol* **2009**, *41* (2), 398-404. DOI: 10.1016/j.biocel.2008.08.017.

47. Belin, S.; Beghin, A.; Solano-Gonzàlez, E.; Bezin, L.; Brunet-Manquat, S.; Textoris, J.; Prats, A. C.; Mertani, H. C.; Dumontet, C.; Diaz, J. J. Dysregulation of ribosome biogenesis and translational capacity is associated with tumor progression of human breast cancer cells. *PLoS One* **2009**, *4* (9), e7147. DOI: 10.1371/journal.pone.0007147 From NLM.

48. Cadinoiu, Anca N.; Rata, Delia M.; Atanase, Leonard I.; Daraba, Oana M.; Gherghel, Daniela; Vochita, Gabriela; Popa, Marcel. Aptamer-Functionalized Liposomes as a Potential Treatment for Basal Cell Carcinoma. *Polymers* **2019**, *11* (9), 1515. DOI: 10.3390/polym11091515 (acccessed 2021-04-01T09:29:36).

49. Chandler, M.; Lyalina, T.; Halman, J.; Rackley, L.; Lee, L.; Dang, D.; Ke, W.; Sajja, S.; Woods, S.; Acharya, S.; et al. Broccoli Fluorets: Split Aptamers as a User-Friendly Fluorescent Toolkit for Dynamic RNA Nanotechnology. *Molecules* **2018**, *23* (12). DOI: 10.3390/molecules23123178.

50. Esposito, Carla L; Cerchia, Laura; Catuogno, Silvia; De Vita, Gennaro; Dassie, Justin P; Santamaria, Gianluca; Swiderski, Piotr; Condorelli, Gerolama; Giangrande, Paloma H; De Franciscis, Vittorio. Multifunctional aptamer-miRNA conjugates for targeted cancer therapy. *Molecular therapy* **2014**, *22* (6), 1151-1163.

51. Panigaj, M.; Johnson, M. B.; Ke, W.; McMillan, J.; Goncharova, E. A.; Chandler, M.; Afonin, K. A. Aptamers as Modular Components of Therapeutic Nucleic Acid Nanotechnology. *ACS Nano* **2019**, *13* (11), 12301-12321. DOI: 10.1021/acsnano.9b06522.

52. Keefe, Anthony D; Pai, Supriya; Ellington, Andrew. Aptamers as therapeutics. *Nature reviews Drug discovery* **2010**, *9* (7), 537-550.

53. Elbashir, S. M.; Harborth, J.; Lendeckel, W.; Yalcin, A.; Weber, K.; Tuschl, T. Duplexes of 21-nucleotide RNAs mediate RNA interference in cultured mammalian cells. *Nature* **2001**, *411* (6836), 494-498. DOI: 10.1038/35078107 From NLM.

54. Martins, A. N.; Ke, W.; Jawahar, V.; Striplin, M.; Striplin, C.; Freed, E. O.; Afonin, K. A. Intracellular Reassociation of RNA-DNA Hybrids that Activates RNAi in HIV-Infected Cells. *Methods Mol Biol* **2017**, *1632*, 269-283. DOI: 10.1007/978-1-4939-7138-1_18.

55. Afonin, K. A.; Grabow, W. W.; Walker, F. M.; Bindewald, E.; Dobrovolskaia, M. A.; Shapiro, B. A.; Jaeger, L. Design and self-assembly of siRNA-functionalized RNA nanoparticles for use in automated nanomedicine. *Nature protocols* **2011**, *6* (12), 2022-2034. DOI: 10.1038/nprot.2011.418.

56. Redfern, A. D.; Colley, S. M.; Beveridge, D. J.; Ikeda, N.; Epis, M. R.; Li, X.; Foulds, C. E.; Stuart, L. M.; Barker, A.; Russell, V. J.; et al. RNA-induced silencing complex (RISC) Proteins PACT, TRBP, and Dicer are SRA binding nuclear receptor coregulators. *Proceedings of the National Academy of Sciences of the United States of America* **2013**, *110* (16), 6536-6541. DOI: 10.1073/pnas.1301620110 From NLM.

57. Rackley, L.; Stewart, J. M.; Salotti, J.; Krokhotin, A.; Shah, A.; Halman, J. R.; Juneja, R.; Smollett, J.; Lee, L.; Roark, K.; et al. RNA Fibers as Optimized Nanoscaffolds for siRNA Coordination and Reduced Immunological Recognition. *Adv Funct Mater* **2018**, *28* (48). DOI: 10.1002/adfm.201805959.

58. Mitchell, William M. Efficacy of rintatolimod in the treatment of chronic fatigue syndrome/myalgic encephalomyelitis (CFS/ME). *Expert Review of Clinical Pharmacology* **2016**, *9* (6), 755-770. DOI: 10.1586/17512433.2016.1172960.

59. Afonin, Kirill A.; Dobrovolskaia, Marina A.; Church, George; Bathe, Mark. Opportunities, Barriers, and a Strategy for Overcoming Translational Challenges to

Therapeutic Nucleic Acid Nanotechnology. *ACS Nano* **2020**, *14* (8), 9221-9227. DOI: 10.1021/acsnano.0c04753 (acccessed 2021-01-04T20:59:11).

60. Afonin, Kirill A.; Dobrovolskaia, Marina A.; Ke, Weina; Grodzinski, Piotr; Bathe, Mark. Critical review of nucleic acid nanotechnology to identify gaps and inform a strategy for accelerated clinical translation. *Advanced Drug Delivery Reviews* **2022**, *181*, 114081. DOI: https://doi.org/10.1016/j.addr.2021.114081.

61. Avila, Yelixza I.; Chandler, Morgan; Cedrone, Edward; Newton, Hannah S.; Richardson, Melina; Xu, Jie; Clogston, Jeffrey D.; Liptrott, Neill J.; Afonin, Kirill A.; Dobrovolskaia, Marina A. Induction of Cytokines by Nucleic Acid Nanoparticles (NANPs) Depends on the Type of Delivery Carrier. *Molecules* **2021**, *26* (3), 652. DOI: 10.3390/molecules26030652 (acccessed 2021-01-28T18:30:11).

62. Bila, Dominika; Radwan, Yasmine; Dobrovolskaia, Marina A.; Panigaj, Martin; Afonin, Kirill A. The Recognition of and Reactions to Nucleic Acid Nanoparticles by Human Immune Cells. *Molecules* **2021**, *26* (14), 4231.

63. Hong, E.; Halman, J. R.; Shah, A.; Cedrone, E.; Truong, N.; Afonin, K. A.; Dobrovolskaia, M. A. Toll-Like Receptor-Mediated Recognition of Nucleic Acid Nanoparticles (NANPs) in Human Primary Blood Cells. *Molecules* **2019**, *24* (6). DOI: 10.3390/molecules24061094.

64. Kawasaki, T.; Kawai, T. Toll-like receptor signaling pathways. *Front Immunol* **2014**, *5*, 461. DOI: 10.3389/fimmu.2014.00461 From NLM PubMed-not-MEDLINE.

65. Hong, E.; Halman, J. R.; Shah, A. B.; Khisamutdinov, E. F.; Dobrovolskaia, M. A.; Afonin, K. A. Structure and Composition Define Immunorecognition of Nucleic Acid Nanoparticles. *Nano letters* **2018**, *18* (7), 4309-4321. DOI: 10.1021/acs.nanolett.8b01283.

66. Chandler, M.; Johnson, M. B.; Panigaj, M.; Afonin, K. A. Innate immune responses triggered by nucleic acids inspire the design of immunomodulatory nucleic acid nanoparticles (NANPs). *Curr Opin Biotechnol* **2019**, *63*, 8-15. DOI: 10.1016/j.copbio.2019.10.011.

67. Johnson, M. B.; Halman, J. R.; Satterwhite, E.; Zakharov, A. V.; Bui, M. N.; Benkato, K.; Goldsworthy, V.; Kim, T.; Hong, E.; Dobrovolskaia, M. A.; et al. Programmable Nucleic Acid Based Polygons with Controlled Neuroimmunomodulatory Properties for Predictive QSAR Modeling. *Small (Weinheim an der Bergstrasse, Germany)* **2017**, *13* (42). DOI: 10.1002/smll.201701255 From NLM.

68. Gosu, V.; Basith, S.; Kwon, O. P.; Choi, S. Therapeutic applications of nucleic acids and their analogues in Toll-like receptor signaling. *Molecules* **2012**, *17* (11), 13503-13529. DOI: 10.3390/molecules171113503 From NLM.

69. Zheng, C.; Chen, J.; Chu, F.; Zhu, J.; Jin, T. Inflammatory Role of TLR-MyD88 Signaling in Multiple Sclerosis. *Front Mol Neurosci* **2019**, *12*, 314. DOI: 10.3389/fnmol.2019.00314 From NLM PubMed-not-MEDLINE.

70. Majer, Olivia; Liu, Bo; Barton, Gregory M. Nucleic acid-sensing TLRs: trafficking and regulation. *Current Opinion in Immunology* **2017**, *44*, 26-33. DOI: 10.1016/j.coi.2016.10.003 (acccessed 2021-02-02T11:35:32).

71. Le Naour, J.; Galluzzi, L.; Zitvogel, L.; Kroemer, G.; Vacchelli, E. Trial watch: TLR3 agonists in cancer therapy. *Oncoimmunology* **2020**, *9* (1), 1771143. DOI: 10.1080/2162402x.2020.1771143 From NLM.

72. Diebold, Sandra S.; Montoya, Maria; Unger, Hermann; Alexopoulou, Lena; Roy, Polly; Haswell, Linsey E.; Al-Shamkhani, Aymen; Flavell, Richard; Borrow, Persephone; Sousa, Caetano Reis e. Viral infection switches non-plasmacytoid dendritic cells into high interferon producers. *Nature* **2003**, *424* (6946), 324-328. DOI: 10.1038/nature01783.

73. Dauber, Bianca; Schneider, Jana; Wolff, Thorsten. Double-Stranded RNA Binding of Influenza B Virus Nonstructural NS1 Protein Inhibits Protein Kinase R but Is Not Essential To Antagonize Production of Alpha/Beta Interferon. *Journal of Virology* **2006**, *80* (23), 11667-11677. DOI: 10.1128/jvi.01142-06 (acccessed 2023/06/03).

74. Lemaire, Peter A.; Anderson, Eric; Lary, Jeffrey; Cole, James L. Mechanism of PKR Activation by dsRNA. *J Mol Biol* **2008**, *381* (2), 351-360. DOI: 10.1016/j.jmb.2008.05.056.

75. Diebold, Sandra S; Kaisho, Tsuneyasu; Hemmi, Hiroaki; Akira, Shizuo; Reis e Sousa, Caetano. Innate antiviral responses by means of TLR7-mediated recognition of single-stranded RNA. *Science* **2004**, *303* (5663), 1529-1531.

76. Zhang, Zhikuan; Ohto, Umeharu; Shibata, Takuma; Taoka, Masato; Yamauchi, Yoshio; Sato, Ryota; Shukla, Nikunj M.; David, Sunil A.; Isobe, Toshiaki; Miyake, Kensuke; et al. Structural Analyses of Toll-like Receptor 7 Reveal Detailed RNA Sequence Specificity and Recognition Mechanism of Agonistic Ligands. *Cell Reports* **2018**, *25* (12), 3371-3381.e3375. DOI: 10.1016/j.celrep.2018.11.081 (acccessed 2021-02-02T11:55:11).

77. Fejtkova, M.; Sukova, M.; Hlozkova, K.; Skvarova Kramarzova, K.; Rackova, M.; Jakubec, D.; Bakardjieva, M.; Bloomfield, M.; Klocperk, A.; Parackova, Z.; et al. TLR8/TLR7 dysregulation due to a novel TLR8 mutation causes severe autoimmune hemolytic anemia and autoinflammation in identical twins. *Am J Hematol* **2022**, *97* (3), 338-351. DOI: 10.1002/ajh.26452 From NLM.

78. De Marcken, Marine; Dhaliwal, Khushwant; Danielsen, Ann Caroline; Gautron, Anne Sophie; Dominguez-Villar, Margarita. TLR7 and TLR8 activate distinct pathways in monocytes during RNA virus infection. *Science Signaling* **2019**, *12* (605), eaaw1347. DOI: 10.1126/scisignal.aaw1347 (acccessed 2021-02-02T11:57:17).

79. Gorden, Keith B.; Gorski, Kevin S.; Gibson, Sheila J.; Kedl, Ross M.; Kieper, William C.; Qiu, Xiaohong; Tomai, Mark A.; Alkan, Sefik S.; Vasilakos, John P. Synthetic TLR Agonists Reveal Functional Differences between Human TLR7 and TLR8. *The Journal of Immunology* **2005**, *174* (3), 1259-1268. DOI: 10.4049/jimmunol.174.3.1259.

80. Latz, E.; Visintin, A.; Espevik, T.; Golenbock, D. T. Mechanisms of TLR9 activation. *J Endotoxin Res* **2004**, *10* (6), 406-412. DOI: 10.1179/096805104225006525 From NLM.

81. Krieg, A. M. CpG motifs in bacterial DNA and their immune effects. *Annu Rev Immunol* **2002**, *20*, 709-760. DOI: 10.1146/annurev.immunol.20.100301.064842 From NLM.

82. Loo, Yueh-Ming; Gale, Michael. Immune Signaling by RIG-I-like Receptors. *Immunity* **2011**, *34* (5), 680-692. DOI: 10.1016/j.immuni.2011.05.003 (acccessed 2021-02-02T12:11:51).

83. Yu, Le; Liu, Pengda. Cytosolic DNA sensing by cGAS: regulation, function, and human diseases. *Signal Transduction and Targeted Therapy* **2021**, *6* (1), 170. DOI: 10.1038/s41392-021-00554-y.

84. Halman, J. R.; Afonin, K. A. Editorial for the Special Issue on "Nucleic Acid Architectures for Therapeutics, Diagnostics, Devices and Materials". *Nanomaterials (Basel)* **2019**, *9* (7). DOI: 10.3390/nano9070951.

85. Halman, Justin; Satterwhite, Emily; Smollett, Jaclyn; Bindewald, Eckart; Parlea, Lorena; Viard, Mathias; Zakrevsky, Paul; Kasprzak, Wojciech K.; Afonin, Kirill A.; Shapiro, Bruce A. Triggerable RNA nanodevices. *RNA & disease (Houston, Tex.)* **2017**, *4*.

86. Afonin, K. A.; Viard, M.; Koyfman, A. Y.; Martins, A. N.; Kasprzak, W. K.; Panigaj, M.; Desai, R.; Santhanam, A.; Grabow, W. W.; Jaeger, L.; et al. Multifunctional RNA nanoparticles. *Nano letters* **2014**, *14* (10), 5662-5671. DOI: 10.1021/nl502385k.

87. Westhof, E.; Masquida, B.; Jaeger, L. RNA tectonics: towards RNA design. *Fold Des* **1996**, *1* (4), R78-88. DOI: 10.1016/S1359-0278(96)00037-5.

88. Kim, T.; Afonin, K. A.; Viard, M.; Koyfman, A. Y.; Sparks, S.; Heldman, E.; Grinberg, S.; Linder, C.; Blumenthal, R. P.; Shapiro, B. A. In Silico, In Vitro, and In Vivo Studies Indicate the Potential Use of Bolaamphiphiles for Therapeutic siRNAs Delivery. *Molecular therapy* **2013**, *2*, e80.

89. Afonin, Kirill A.; Kasprzak, Wojciech K.; Bindewald, Eckart; Kireeva, Maria; Viard, Mathias; Kashlev, Mikhail; Shapiro, Bruce A. In silico design and enzymatic synthesis of functional RNA nanoparticles. *Accounts of chemical research* **2014**, *47* (6), 1731-1741. DOI: 10.1021/ar400329z From PubMed.

90. Afonin, K. A.; Bindewald, E.; Yaghoubian, A. J.; Voss, N.; Jacovetty, E.; Shapiro, B. A.; Jaeger, L. In vitro assembly of cubic RNA-based scaffolds designed in silico. *Nat Nanotechnol* **2010**, *5* (9), 676-682. DOI: 10.1038/nnano.2010.160.

91. Grabow, W. W.; Zakrevsky, P.; Afonin, K. A.; Chworos, A.; Shapiro, B. A.; Jaeger, L. Self-assembling RNA nanorings based on RNAI/II inverse kissing complexes. *Nano letters* **2011**, *11* (2), 878-887.

92. Ke, W.; Hong, E.; Saito, R. F.; Rangel, M. C.; Wang, J.; Viard, M.; Richardson, M.; Khisamutdinov, E. F.; Panigaj, M.; Dokholyan, N. V.; et al. RNA-DNA fibers and polygons with controlled immunorecognition activate RNAi, FRET and transcriptional regulation of NF-κB in human cells. *Nucleic Acids Res* **2019**, *47* (3), 1350-1361. DOI: 10.1093/nar/gky1215 From NLM.

93. Ke, W.; Hong, E.; Saito, R. F.; Rangel, M. C.; Wang, J.; Viard, M.; Richardson, M.; Khisamutdinov, E. F.; Panigaj, M.; Dokholyan, N. V.; et al. RNA-DNA fibers and polygons with controlled immunorecognition activate RNAi, FRET and transcriptional regulation of NF-kappaB in human cells. *Nucleic Acids Res* **2019**, *47* (3), 1350-1361. DOI: 10.1093/nar/gky1215.

94. Parlea, L.; Bindewald, E.; Sharan, R.; Bartlett, N.; Moriarty, D.; Oliver, J.; Afonin, K. A.; Shapiro, B. A. Ring Catalog: A resource for designing self-assembling RNA nanostructures. *Methods* **2016**, *103*, 128-137. DOI: 10.1016/j.ymeth.2016.04.016.

95. Bindewald, E.; Hayes, R.; Yingling, Y. G.; Kasprzak, W.; Shapiro, B. A. RNAJunction: a database of RNA junctions and kissing loops for three-dimensional structural analysis and nanodesign. *Nucleic Acids Res* **2008**, *36* (Database issue), D392-397.

96. Panigaj, M.; Dobrovolskaia, M. A.; Afonin, K. A. 2021: an immunotherapy odyssey and the rise of nucleic acid nanotechnology. *Nanomedicine (Lond)* **2021**, *16* (19), 1635-1640. DOI: 10.2217/nnm-2021-0097.

97. Kularatne, R. N.; Crist, R. M.; Stern, S. T. The Future of Tissue-Targeted Lipid Nanoparticle-Mediated Nucleic Acid Delivery. *Pharmaceuticals (Basel)* **2022**, *15* (7). DOI: 10.3390/ph15070897 From NLM.

98. Dobrovolskaia, Marina A.; Afonin, Kirill A. Use of human peripheral blood mononuclear cells to define immunological properties of nucleic acid nanoparticles. *Nature protocols* **2020**, *15* (11), 3678-3698. DOI: 10.1038/s41596-020-0393-6 (acccessed 2021-01-28T18:07:44).

99. Halman, J. R.; Satterwhite, E.; Roark, B.; Chandler, M.; Viard, M.; Ivanina, A.; Bindewald, E.; Kasprzak, W. K.; Panigaj, M.; Bui, M. N.; et al. Functionally-interdependent shape-switching nanoparticles with controllable properties. *Nucleic Acids Res* **2017**, *45* (4), 2210-2220. DOI: 10.1093/nar/gkx008 From NLM.

100. Nordmeier, Senny; Ke, Weina; Afonin, Kirill A.; Portnoy, Victoria. Exosome mediated delivery of functional nucleic acid nanoparticles (NANPs). *Nanomedicine: Nanotechnology, Biology and Medicine* **2020**, *30*, 102285. DOI: https://doi.org/10.1016/j.nano.2020.102285.

101. Roark, B. K.; Tan, L. A.; Ivanina, A.; Chandler, M.; Castaneda, J.; Kim, H. S.; Jawahar, S.; Viard, M.; Talic, S.; Wustholz, K.L.; et al. Fluorescence blinking as an output signal for biosensing. *ACS sensors* **2016**, *1* (11), 1295-1300.

102. Ke, Weina; Chandler, Morgan; Cedrone, Edward; Saito, Renata F.; Rangel, Maria Cristina; de Souza Junqueira, Mara; Wang, Jian; Shi, Da; Truong, Nguyen; Richardson, Melina; et al. Locking and Unlocking Thrombin Function Using Immunoquiescent Nucleic Acid Nanoparticles with Regulated Retention In Vivo. *Nano letters* **2022**, *22* (14), 5961-5972. DOI: 10.1021/acs.nanolett.2c02019.

103. Tran, Allison N.; Chandler, Morgan; Halman, Justin; Beasock, Damian; Fessler, Adam; McKeough, Riley Q.; Lam, Phuong Anh; Furr, Daniel P.; Wang, Jian; Cedrone, Edward; et al. Anhydrous Nucleic Acid Nanoparticles for Storage and Handling at Broad Range of Temperatures. *Small (Weinheim an der Bergstrasse, Germany)* **2022**, *n/a* (n/a), 2104814, https://doi.org/10.1002/smll.202104814. DOI: https://doi.org/10.1002/smll.202104814 (acccessed 2022/03/11).

104. Ng, Eugene W. M.; Shima, David T.; Calias, Perry; Cunningham Jr, Emmett T.; Guyer, David R.; Adamis, Anthony P. Pegaptanib, a targeted anti-VEGF aptamer for ocular vascular disease. *Nature reviews drug discovery* **2006**, *5* (2), 123-132.

105. Sahebkar, Amirhossein; Watts, Gerald F. Managing recalcitrant hypercholesterolemia in patients on current best standard of care: efficacy and safety of novel pharmacotherapies. *Clinical Lipidology* **2014**, *9* (2), 221-233.

106. Scott, Lesley J. Givosiran: first approval. *Drugs* **2020**, *80* (3), 335-339.

107. Migliorati, Julia M.; Jin, Jing; Zhong, Xiao-bo. siRNA drug Leqvio (inclisiran) to lower cholesterol. *Trends in pharmacological sciences* **2022**, *43* (5), 455-456.

108. Verbeke, Rein; Lentacker, Ine; De Smedt, Stefaan C.; Dewitte, Heleen. The dawn of mRNA vaccines: The COVID-19 case. *Journal of Controlled Release* **2021**, *333*, 511-520. DOI: https://doi.org/10.1016/j.jconrel.2021.03.043.

109. Keam, Susan J. Vutrisiran: First Approval. *Drugs* **2022**, *82* (13), 1419-1425.

110. Newton, Hannah S.; Radwan, Yasmine; Xu, Jie; Clogston, Jeffrey D.; Dobrovolskaia, Marina A.; Afonin, Kirill A. Change in Lipofectamine Carrier as a Tool to Fine-Tune Immunostimulation of Nucleic Acid Nanoparticles. In *Molecules*, 2023; Vol. 28.

111. Halman, J. R.; Kim, K. T.; Gwak, S. J.; Pace, R.; Johnson, M. B.; Chandler, M. R.; Rackley, L.; Viard, M.; Marriott, I.; Lee, J. S.; et al. A cationic amphiphilic co-polymer as a carrier of nucleic acid nanoparticles (Nanps) for controlled gene silencing, immunostimulation, and biodistribution. *Nanomedicine* **2020**, *23*, 102094. DOI: 10.1016/j.nano.2019.102094.

112. Kim, T.; Viard, M.; Afonin, K. A.; Gupta, K.; Popov, M.; Salotti, J.; Johnson, P. F.; Linder, C.; Heldman, E.; Shapiro, B. A. Characterization of Cationic Bolaamphiphile Vesicles for siRNA Delivery into Tumors and Brain. *Molecular therapy* **2020**, *20*, 359-372. DOI: 10.1016/j.omtn.2020.02.011.

113. Halman, Justin; Satterwhite, Emily; Smollett, Jaclyn; Bindewald, Eckart; Parlea, Lorena; Viard, Mathias; Zakrevsky, Paul; Kasprzak, Wojciech K.; Afonin, Kirill A.; Shapiro, Bruce A. Triggerable RNA Nanodevices. *Rna & Disease* **2016**. DOI: 10.14800/rd.1349.

114. Grabow, Wade W.; Afonin, Kirill A.; Zakrevsky, Paul; Walker, Faye M.; Calkins, Erin R.; Geary, Cody; Kasprzak, Wojciech; Bindewald, Eckart; Shapiro, Bruce A.; Jaeger, Luc. RNA Nanotechnology in Nanomedicine. In *Nanomedicine and Drug Delivery*, 2013.

2 CHAPTER 2: BIOMOTORS, VIRAL ASSEMBLY, AND RNA NANOBIOTECHNOLOGY: CURRENT ACHIEVEMENTS AND FUTURE DIRECTIONS

2.1 Introduction

Nucleic acid engineering has been gaining considerable momentum for over a decade since the first meeting of the International Society of RNA Nanotechnology and Nanomedicine (ISRNN). This massive research effort is inspired by the immense potential that RNA offers to basic research and in clinical settings. RNA is a natural biopolymer that is highly integrated in a plethora of mechanisms essential for life and thus, understanding RNA's folding, structure, and functions would allow for the rational design of RNA-based therapies and nanodevices suitable for biomedicines [1, 2]. As the translational aspects of the field have advanced, there have been new RNA therapies approved for clinical use [3], most notably two SARS-CoV-2 mRNA vaccines that were rapidly developed and introduced during the COVID-19 pandemic. Despite these successes, the numerous translational challenges of RNA therapeutics [4-8] still preclude their broader biomedical applications. With the increasing number of research teams whose work focuses on overcoming these barriers, the emerging RNA field keeps moving towards curative goals.

In order to advance the applications of RNA in the fields of nanotechnology and nanomedicine, an interdisciplinary effort must be undertaken. To further this goal, the ISRNN has hosted a biennial meeting series, entitled "Biomotors, Viral Assembly, and RNA Nanobiotechnology". At these events, researchers gather from across the globe to share and discuss their findings in each of these areas, with the most recent boasting presentations from over 15 countries by 68 independent researchers. This critical review aims to cover recent

research highlights and perspectives in selected topics; namely, we discuss advancements in the fields of biomotors and biomachines, nanopores, nanozymes, viral frameshifting elements, RNA structure prediction and assessment, and RNA nanotechnology.

2.2 Biomotors and Biomachines

2.2.1 The push-to-open mechanism and the challenge of tethered mechano-sensitive ion channel NompC

The 2021 Nobel Prize in Physiology and Medicine was given to Professors David Julis and Aderm Patapoutian for their discoveries of receptors that sense heat and pain. These breakthroughs launched intense research activities that lead to a rapid increase in our understanding of how our nervous system senses changes in temperature and mechanical stimuli. NompC is a TRP (Transient Receptor Potential) channel that is in the same family as the capsaicin receptor TRPV1. NompC is also a special mechanosensitive ion channel responsible for the sensation of touch and balance in Drosophila melanogaster [9]. Based on a cryo-EM structure of NompC [10], the team performed all-atom molecular dynamics simulations and electrophysiological experiments to study the atomistic details of NompC gating. As shown in Figure 1, work done in the Shu group showed that NompC could be opened by compression of the intracellular ankyrin repeat domain but not by stretching, and that a number of hydrogen bonds along the force conveyance pathway are important for the mechanosensitivity [11]. Under intracellular compression, the bundled ankyrin repeat region acts like a spring with a spring constant of ~13 pN/nm and transfers forces at a rate of ~1.8 nm/ps. The linker helix region acts as a bridge between the ankyrin repeats and the transient receptor potential (TRP) domain, which passes on the pushing force to the TRP domain to undergo a clockwise rotation, resulting in the opening of the channel. This could be the

universal gating mechanism of similar tethered mechanosensitive TRP channels, which enable cells to feel compression and shrinkage.

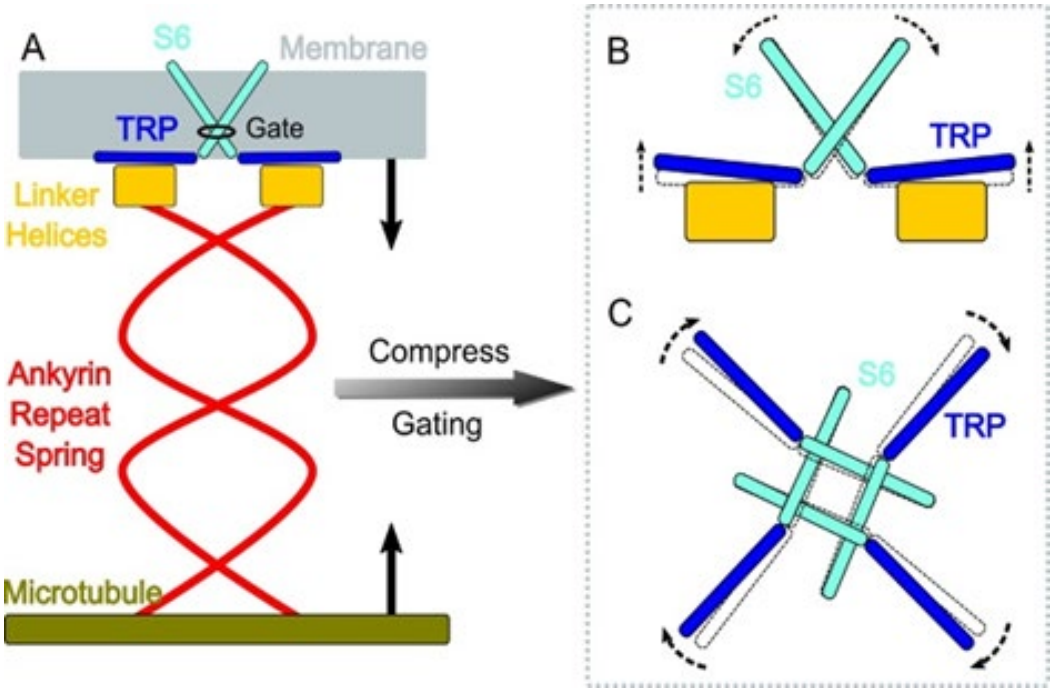

Figure 1. (A) The compression of the ankyrin repeat (AR) region will generate a pushing force and a torque on the linker helix (LH) domain, pointing to the extracellular side. (B) The LH domain further pushes the transient receptor potential (TRP) domain, leading to a tilt (side view), and (C) a clockwise rotation of the TRP domain (looking from the intracellular side). The motion of the TRP domain pulls the S6 helices to slightly tilt and rotate, which dilates the constriction site of the pore.

The Shu group's experimental collaborators, Prof. Zhiqiang Yan's group, found, using the cell-attached patch clamp method that positive pressure acted on the NompC expressed by Drosophila melanogaster S2 neuro cells, which simulated the compression of the gating spring on NompC [11]. From this experiment, electrical signals were detected from the cells, which indicated that the NompC channel was open in response to the compression of gating spring. By using the cell-attached method with negative pressure, there was no obvious current detected. On the other hand, the outside-out patch clamp method with negative pressure which also simulate the compression of gating spring, they can detect obvious

current. These experiments validated the Shu group's findings from MD simulations using in vitro methods. These findings were further validated by Prof. Michael Krieg's research group via an in vivo C. elegans behavior experiment [12]. They found that the movement of C. elegans was controlled by two ion channels. Straight-forward movement was controlled by the TREK2 channel, a mechanosensitive potassium channel that can sense membrane stretching and transmit electric signals. The omega turn movement of C. elegans was found to be controlled by the NompC channel, which is stimulated by cellular compression [11]. NompC-knock out C. elegans can only go straight while the TREK2-knocked out C elegans can only perform the omega turn movement. Therefore, they summarize an interesting physical model of C. elegans. When the C. elegans moves straight, the TREK2 channel opens due to the stretch of nerve cells while NompC remain closed. On the contrary, when s C. elegans performs an omega turn, the sensory cells are compressed, opening the NompC channel while TREK2 is closed. These findings showed that NompC plays key roles in sensing touch and proprioception in C. elegans, which will provide promising logic element for designing smart C. elegans.

The push-to-open gating mechanism of NompC represents a special mechanism for sensing the compression of sensory cells, which is different from other traditional mechano-sensitive ion channels that mainly rely on membrane surface extension and respond to cell expansion. This model provides a promising area for designing smart biosensors in response to mechanical stimuli. Although the sequence and structure of other TRP ion channel family members, such as TRPV1 and TRPV4, is similar to NompC, whether the gating mechanism of these TRP channels obeys the push to open model remains an open challenge for structural biology. In the near future, the humans will begin to expand their explorations of space. The

low gravity conditions in space pose a large challenge to the health of astronauts. Astronauts will face quite different health challenges from those living on earth. The relative studies on the gating of TRP channels under extreme conditions such as low gravity will give new insight to solve these problems.

2.2.2 The asymmetrical revolving motor mechanism

A key characteristic of "living beings" is movement. These motion activities are usually performed by ATPase motors [13, 14]. One of the most important motor functions is dsDNA translocation, which occurs during DNA replication, cellular mitosis, plasmid conjugation, DNA repair, and dsDNA viral genome packaging. The motor of these essential living processes shares plenty of similarities, such as the structure and mechanism. A rotatory mechanism has become a common belief due to the helical structure of the substrate DNA; however, the rotation mechanism is questioned based on several experimental data [15, 16]. To solve this problem, a revolving mechanism is proposed [17]. Rotation involves the turning of an object around its own axis like Earth moving around its axis every 24 hours, while revolving is the circular motion of an object around a secondary object, similar to Earth orbiting the sun every 365 days. Studies of the structure of biological motors in different species have suggested a similar revolving mechanism that can transport the long dsDNA genome. This mechanism is established in the dsDNA packaging motor of the bacterial virus phi29, which uses six ATPases to work in sequential action (Figure 2) [18, 19]. Several other biomotors have been reported to function in the revolving mechanism as well, such as the packaging motor of herpesviruses [20], the cell division motor of Escherichia coli FtsK [21], and plasmid conjugation motor TraB in streptomyces [22]. The studies of these motors suggest an asymmetric hexameric structure for transporting dsDNA in the sequential mechanism of action that is the motor

contains four monomer subunits and one dimeric subunit arranged in an asymmetrical structure. The finding may help understand why huge genomes, including chromosomes, translocate in complex systems without coiling and tangling, which will decrease the speed of dsDNA translocation and consume more energy.

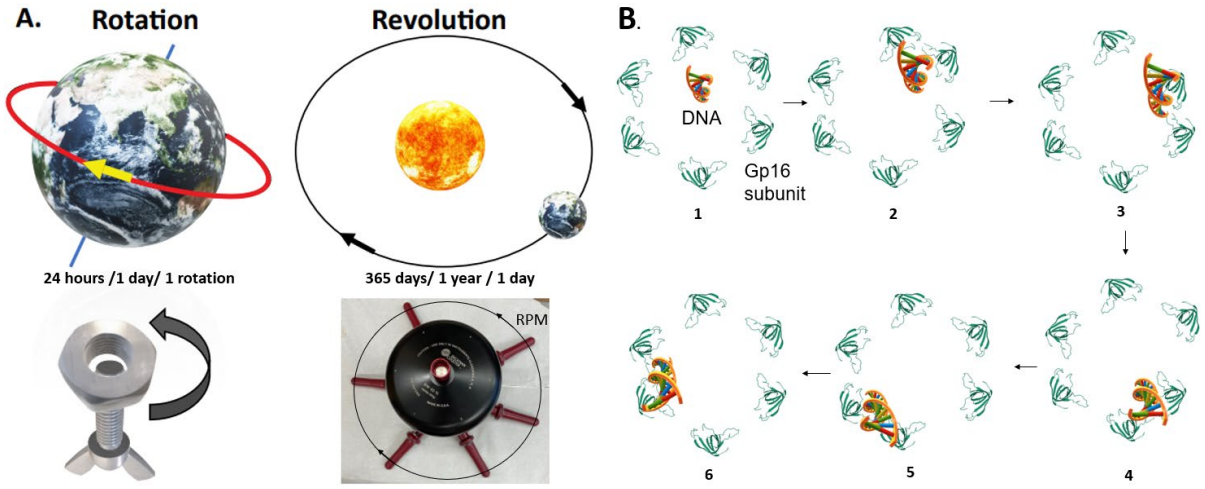

Figure 2. Differentiation of revolving mechanism from the rotation mechanism. Rotation is the object turning along its own axis. Revolving is one object moving around a second object. (A) Earth rotates one round every 24 hours, analogous to the rotation of the bolt and nut (B). (C) Earth moving around the sun every 365 days per circles. Revolution is analogous to the RPM (revolution per minute) counting of rotors in ultracentrifugation (D). (E) The DNA translocation motor used a revolving mechanism. The revolving is a result of the sequential action of individual subunits trafficking DNA. DNA hugs the channel wall via sequential handoffs via dimerization of individual gp16 subunits (PDB 2KCA)[23]. This sequential dimerization of the gp16 subunits is ATP driven and traffics one strand of the DNA through the connector through touch and go interactions.

2.3 Nanopore and Nanozyme Technologies

2.3.1 Protein fingerprinting through nanopores

Nanopore technology has demonstrated its ability to detect fine molecular details, allowing the study of subtle changes in protein or RNA conformation [24, 25], characterization of short polypeptide chains with single amino acid resolution, detect and identify specific amino acids [26, 27] and detect subtle chemical modifications [28, 29] or post-translational modifications [30, 31] all

which led to the hope of directly sequencing whole proteins. In addition, the biological nanopore can be reengineered to be inserted in lipid bilayer system or commercially available platform [32, 33].

While recent efforts to sequence proteins at the single-molecule level using nanopores have shown promise [28, 34, 35] reading the protein sequence remains a challenge. Considering the complexity of identifying proteins by reading their sequence, a new approach to identify proteins without reading their sequence has recently been demonstrated [36, 37]. This approach consists on identifying proteins by monitoring fragments resulting from the reaction products of a protease through biological nanopores and using protein databases to determine to which protein those fragments correspond, in a manner roughly similar to mass spectrometry (Figure 3). Specifically, it has been demonstrated that the AeL nanopore enables discrimination between three different proteins with approximately the same molecular mass, opening up the possibility of extending this approach to the identification of proteins irrespective of their size, charge, and structure/conformation [36]. This new approach, which can easily be miniaturized, could replace mass spectrometry as a part of the protein identification workflow. If implemented by a commercial entity, the technology could be made practical and low cost enough for use at point-of-care facilities, as the identification of proteins for health-care applications does not require full sequencing.

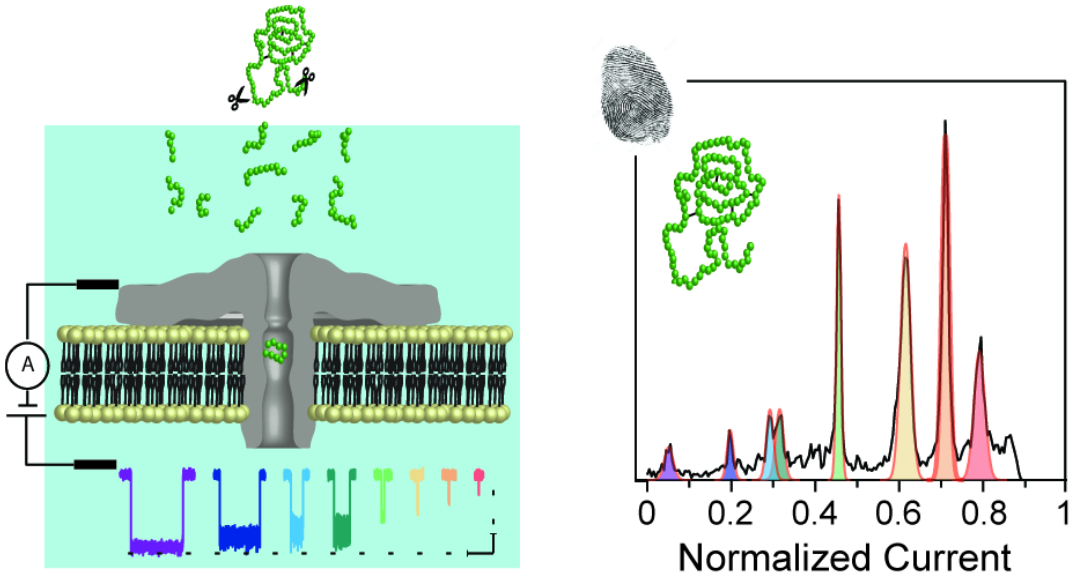

Figure 3. Following protease digestion, peptide fragments of various lengths and sequence can be distinguished as they travel through a nanopore as a function of the normalized current across the membrane, resulting in a unique fingerprint for each protein.

2.3.2 Computational design of nanozymes for biomedical applications

Many inorganic nanomaterials have intrinsic catalytic activities in living cells mimicking those of oxidoreductases, which endow the nanomaterials with intriguing potentials in biomedical applications [38]. These nanomaterials are collectively called nanozymes. For example, the peroxidase-activity of nanomaterials activates H_2O_2, which is abundant in tumor cells, to abstract electrons from the surroundings and thus induces apoptosis or necrosis of tumor cells. The catalase-like activity converts H_2O_2 into O_2, which is useful to attenuate tumor hypoxia. The superoxide dismutase-like activity is useful for scavenging O_2^{*-}, providing the nanomaterials with anti-oxidant activity. Owing to their enzyme-like activities, the nanomaterials have potentials in tumor chemodynamic, anti-hypoxia, and antioxidant protection therapies (Figure 4).

Because specific biomedical applications require that the nanomaterials have high catalytic activities, it is desirable to understand the atomistic-level mechanisms for the catalysis and

develop theoretical methods to evaluate the activities prior to experimental applications. Density functional theory calculations have played an indispensable role in studying atomistic mechanisms and structure-activity relationships for catalysts. Using these calculations, the Gao group has studied the mechanisms for the above oxidoreductase-like activities and further developed theoretical methods to predict the peroxidase-, catalase-, and superoxide dismutase-like activities of nanomaterials, paving a road for the application-targeted design of nanozymes [39-41].

However, challenges still remain. Among them, a big challenge is to improve the substrate selectivity for the nanomaterial catalysis by de novo design, and another question is to improve the accuracy of experimental fabrication and characterization of nanomaterials to comply with the design. Other questions like the long-term toxicity of nanomaterials merit further investigation.

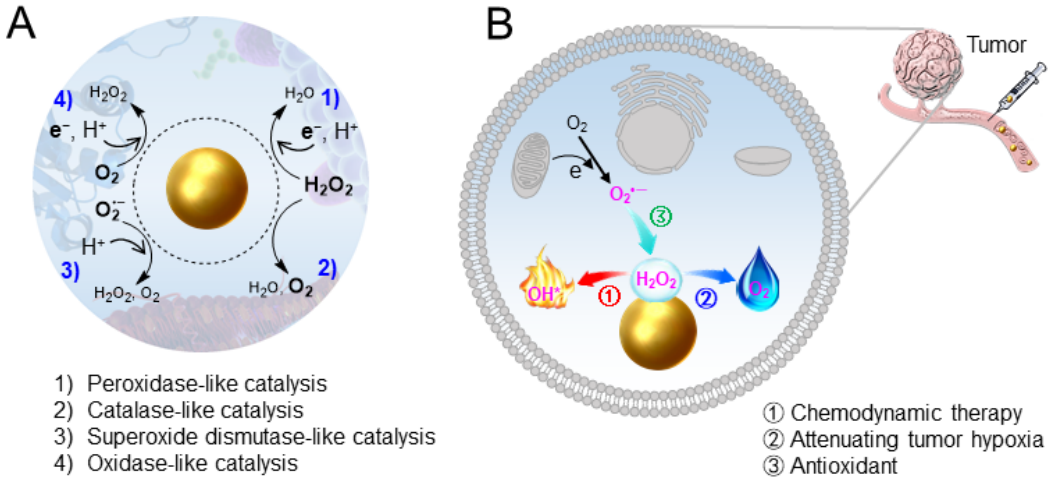

Figure 4. (A) The enzyme-like activities of nanomaterials and (B) potential biomedical applications.

2.4 Ribosomal Frameshifting Elements

2.4.1 Programmed ribosomal frameshifting: a potential broad range target for antiviral therapeutics

Human population growth, climate change, and globalization are accelerating the emergence of novel pathogenic viruses. Many viruses use a programmed −1 ribosomal frameshift (−1 PRF) mechanism to direct synthesis of their replicase proteins, a critical switch in their replication program that can be therapeutically targeted [42]. Nearly half a century of research into −1 PRF have provided insight into its biological importance, the molecular mechanisms that drive it, and approaches that can be used to manipulate it towards therapeutic outcomes, with particular emphasis on SARS-CoV-2.

The -1 PRF is a kinetically driven process. Elongating ribosomes are forced to pause over heptameric “slippery sequences” by metastable frameshift stimulating elements (FSEs) on mRNAs, typically pseudoknots [43]. Emerging evidence suggests that the frequency of -1 PRF events is dictated by the extent of structural heterogeneity, or Shannon Entropy, of these FSEs [44]. The idea is that the greater the number of structures that a sequence can sample, the greater the chance that one will be sampled that favors ribosome slippage. The ribosome is also an active player in the frameshift process. The dynamic conformational changes that it undergoes as it transits through the elongation cycle, along with the hydrolysis of GTP by the elongation factors provides the energetic inputs required to overcome the otherwise energetically unfavorable slippage events [43]. While -1 PRF is ultimately a stochastic process, each individual -1 PRF signal is evolutionarily fine-tuned to shift ribosomes at a specific frequency.

First demonstrated using the yeast "Killer" virus system [45], the idea that altering -1 PRF rates negatively impacts viral replication has been broadly demonstrated in retroviruses, coronaviruses, flaviviruses, alphaviruses, and others [42]. Decreases in -1 PRF can result in large, e. g., 3-4 orders of magnitude, decreases in viral copy numbers [46-48]. The triple-stem loop FSEs of coronaviruses present particularly promising therapeutic targets, as they harbor ring and hole structures conveniently sized to accommodate drug-sized small molecules [49-51]. Recently, high throughput screens have identified FDA approved drugs that alter SARS-CoV-2 -1 PRF efficiency, as well as -1 PRF promoted by other coronaviruses that may potentially emerge into the human population [52-54]. However, these small molecules were originally optimized to interact with proteins; efforts should be devoted toward developing RNA-specific interactors.

Although numerous academic and private entities are currently targeting the -1 PRF signal of SARS-CoV-2, the challenge of drugging a highly dynamic RNA structural element situates these efforts at the cutting edge of technology. Further, while -1 PRF is an essential regulatory element for many viruses, each viral -1 PRF signal is unique, likely necessitating developing -1 PRF signal-specific drugs for every virus. Additionally, as it is becoming clear that -1 PRF is used to regulate human gene expression [55, 56], the activities of such antiviral agents on -1 PRF in cellular genes will have to be investigated, although, as noted above, the unique nature of each -1 PRF signal may allay this concern. On a positive note, since the -1 PRF signals of each virus are highly conserved, this mitigates worries about drug-resistant bypass mutations. As we try to peer over the horizon to prevent the next pandemic(s), -1 PRF represents an important target to add to the arsenal of antiviral therapeutic strategies.

2.4.2 Unraveling structures and mechanisms of the SARS-CoV-2 RNA frameshifting element by graph theory and molecular modeling

Nucleic Despite the ongoing vaccination campaigns across the world, we are entering the third year of the COVID-19 pandemic with new waves of infection by SARS-CoV-2 and witnessing mutations that continue to evade our immune system while producing alarming symptoms in increasing cohorts and parts of the world. It has become clear that simple solutions are difficult and that more fundamental scientific knowledge, as well as clinical evidence, is required to address current and future viral infections that inevitably will arise.

Fortunately, the level of scientific cooperation and advances we have witnessed since early 2020 offers hope. Besides successful vaccine development efforts, progress on unraveling the complex and multifarious biophysical aspects of the virus life cycle and infection trajectory has helped us describe how the virus hijacks our own protein-synthesis machinery into making viral proteins efficiently and propose new lines of defense against the deadly disease it carries. These insights into the life cycle of the virus and mode of action are invaluable for further development of drugs and other strategies to combat current and future viral epidemics.

Investigations of the RNA viral agent itself are crucial for understanding how the RNA invader replicates itself, is translated by the human ribosomal machinery, assembles, and synthesizes a suite of viral proteins that enable the continuation of its invasive trajectory. Importantly, RNA-targeting therapeutics and vaccines can disarm the origin of the infection rather than its products and potentially be more effective in the long term. However, the complexity of the RNA molecule and the lagging science about its modeling, imaging, and drug screening, as compared to proteins, poses several challenges. With technological

improvements in RNA delivery systems, the rise of CRISPR-based gene editing systems [57, 58], and improved RNA modeling techniques [59, 60], this RNA focus is not only warranted but clearly successful, as evidenced by recent mRNA-based vaccines.

Of particular interest by many groups is the RNA frameshifting element (FSE), a small region in the open reading frame ORF1a,b region (Figure 5A) of the viral genome that codes for the polyproteins that initiate the cascade of viral protein synthesis. The FSE is responsible for the crucial −1 PRF mechanism utilized by many viruses, including HIV-1, to handle protein synthesis from overlapping reading frames [61-63]. A pseudoknot (intertwined hydrogen-bonding), or a stem-loop motif, is believed to be crucial for the requisite pausing associated with frameshifting [63-65].

When encountering ORF1b, out of register with respect to ORF1a, the ribosome backs up one nucleotide in the 5' direction to define a different sequence of codons (Figure 5). Because studies indicate correlations between the FSE conformational plasticity and frameshifting efficiency, it is likely that more complex conformational mechanisms are involved rather than a simple "barrier" [42, 66-68]. Indeed, the discovery of many alternative conformations of the SARS-CoV-2 FSE [50, 69-78] suggest a complex conformational and thermodynamic landscape.

The FSE's crucial role in viral protein synthesis makes it an excellent target for therapeutic intervention [42, 79, 80]. Already, small-molecule agents such as 1,4-diazepane derivative 10 (MTDB) (originally designed for SARS-CoV [68, 81, 82]), fluoroquinolone antibacterial merafloxacin [74], and a phenyl thiourea C5[83] were found to hamper SARS-CoV-2 frameshifting. However, a mechanistic understanding of the process and the drug effect is unknown. Complexity is inherent in the makeup and variability of the FSE region. The 84-

residue SARS-CoV-2 FSE (13462–13545 of the 29891 nt RNA genome) contains a 7-residue slippery site (UUUAAAC) and a 77-residue conformationally flexible region (Figure 5). Besides the folds and mechanisms of the RNA FSE itself, important interactions are involved between the FSE and the ribosome during viral protein synthesis.

The Schlick group focuses on better understanding the conformational landscape of the FSE using a combination of complementary graph-based modeling and chemical reactivity and other experiments. Already, several groups have explored FSE structure by modeling [49, 69, 77, 78, 84], in vivo Selective 2'-Hydroxyl Acylation by Primer Extension (SHAPE) [85, 86] and DMS structure probing experiments [50, 70-76], NMR [87], Cryo-EM [50, 51], and other biophysical mutational profiling and scanning approaches [82, 88, 89].

Many have characterized the FSE of SARS-CoV-2 as a 3-stem hairpin (H-type) pseudoknot with colinear Stems 1 and 2 intertwined via a pseudoknot and perpendicular Stem 3. This association has persisted from the SARS-CoV FSE characterization [82], which differs in only one base from the SARS-CoV-2 FSE (residue A13533 in Covid-19 is C in SARS, Figure 5). However, depending on the modeling software and experimental technique, alternative secondary structures have been reported for SARS-CoV-2, both pseudoknotted and unknotted [50, 69-78].

Developing further and applying the RNA-As-Graphs (RAG) graph-theory tools for handling pseudoknots [90-94] to the SARS-CoV-2 FSE, the Schlick group has designed double mutants, shown in Figure 5B, that dramatically alter the FSE conformation (see [84] and accompanying New & Notable commentary [95]). These mutations define target residues for drug binding and gene editing. By further probing the FSE structure as a function of length and performing chemical reactivity experiments with SHAPE, we have described alternative

forms of the FSE [96]. Notably, the combined complex conformational landscape has three viable structures of the FSE: two 3-stem pseudoknotted RNAs (3_6 and 3_3 in the dual graph notation), and one unknotted, 3-way junction RNA (3_5) (Figure 5B). The flexible Stem 2 may be involved in a switch between these conformations and associations with the ribosome during protein translation, as well as define a co-transcriptional kinetic folding trap. For whole genome constructs, a stem-loop motif (2_2 graph) may also compete with these forms. In addition, we confirmed experimentally that other designed FSE mutants stabilize one conformation over all others [97], lending confidence in these mutational transformations. These conformation-specific mutations may be particularly effective when used in combination with anti-viral compounds that target a specific FSE form. The Schlick group's recent molecular dynamics studies of these alternative conformations at various lengths suggest key transition states that are shared by all three FSE conformations and, importantly, pathways for inter-conversion among them [97]. These studies also point to several therapeutic avenues, including interference with FSE transformations, FSE/ribosome interactions, and FSE folding. Ongoing research is addressing these possible therapeutic avenues as well as the dynamic mechanisms associated with frameshifting.

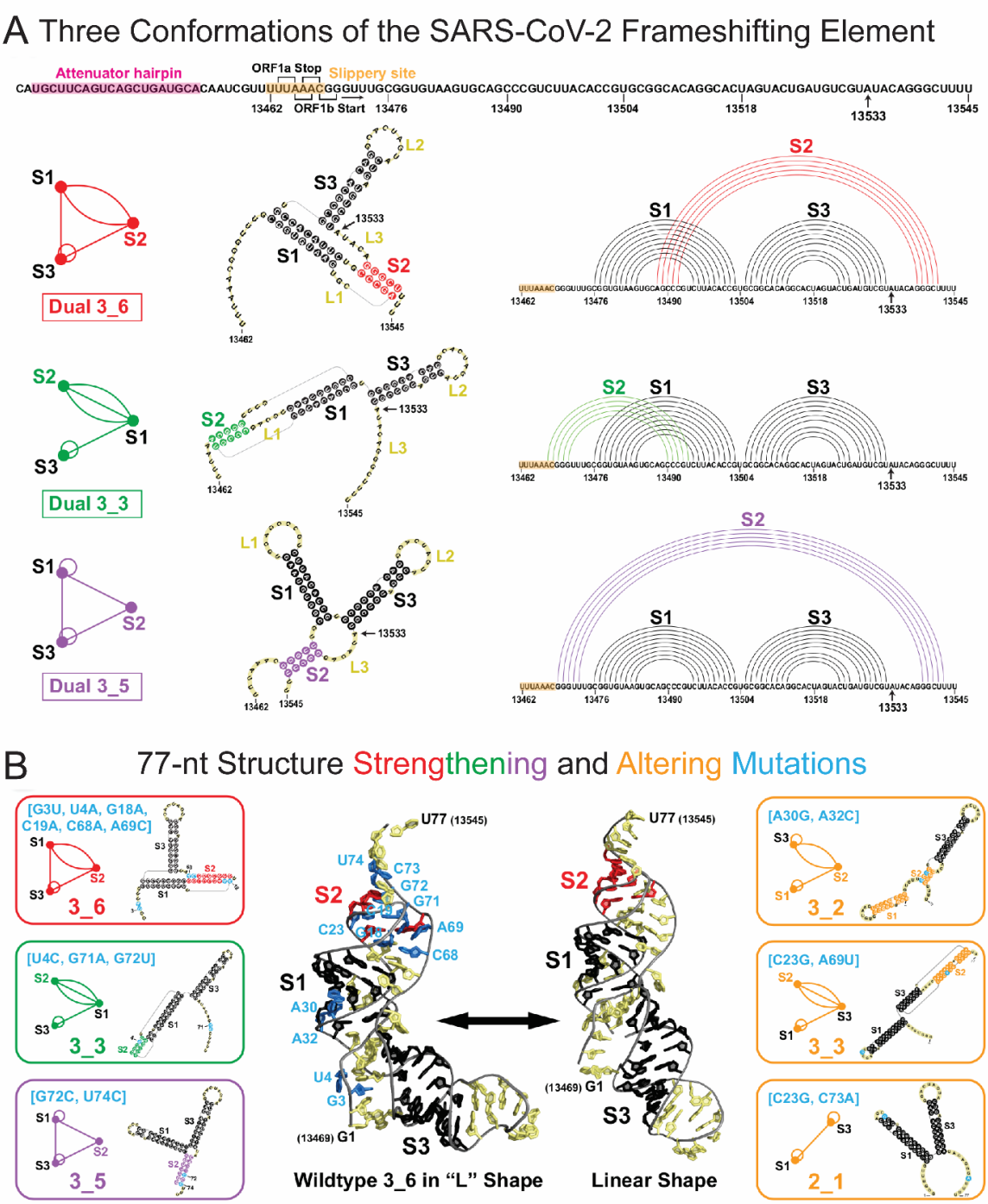

Figure 5. FSE sequence, three relevant 2D structures for the SARS-CoV-2 84 nt FSE (residues 13462–13545) emerging from the Schlick group's work [84, 96] and mutants that transform the 3_6 motif and stabilize all conformers, using graph based models, 2D structure prediction, SHAPE structural probing, thermodynamic ensemble modeling, and molecular dynamics simulations [97]. (A) The −1 frameshifting moves the transcript UUU-UU*A(Leu)-AAC(Asn)-GGG at the second codon (asterisk) to start as AAA-CGG(Arg), so that translation resumes at

CGG. Top: FSE sequence, with the attenuator hairpin region, the 7 nt slippery site, and A13533 labeled (C in SARS). The ORF1a end and ORF1b start codons for the overlapping regions are marked. For each 2D structure, 3_6 pseudoknot, 3_3 pseudoknot, and three-way junction 3_5 (unknotted RNA), we show corresponding dual graphs, 2D structures, and arc plots, with color-coded stems and loops. (B), Left: Mutants that stabilize each conformer; (B), Right: Double mutants that transform the 3_6 form into other RNAs. B, Middle: Straight to L-shape transition captured in the simulation for wild type 3_6 system, which is suppressed in the 3_6 stabilizing mutant.

2.5 RNA Structure and Assessment

2.5.1 End-to-end prediction of RNA base pairing structures through deep transfer learning of evolution and co-evolution information

Predicting RNA secondary structure has long been dominated by folding-based algorithms, which require a scoring function coupled with a minimum-searching algorithm. These predictions, however, are often limited to nested and stacked canonical base pairs (i.e., AU and GC Watson-Crick and GU wobble base pairs), while ignoring other hydrogen-bonded bases stabilized by tertiary interactions. The ignorance reflects the difficulty to predict “tertiary” base pairs without knowing three-dimensional structures. Structure-stabilized base pairs include un-nested (pseudoknot), noncanonical and isolated lone base pairs as well as base triplets. Thus, a gold-standard dataset for these “tertiary” base pairs requires experimentally determined three-dimensional structures. However, there are only a few thousand RNA structures that have been solved so far. Such a small number of RNA structures makes it challenging to apply deep learning to RNA structure prediction.

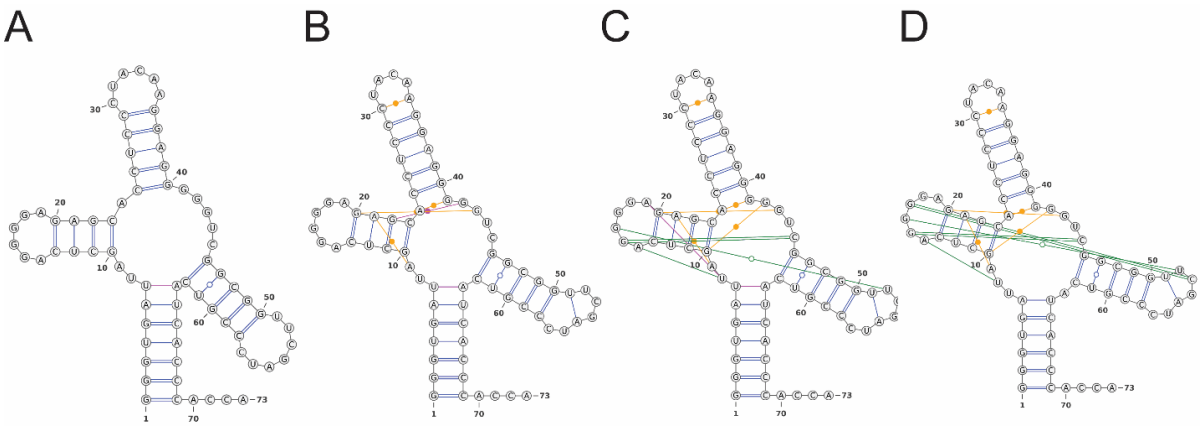

Figure 6. Base pair prediction for 70S ribosome (PDB 6CAE, chain 1Y) by (A) CentroidAlifold [PR=95, SN=67], (B) SPOT-RNA [PR= 93, SN=83], and (C) SPOT-RNA2 [PR=94, SN=97], compared to (D) the native as labelled. All false positives are shown in red. Tertiary base pairs (noncanonical base pairs in orange and pseudoknots in green) are the most visible improvement from the traditional folding algorithm (CentroidAlifold, limited to canonical base pairs in blue) to SPOT-RNA without evolution information and SPOT-RNA2 with evolution information. Copyright (2021) Oxford University Press.

Recently, Singh et al. showed that the above problem can be addressed by using a highly accurate but approximate database of RNA secondary structures for initial training [98]. The initial training is followed by transfer learning with a small dataset of full base-pairing structures derived from RNA structures. The resulting method called SPOT-RNA showed that a single sequence (i.e., without information of homologous sequences) can provide a significant improvement over the stagnant accuracy of secondary structure prediction by folding-based algorithms in recent years. The most significant improvement is in “tertiary” base pairs such as pseudoknots, noncanonical and lone base pairs.

To further improve the above prediction, it is necessary to incorporate sequence conservation and co-variation information as in proteins. However, unlike proteins, 4-letter coded RNA can easily lose their sequence identity in evolution. Thus, it is necessary to incorporate structural information in homology search as has been done in INFERNAL [99], which searches homology sequences using a secondary-structure-based covariance model.

RNAcmap is the first fully automatic pipeline that performs homology search, multiple sequence alignment, and direct coupling/co-mutational analysis in a single run [100]. Incorporating sequence profiles and mutational coupling generated by RNAcmap yields another significant improvement in RNA secondary structure prediction (SPOT-RNA2 [101]) and distance-based contact prediction (SPOT-RNA-2D [102]) for those RNAs with a significant number of homologous sequences, in particular. One example was shown in Figure 6, where SPOT-RNA2 provided accurate prediction of tertiary base pairs. The result highlights the usefulness of deep learning and multiple sequence alignment for the problems related to RNA structure prediction. RNAcmap, SPOT-RNA, SPOT-RNA2 and other RNA/protein-related tools (SPOT-RNA-1D for backbone structure [103] and RNAsnap2 for solvent accessibility [104]) are available for download or as online servers at http://sparks-lab.org.

Despite the above progress, many challenges remain. For example, RNA homologies remain difficult to find, for long RNA sequences (>1000 nucleotides) in particular [100]. Moreover, even with perfect contact maps as restraints, many RNA structures remain elusive [103] because RNA backbone structures have a much higher degree of freedom (6 torsion angles) than protein backbone structures (2 torsion angles). Better energy functions are certainly needed [105]. More importantly, the number of 3D structures in protein databank is insufficient for typical deep learning techniques. Thus, it is likely that a combination of deep learning with RNA-specific scoring/energy function is required to make significant progress in the foreseeable future [106].

2.5.2 Cryo-EM reveals conformational dynamics in a multifunctional viral RNA

Development of new nanotechnologies based on engineered RNA structures depends on knowledge of the fundamental properties of RNA folding and its conformational

dynamics [107]. The modular architecture of RNA can be exploited to rationally build RNA structures [108, 109], but we need to solve the structures of more, and more dynamic, RNA structures to understand underlying principles and discover conformationally dynamic 'building blocks' for use in RNA nanotechnology.

Viruses ubiquitously use structured RNA elements as part of their overall infection strategy, and for regulating the formation of the capsid [110-113]. Many structured viral RNA elements are multifunctional, a feature that may depend on conformational changes programmed into the RNA structure. Thus, explorations of these RNA elements can yield new tools for RNA nanotechnology while revealing fundamental features of RNA folding and dynamics. Although traditional structural methods are ill-suited for large, structurally dynamic RNAs, advances in cryo-electron microscopy (cryo-EM) may provide a new way to explore these RNAs.

Examples of structured, multifunctional, and perhaps conformationally dynamic RNA elements are the tyrosine-accepting tRNA-like structures (TLSTyr). TLSTyr are found at the 3' end of specific single-stranded positive-sense RNA viral genomes [114, 115]. They are aminoacylated by the host cell's tyrosine aminoacyl tRNA synthetase (Tyr-AARS) and regulate several viral processes. These characteristics suggest TLSTyr are tRNA mimics that undergo programmed conformational changes, but their structure had remained elusive for decades.

The Kieft group has used single-particle cryo-EM to solve the structure of a representative TLSTyr RNA (~55 kDa) in both its unbound form and bound to Tyr-AARS (Figure 7) [116]. The unbound RNA comprises a complex structure of multiple helical elements emanating from a central junction. Surprisingly, the structure does not directly mimic tRNA,

suggesting it must change conformation to productively bind the Tyr-AARS. Further analyses revealed that the part of the RNA that acts as the anticodon loop mimic is within a conformationally mobile domain. The structure of the TLSTyr RNA in the Tyr-AARS-bound state subsequently showed that this mobile domain adopts a position at a roughly right angle to its position in the unbound state. This mode of binding differs dramatically and unexpectedly from that of an authentic tRNA.

These findings show that programmed conformational dynamics are an inherent and necessary component of TLSTyr RNA's ability to hijack the host cell synthetase. Furthermore, there exist two distinct bound states, one in which the TLSTyr RNA is making limited contact with the enzyme and one in which the 3' end of the RNA is 'pulled into' the enzyme's active site. Although we cannot ascribe an order of events to these states, they suggest a multistep mechanism of binding that may be more generally applicable. Overall, these studies show the power of cryo-EM to detect and characterize conformational changes in RNAs that have been largely intractable by other methods.

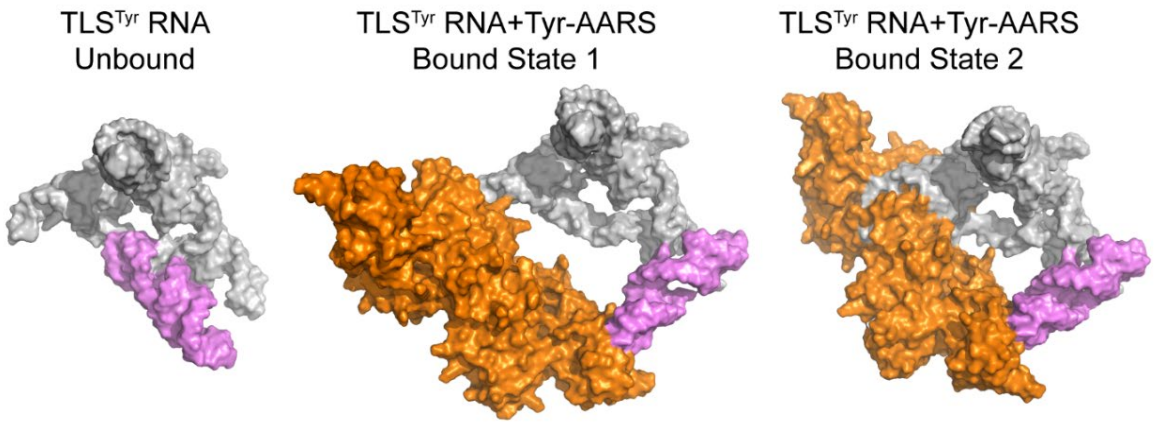

Figure 7. Structure of a TLSTyr RNA (grey and purple) in the unbound form (left) and bound to a Tyr-AARS, which is colored orange (center and right). Solvent-accessible surfaces are shown. The purple TLSTyr RNA domain is dynamic relative to the rest of the molecule (grey), adopting different positions in the unbound versus bound states.

2.5.3 Correlating SHAPE data to RNA 3D structure

The talk from Shi-Jie Chen's research group from the University of Missouri, Columbia, focused on a novel method for data-assisted RNA structure prediction. As a readily available alternative to x-ray footprinting of RNA for assessing secondary and tertiary structures which does not require the use of a synchrotron, selective 2'-hydroxyl acylation analyzed by primer extension (SHAPE) provides insights into the flexibility of nucleotides [117, 118]. A SHAPE ligand such as 1-methyl-7-nitroisatoic anhydride (1M7) reacts with nucleotides in the flexible regions of RNA (flexible loops) and does not react with nucleotides in rigid regions (helices, rigid loops). SHAPE is known to supply effective constraints for the prediction of a 2D structure (base pairs)[85]. However, nucleotide flexibility is determined by atomic interactions, which is 3D. Thus, SHAPE reactivity is intrinsically tied to the 3D structure of RNA. The Chen lab has developed, SHAPER[119-121], a web server (URL: http://rna.physics.missouri.edu/shaper/) that can compute the SHAPE profile from a 3D RNA structure. Combined with computer simulations that can generate a pool of candidate 3D structures, SHAPER would provide a novel, SHAPE data-driven, method to efficiently identify the native structure or near-native structures by removing SHAPE-incompatible structures from the pool of candidate structures.

The key product of the model is a new estimator of SHAPE reactivity for each nucleotide in a given 3D structure[85, 119]. The main driver of the prediction is the energy-like score that connects the SHAPE reactivity profile to the energetics of the nucleotide. This SHAPE energy score is related the 3D interaction energy that combines the effects of base pairing and stacking to estimate the interaction strength for a nucleotide. This score also accounts for several key factors including ligand accessibility, sugar conformation, and the effect of

terminal residues due to alterations of the terminal regions of the RNA during the experiment. Because a SHAPE reaction occurs at the 2'-OH, the SHAPE ligand has to access the space between the nucleotide being scored and the nucleotide directly downstream, so the interaction strength of these two nucleotides with other members of the RNA and the 5' to 3' polarity of the nucleotide interactions are very important to the ability of the SHAPE ligand to react. Furthermore, Chen lab found that including the non-nearest-neighbor interactions of these nucleotides is also important in estimating the SHAPE reactivity.

Overall, this new model displays substantial promise in the assessment tested. For a structure, the Pearson correlation is calculated between the predicted SHAPE profile and the experimental profile. The result (Figure 8) of the Spearman rank correlation between the Pearson correlation and the interaction network fidelity (INF) show that the model is able to discern between near-native and non-native structures with a high degree of accuracy. Taken together, these results suggest that the model is both sensitive and accurate in identifying the native or near-native 3D folds of an RNA. Combined with SHAPE data, the model would provide a powerful tool for RNA nanoparticle design based on the desired RNA native structures [122-128], RNA conformational changes [129-132], and RNA-ligand interactions [133-135].

There are two major challenges to the SHAPER model. First, the SHAPE data used to train the model are from various systems and may rely on different data processing of the raw data. Therefore, the model may suffer from the quality of the training data set. This has been shown by a previous attempt of using machine learning to predict the SHAPE profile from a 3D RNA structure [136]. Second, the correlation between intra-molecular interactions and SHAPE reactivity is not fully clear, which would directly impact the reliability of the model. In future developments, more high-quality SHAPE data needs to be collected for different

RNA structures, in particular, for RNA nanoparticle structures. With such data, the SHAPR model will be refined to more effectively and accurately sieve incorrect 3D folds and identify the correct native structures for RNA nanoparticles. Furthermore, future development of the SHAPER model should rely on a rigorous model for intramolecular interactions, in particular, for the non-canonical base-pairing interactions in different tertiary structural motifs. Better models of the interactions demand more biophysical data on RNA structure and stability.

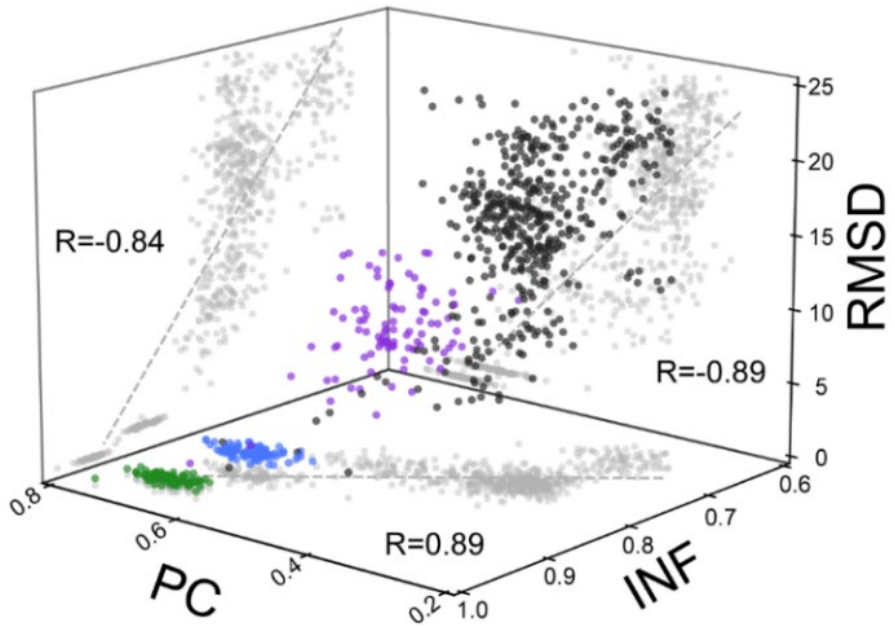

Figure 8 The figure shows the trends between the Pearson correlation, INF and RMSD for Lysine riboswitch (PDBID: 3DIG). The INF is a measure that captures native interactions, so the reference native structure has an INF of 1. The RMSD is the root mean squared deviation of the structure, so the reference native structure has an RMSD of 0. Structures in the green region are the decoys generated from a simulation of the native RNA with the backbone and base pairs restrained. The blue region represents a similar ensemble of structures, except that

the base pairs are no longer restrained while the backbone atoms are restrained to maintain the global folding. Structures in the purple region are the decoys generated from coarse-grained simulations with the base pairs enforced, but no backbone restraints. The black region shows an ensemble of alternative (nonnative) low-energy 2D structure decoys generated from coarse-grained simulations. The projections of the decoy structures are shown as shadows in each 2D plane. We see that as the INF increases and RMSD decreases, i.e., as the structure approaches the native state, the Pearson correlation between the SHAPER prediction of the SHAPE reactivity and the experimental SHAPE reactivity of the structures increases, indicating that the model is successful in estimating the SHAPE reactivity for decoy structures. This may be used for predictive purposes. By sieving low-energy decoys, the model can improve predictions RNA structure prediction by removing structures that are incompatible with SHAPE data.

2.5.4 Integrating molecular dynamics simulations and SAXS data

Small angle X-ray scattering (SAXS) experiments are valuable in providing information about size and shape of RNA molecules and thus optimally complement other biophysical techniques [137, 138]. Given their low resolution, SAXS data must be integrated with accurate modeling tools so as to provide detailed structural information. For a single molecule in vacuum, frozen in a single conformation, scattering intensities are straightforwardly related to the radial Fourier transform of the atomic coordinates. However, for biomolecules in solution, two additional factors might make the interpretation more difficult, namely (a) the contribution of the solvent and (b) the presence of multiple alternative conformations in the same buffer (RNA dynamics).

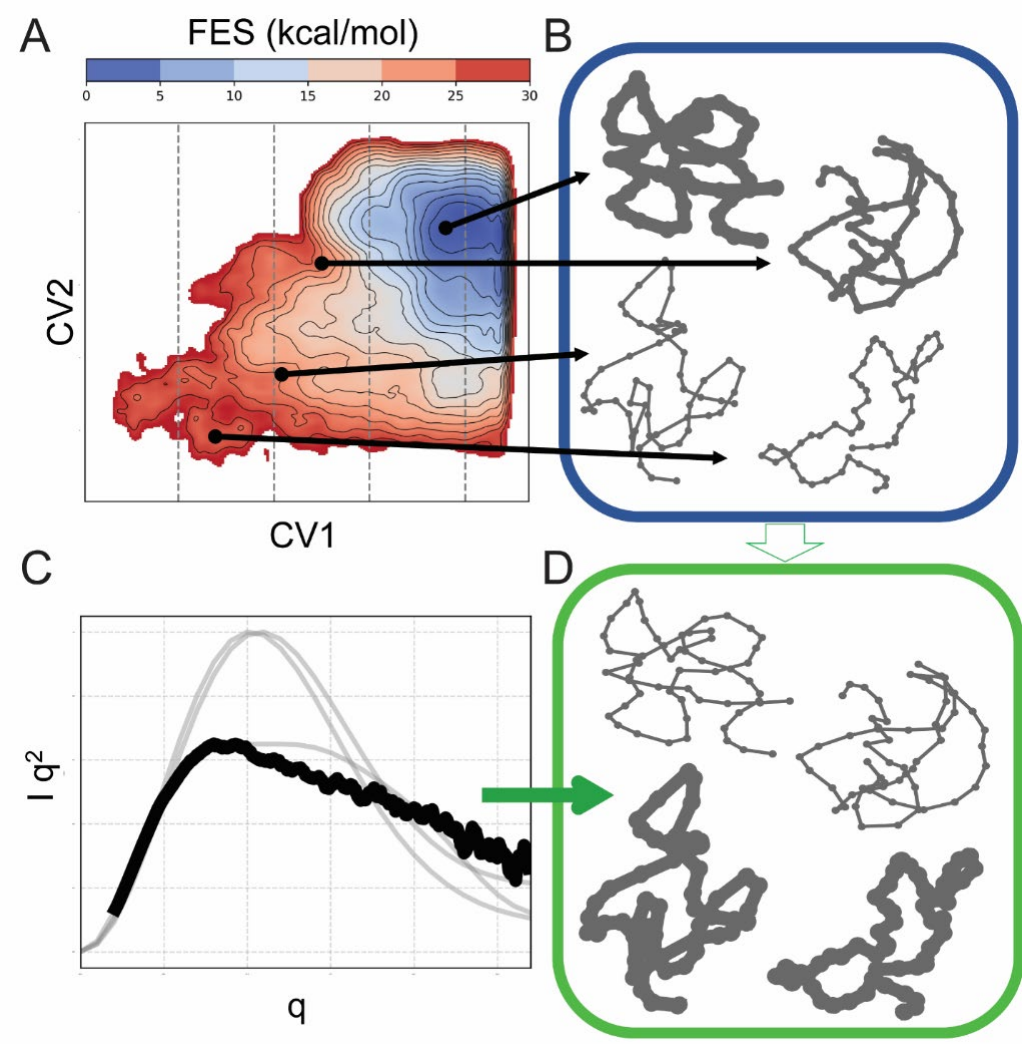

Figure 9. Integrating enhanced sampling simulations and SAXS data. (A) Molecular dynamics simulations with enhanced sampling techniques allow the extraction of a free energy surface (FES) as a function of one or more collective variables (CV1 and CV2). (B) The generated ensemble contains both compact and extended structures, and associates them with a population. (C) SAXS experiments at different ion concentrations provide a spectrum that is affected by solvent effects and ensemble averages. (D) The combination of molecular dynamics and experiments allow RNA dynamics to be reconstructed at atomistic resolution. Copyright (2021) Oxford University Press.

Molecular dynamics simulations allow for RNA dynamics to be investigated at atomistic resolution and are currently a standard tool for structural biology studies [139]. Notably, they can be combined with SAXS data so as to provide an interpretation of the experiment at atomic resolution [140]. In theory, they allow both factors mentioned above to be considered.

Solvent effects can indeed be included by explicitly subtracting a separate buffer simulation, similarly to what is done in experiments [141, 142]. At the same time, the presence of multiple conformations naturally arises from the spontaneous structural fluctuations, which can be directly averaged. Given the typical timescales required for RNA conformation changes, this can only be obtained by using suitably designed enhanced sampling methods [143]. These two ideas have been however rarely combined.

In a recent work [144] (see also Figure 9), the Bussi group has shown how solvent effects and RNA dynamics can be brought together to characterize the ion-dependent population of compact and extended states of the GTPase-associated center, an RNA molecule involved in protein translation for which SAXS data were previously reported [145]. Specifically, an enhanced sampling method [146] was used that encourages the exploration of structures with heterogeneous SAXS spectra, by quickly estimating spectra on-the-fly without including solvent effects [147]. This allowed to generate an ensemble consisting of a mixture of compact and extended structures. The SAXS spectra for the generated ensembles were then reconstructed by explicitly including water contributions and modeling the experimental buffer subtraction [141], and use the maximum entropy principle to reweight the results so as to match experiments [148]. The results show that different populations of compact and extended states are required based on the type and concentration of ions present in the buffer.

Overall, these results show that both conformational dynamics and solvent effects play an important role in SAXS spectra of RNA, and indeed, neither of the two effects can separately account for the experimental results. The importance of the solvent might be ascribed to the highly charged nature of RNA. At the same time, the observation that rich and heterogeneous

conformational ensembles are required to match experiments underlines the importance of RNA dynamics in analyzing data obtained in solution.

Given the relative simplicity of small (and wide) angle X-ray scattering experiments (SAXS and WAXS) when compared to other biophysical techniques, as well as their capability to capture dynamical effects, the application of these techniques to RNA systems is gaining momentum. At the same time, several methods are emerging to combine them with molecular modeling techniques so as to extract the maximum amount of information. We believe that this field will see other methodological developments in the next few years. In addition to methods based on maximizing entropy, such as the one discussed above, other techniques based on the maximum parsimony principle, such as sample-and-select, have been recently applied to RNA [149]. These techniques have the advantage of reporting a limited number of structural models, and thus provide more interpretable results, at the price of ignoring a possibly relevant fraction of conformation dynamics. A future challenge in the field is certainly the synergistic integration of these ideas so as to combine their benefits. Finally, it is important to recognize that the applicability of atomistic molecular dynamics simulations to medium-sized (50–100 nucleotides) RNAs is extremely expensive, especially in the most interesting cases where conformational dynamics is important. The field will thus certainly benefit from the development and availability of novel enhanced sampling methods based on the application of machine learning techniques [150]. An alternative approach is that of using coarse-grained models that have an inherent advantage when compared to MD in their capability to quickly generate large sets of heterogeneous structures [151]. Hence, we believe that future research should be aimed at developing methods to increase the accuracy in the

back-calculation of SAXS and WAXS spectra when using coarse-grained representations of RNAs.

2.6 RNA Nanotechnology

2.6.1 The dynamic property of RNA leads the emerging field of RNA nanotechnology

RNA folds into thermostable structures and nanocomplexes with defined stoichiometry, size, and shape from one or multiple RNA oligo strands [152-162]. RNA ensemble structures hold a higher level of apparent entropy (S), or structural disorder than DNA, despite RNA possessing more a compact helical region [107, 152, 161]. Helical regions of RNA are highly structured and inflexible, but other elements, such as loops and bulges, are capable of dynamic motions capable of interacting with small molecules and receptors via induced fit models [153]. The high level of entropy and the ability for dynamic motions allow for RNA to have the property of movement, motion, and deform shapes much like an amoeba. This amoeba-like property has often been encompassed in a worm/snake-like chain structural model and possesses unique biodistribution properties [163, 164].

Methods for examining the motion and movement of RNA utilize nuclear magnetic resonance (NMR) [154-159], X-ray crystallography [165, 166], single-molecule imaging microscopy [167-169], and cryogenic electron microscopy (cryo-EM) [169, 170].

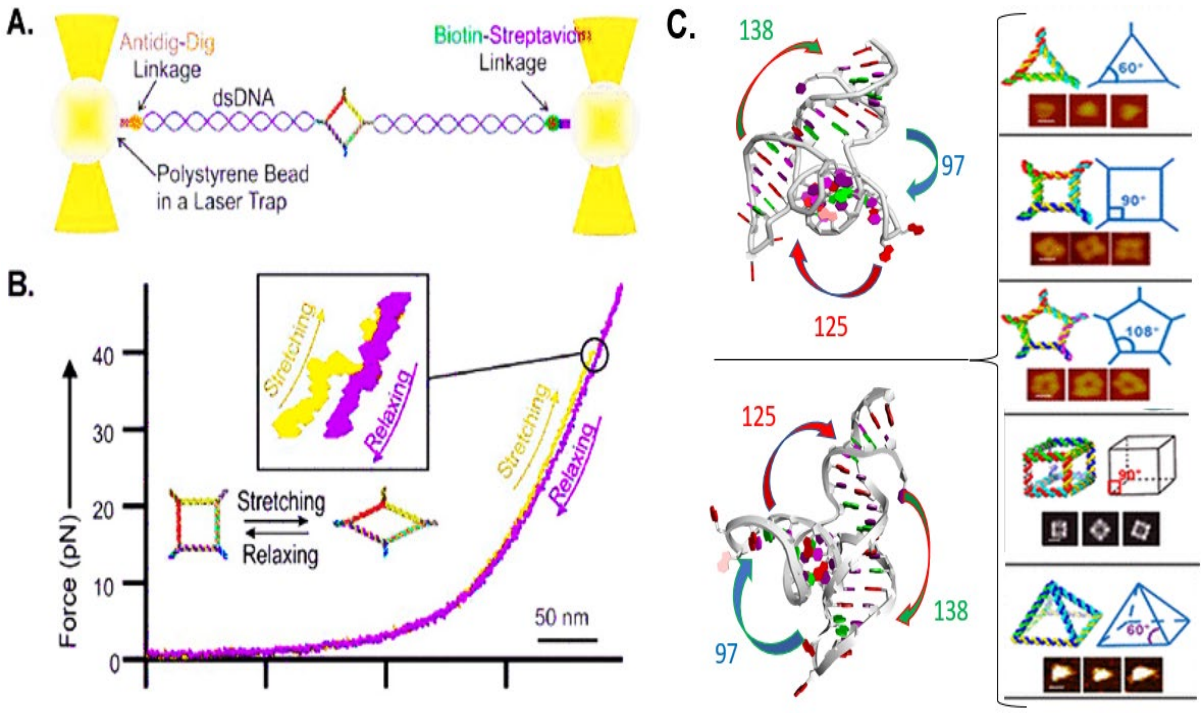

Figure 10. RNA nanoparticles stretched via dual trap optical tweezer by Guo and colleagues. (A) Dual trap optical tweezers with tethered RNA construct between two dsDNA handles via affinity linkers. (B) Control force–extension curve for stretching (red) and relaxing (black) of RNA nanoparticle as a square. Inset: Point at which the nanoparticle undergoes conformational change in response to force. [171] (C) RNA nanostructures constructed through using the dynamic property of pRNA 3WJ its natural angles of 97, 138, and 125 respectively, tunable past its these natural angles to 60°, 90°, and 108° respectively. [172] (A-B) Reprinted (adapted) with permission from Ghimire et al 2019. Copyright 2019 American Chemical Society. (C) Copyright 2014 Oxford University Press.

RNA moves to change conformations in the presence of a ligand during the binding of proteins, or when undergoing co-transcriptional dynamic folding and restructuring, demonstrating movement during enzymatic behaviors in accordance with the induced fit model of substrate ligand interactions [153, 160-162, 166]. Besides mRNA, rRNA, and tRNA, cells contain many other noncoding RNA for critical functions in the regulation of basic cellular functions [173-175]. The dynamic nature of RNA results in its motile and deformative behavior which is interacting with a large variety of cellular functions aside from post-transcriptional and translational functions. This deformative property is highlighted in Figure 10.

Conformational transitions change base-pairing, breathing within complemented strands [176], and pseudoknot formation at a 2D level [177], as well as the induced-fit [178] and conformation capture at the 3D level [179] which are important for biological functions including regulation, translation, and catalysis. The dynamic conformational transition follows the nearest neighbour principle to determine an ensemble of transient states with respective Gibbs free energies sitting around the "lowest" Gibbs free energy state which are adopted at any moment [180]. The dynamic, motile, and catalytic activity has led to a belief that RNA is the origin of life in the RNA world hypothesis, underscoring the interest in understanding RNA structural dynamics [181]. This deformative property of RNA nanoparticles enhances their trans vascular permeability past the leaky blood vessels associated with angiogenesis while also rapidly passing the glomerular membrane for rapid body clearance. The biodistribution of RNA nanoparticles can be further improved by the incorporation of ligands for entry into solid tumours with extensive vascular networks [164]. The negative charge of RNA decreases the toxicity of drugs carried by this platform by preventing nonspecific binding to the negative charge cell membrane while enhancing the solubility of hydrophobic drugs for favourable hemodynamics[182]. These unique properties of RNA nanoparticles and the mechanism of RNA dynamic, motile and deformative properties were presented at the meeting to welcome RNA therapeutics as the third milestone in pharmaceutical drug development.

2.6.2 Strand displacement in Nucleic Acid Nanotechnology

Strand displacement is a reaction between DNA or RNA strands that is essential to dynamic nucleic acid nanotechnology, and has been used in nucleic acid circuits designed for molecular computing, as well as in synthetic biology and molecular sensing[183]. Furthermore,

there is increasingly more evidence that strand displacement is also involved in numerous naturally occurring processes, such as during RNA cotranscriptional folding or during RNA invasion into double-stranded DNA in the CRISPR-Cas9 complex[184].

The Sulc group has studied toehold mediated strand displacement reaction (TMSD)[185-187]. It consists of an invader strand that binds to a complementary strand (substrate) that has been previously bound to another complementary strand (incumbent) (Figure 11). The substrate strand has a single-stranded overhang (toehold) to which the invader bounds prior to removing the incumbent.

While the kinetics and thermodynamics of the TMSD reaction between DNA strands has been studied in detail for DNA nanotechnology via computational and experimental studies, there has not been a systematic study of such systems experimentally carried out when RNA strands are involved. Experiments have also not been carried out for hybrid reactions, where either RNA invades a DNA duplex, thus creating RNA-DNA hybrid, or when DNA strands invades an RNA duplex. The Sulc group has performed an experimental study where they varied the length of the toehold for RNA TMSD, as well as introduced mismatches between the invader and the substrate. Through this work, it was found that increasing toehold length speeds up the reaction exponentially, as was previously observed for DNA. Introducing mismatches slows the reaction, and the closer the mismatch is to the interface of the toehold / incumbent strand, the larger the slow-down. For a six-nucleotide toehold, it was observed that RNA invading an RNA duplex is faster than RNA invading a DNA duplex. For a toehold of length 3 nucleotides, they found RNA invading DNA to be faster than RNA invading RNA.

It should be noted that these studies are just a first step towards understanding the strand displacement kinetics that involves hybrid DNA-RNA systems. Such systems are still not integrated into available simulations and the design tools that our community uses to design and test strand displacement circuits. The studies which involve invasion (of DNA or RNA) into DNA-RNA hybrid circuits have not been performed yet, and testing of effects of different sequences and positioning on the 5' or 3' end of substrate is also needed for better understanding of RNA TMSD reaction. Finally, while the thermodynamics of DNA and RNA duplexes has been carefully studied over the years, and is currently incorporated into widely used dynamic programming tools for secondary structure prediction such as NUPACK or RNAStructure, the free energies of fully complementary DNA-RNA hybrids were measured in the above work. The thermodynamics of mismatches in DNA-RNA hybrids has still not been measured.

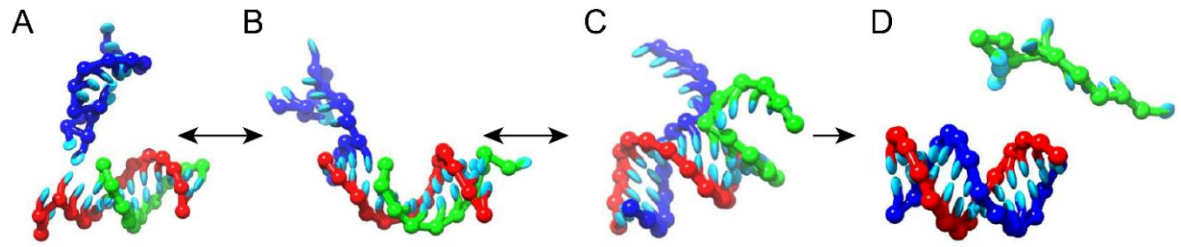

Figure 11. A schematic representation of the toehold-mediated strand displacement reaction that was previously simulated with a coarse-grained RNA model. (A) Invader starts to bind to toehold. (B) Invader strand fully bound to the toehold. (C) Invader starts to replace base pairs between the incumbent and the substrate. (D) Invader fully replaces all bonds between the incumbent and the substrate.

2.6.3 Rationally designed nucleic acid nanoparticles (NANPs) with regulated immune recognition

As was revealed by the COVID-19 pandemic, there are numerous biological challenges that we are not prepared for[8, 188]. Nevertheless, while the same risks still exist for

many other pathogens and diseases, there is now an enormous potential available for accelerated solutions that can be provided for future health threats.

With traditional small molecule drugs, there are two main components -- the dianophore that defines drug's biodistribution and pharmacokinetics, and the pharmacophore that determines its targeted function and biological responses. Therefore, even minor changes to a chemical composition of a small molecule drug can have drastic effects on its function and distribution and consequently, would require its complete re-evaluation[189]. In contrast, the separation of the dianophore and pharmacophore components yields a more modular therapeutic approach. In the case of therapeutic nucleic acids (TNAs), the backbone chemistry and the sequence define the dianophore and the pharmacophore components, respectively. This modularity allows for a tighter control over therapeutic characteristics of the drug and by changing ether chemical makeup of the backbone or the sequence of TNAs, the new therapeutic effect can be predicted and tuned as required for specific functions.

On top of being used as therapeutics, nucleic acids can now be employed as nanoscaffolds to coordinate simultaneous delivery of multiple different TNAs that are intended for synchronized action in the same diseased cell[190, 191]. These nucleic acid nanoparticles, or NANPs, are rationally designed to self-assemble into specific structures[192] that gain pre-defined architectural and physicochemical parameters[193]. Furthermore, NANPs can be programmed to carry multiple functionalities embedded in their structures that all together can be activated to target multiple pathways in a particular disease.

Due to the intended applications, it becomes important to understand how NANPs interact with the human innate immune system, evolutionary equipped with the diverse set of pattern recognition receptors (PRRs) that act specifically against non-self nucleic acids.

During the extensive course of systematic studies in clinically relevant model systems, several important factors responsible for NANPs' immune recognition have been discovered[6, 7, 193-203]. For example, carrier molecules are required for the intracellular delivery of NANPs and their immunorecognition. In addition, the carrier provides extensive protection for NANPs from degradation by nucleases and defines NANPs biodistribution. Without any carriers, all tested NANPs have been effectively invisible to the cells of the immune system. Toll-like receptors in endosomal compartments are the first line of defense against NANPs that undergo scavenger receptor mediated endocytosis and there are various mechanisms with which the immune system responds to NANPs. The recognition of NANPs by human immune cells normally activates a complex network of signaling cascades with excreted interferons being produced as key cytokines. Upon the assessment of immunostimulatory properties of a representative set of NANPs, their dimensionality (1D, 2D, or 3D), composition (RNA vs DNA), and extend of functionalization were found to be the main contributors to the immunostimulation (Figure 12).

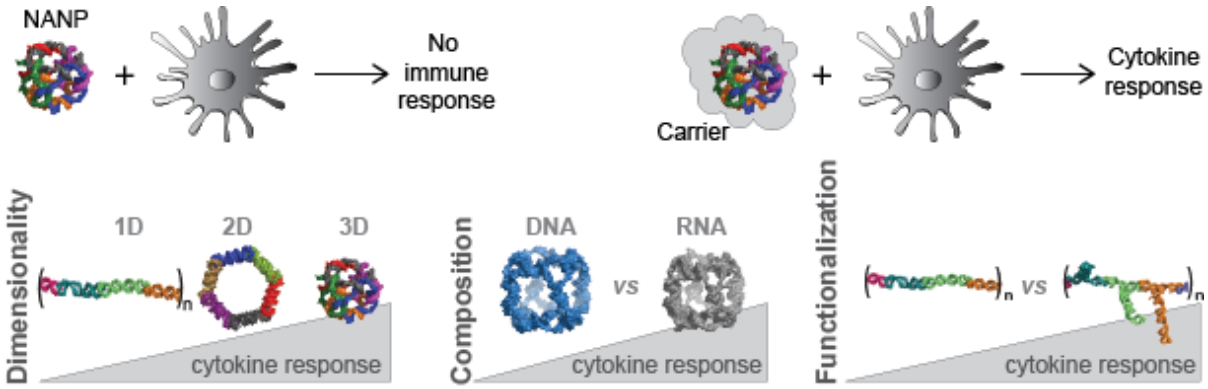

Figure 12. The immunorecognition of NANPs is defined by their structure, composition, functionalization and require the use of delivery agents.

Mechanistic studies helped to disseminate how NANPs can be recognized by the immune cell machinery to trigger the observed immune responses. For example, endosomal

TLR7 and TLR9 and a cytosolic RIG-I have been identified to be important regulators of NANPs' immune recognition by human immune cells[193, 194, 196, 204]. The chemical composition of NANPs also defines their interactions with PRRs as well as their localization within a cell. For example, while in the cytoplasm, some RNA made NANPs may be recognized by RIG-I and DNA hybrids with 2` fluorination can be recognized by RNA polymerase III that transcribes RNAs amenable for detection by RIG-I [196].

Overall, NANPs technology introduces a unique class of therapeutics that bring new possibilities for immunotherapies and targeted drug delivery with their structural versatilities. These particles have the potential to interact with human immune system in unique ways and, if designed correctly, can become a basis for a new class of safe and effective therapeutics. The knowledge and experience we gained by now are testimony to NANPs' potential. Further studies of how NANPs produce the observed immunological effects will pave the way for novel applications.

2.7 References

1. Chandler, M.; Johnson, B.; Khisamutdinov, E.; Dobrovolskaia, M. A.; Sztuba-Solinska, J.; Salem, A. K.; Breyne, K.; Chammas, R.; Walter, N. G.; Contreras, L. M.; et al. The International Society of RNA Nanotechnology and Nanomedicine (ISRNN): The Present and Future of the Burgeoning Field. *ACS Nano* **2021**. DOI: 10.1021/acsnano.0c10240.

2. Afonin, Kirill A.; Dobrovolskaia, Marina A.; Ke, Weina; Grodzinski, Piotr; Bathe, Mark. Critical review of nucleic acid nanotechnology to identify gaps and inform a strategy for accelerated clinical translation. *Advanced Drug Delivery Reviews* **2022**, *181*, 114081. DOI: https://doi.org/10.1016/j.addr.2021.114081.

3. Damase, T. R.; Sukhovershin, R.; Boada, C.; Taraballi, F.; Pettigrew, R. I.; Cooke, J. P. The Limitless Future of RNA Therapeutics. *Front Bioeng Biotechnol* **2021**, *9*, 628137. DOI: 10.3389/fbioe.2021.628137.

4. Afonin, Kirill A.; Dobrovolskaia, Marina A.; Church, George; Bathe, Mark. Opportunities, Barriers, and a Strategy for Overcoming Translational Challenges to Therapeutic Nucleic Acid Nanotechnology. *ACS Nano* **2020**, *14* (8), 9221-9227. DOI: 10.1021/acsnano.0c04753 (acccessed 2021-01-04T20:59:11).

5. Anh Lam, Phuong; Furr, Daniel P.; Tran, Allison; McKeough, Riley Q.; Beasock, Damian; Chandler, Morgan; Afonin, Kirill A.; Trammell, Susan R. The Application of Light-Assisted Drying to the Thermal Stabilization of Nucleic Acid Nanoparticles. *Biopreservation and Biobanking* **2022**. DOI: 10.1089/bio.2022.0035 (acccessed 2022/10/25).

6. Chandler, Morgan; Jain, Sankalp; Halman, Justin; Hong, Enping; Dobrovolskaia, Marina A.; Zakharov, Alexey V.; Afonin, Kirill A. Artificial Immune Cell, AI-cell, a New Tool to Predict Interferon Production by Peripheral Blood Monocytes in Response to Nucleic Acid Nanoparticles. *Small (Weinheim an der Bergstrasse, Germany)* **2022**, *n/a* (n/a), 2204941, https://doi.org/10.1002/smll.202204941. DOI: https://doi.org/10.1002/smll.202204941 (acccessed 2022/10/25).

7. Tran, Allison N.; Chandler, Morgan; Halman, Justin; Beasock, Damian; Fessler, Adam; McKeough, Riley Q.; Lam, Phuong Anh; Furr, Daniel P.; Wang, Jian; Cedrone, Edward; et al. Anhydrous Nucleic Acid Nanoparticles for Storage and Handling at Broad Range of Temperatures. *Small (Weinheim an der Bergstrasse, Germany)* **2022**, *n/a* (n/a), 2104814, https://doi.org/10.1002/smll.202104814. DOI: https://doi.org/10.1002/smll.202104814 (acccessed 2022/03/11).

8. Vishweshwaraiah, Yashavantha L.; Hnath, Brianna; Rackley, Brendan; Wang, Jian; Gontu, Abhinay; Chandler, Morgan; Afonin, Kirill A.; Kuchipudi, Suresh V.; Christensen, Neil; Yennawar, Neela H.; et al. Adaptation-Proof SARS-CoV-2 Vaccine Design. *Advanced Functional Materials* **2022**, *n/a* (n/a), 2206055, https://doi.org/10.1002/adfm.202206055. DOI: https://doi.org/10.1002/adfm.202206055 (acccessed 2022/10/25).

9. Kefauver, J. M.; Ward, A. B.; Patapoutian, A. Discoveries in structure and physiology of mechanically activated ion channels. *Nature* **2020**, *587* (7835), 567-576. DOI: 10.1038/s41586-020-2933-1.

10. Jin, P.; Bulkley, D.; Guo, Y.; Zhang, W.; Guo, Z.; Huynh, W.; Wu, S.; Meltzer, S.; Cheng, T.; Jan, L. Y.; et al. Electron cryo-microscopy structure of the mechanotransduction channel NOMPC. *Nature* **2017**, *547* (7661), 118-122. DOI: 10.1038/nature22981.

11. Wang, Y.; Guo, Y.; Li, G.; Liu, C.; Wang, L.; Zhang, A.; Yan, Z.; Song, C. The push-to-open mechanism of the tethered mechanosensitive ion channel NompC. *Elife* **2021**, *10*. DOI: 10.7554/eLife.58388.

12. Das, Ravi; Lin, Li-Chun; Català-Castro, Frederic; Malaiwong, Nawaphat; Sanfeliu-Cerdán, Neus; Porta-de-la-Riva, Montserrat; Pidde, Aleksandra; Krieg, Michael. An asymmetric mechanical code ciphers curvature-dependent proprioceptor activity. *Science Advances* **2021**, *7* (38), eabg4617. DOI: doi:10.1126/sciadv.abg4617.

13. Liang, C.; Weitao, T.; Zhou, L.; Guo, P. Translation of the long-term fundamental studies on viral DNA packaging motors into nanotechnology and nanomedicine. *Sci China Life Sci* **2020**, *63* (8), 1103-1129. DOI: 10.1007/s11427-020-1752-1.

14. Guo, P.; Zhao, Z.; Haak, J.; Wang, S.; Wu, D.; Meng, B; Weitao, T. Common Mechanisms of DNA translocation motors in Bacteria and Viruses Using One-way Revolution Mechanism without Rotation. *Biotechnology Advances* **2014**, *32*, 853-872.

15. Hugel, T.; Michaelis, J.; Hetherington, C.L.; Jardine, P.J.; Grimes, S.; Walter, J.M.; Faik, W.; Anderson, D.L.; Bustamante, C. Experimental test of connector rotation during DNA packaging into bacteriophage phi29 capsids. *Plos Biology* **2007**, *5*, 558-567.

16. De-Donatis, G.; Zhao, Z.; Wang, S.; Huang, P.L.; Schwartz, C.; Tsodikov, V.O.; Zhang, H.; Haque, F.; Guo, P. Finding of widespread viral and bacterial revolution dsDNA translocation motors distinct from rotation motors by channel chirality and size. *Cell Biosci* **2014**, *4*, 30.

17. Schwartz, C.; De Donatis, G.M.; Zhang, H.; Fang, H.; Guo, P. Revolution rather than rotation of AAA+ hexameric phi29 nanomotor for viral dsDNA packaging without coiling. *Virology* **2013**, *443*, 28-39.

18. Liang, C.; Guo, P. Identification of Arginine Finger as the Starter of the Biomimetic Motor in Driving Double-Stranded DNA. *ACS Nano* **2021**, *15* (8), 13260-13266. DOI: 10.1021/acsnano.1c02973 From NLM.

19. Guo, P.; Driver, D.; Zhao, Z.; Zheng, Z.; Chan, C.; Cheng, X. Controlling the Revolving and Rotating Motion Direction of Asymmetric Hexameric Nanomotor by Arginine Finger and Channel Chirality. *ACS Nano* **2019**, *13* (6), 6207-6223. DOI: 10.1021/acsnano.8b08849 From NLM.

20. Yang, Y.; Yang, P.; Wang, N.; Chen, Z.; Su, D.; Zhou, Z. H.; Rao, Z.; Wang, X. Architecture of the herpesvirus genome-packaging complex and implications for DNA translocation. *Protein Cell* **2020**. DOI: 10.1007/s13238-020-00710-0 From NLM.

21. Jean, N. L.; Rutherford, T. J.; Löwe, J. FtsK in motion reveals its mechanism for double-stranded DNA translocation. *Proceedings of the National Academy of Sciences of the United States of America* **2020**, *117* (25), 14202-14208. DOI: 10.1073/pnas.2001324117 From NLM.

22. Amado, E.; Muth, G.; Arechaga, I.; Cabezón, E. The FtsK-like motor TraB is a DNA-dependent ATPase that forms higher-order assemblies. *J Biol Chem* **2019**, *294* (13), 5050-5059. DOI: 10.1074/jbc.RA119.007459 From NLM.

23. Lhuillier, Sophie; Gallopin, Matthieu; Gilquin, Bernard; Brasilès, Sandrine; Lancelot, Nathalie; Letellier, Guillaume; Gilles, Mathilde; Dethan, Guillaume; Orlova, Elena V.; Couprie, Joël; et al. Structure of bacteriophage SPP1 head-to-tail connection reveals mechanism for viral DNA gating. *Proceedings of the National Academy of Sciences* **2009**, *106* (21), 8507-8512. DOI: 10.1073/pnas.0812407106 (acccessed 2022/11/04).

24. Liu, Y.; Wang, K.; Wang, Y.; Wang, L.; Yan, S.; Du, X.; Zhang, P.; Chen, H. Y.; Huang, S. Machine Learning Assisted Simultaneous Structural Profiling of Differently Charged Proteins in a Mycobacterium smegmatis Porin A (MspA) Electroosmotic Trap. *Journal of the American Chemical Society* **2022**, *144* (2), 757-768. DOI: 10.1021/jacs.1c09259.

25. Tripathi, Prabhat; Chandler, Morgan; Maffeo, Christopher Michael; Fallahi, Ali; Makhamreh, Amr; Halman, Justin; Aksimentiev, Aleksei; Afonin, Kirill A.; Wanunu, Meni. Discrimination of RNA fiber structures using solid-state nanopores. *Nanoscale* **2022**. DOI: 10.1039/d1nr08002d (acccessed 2022-04-22T16:42:00).

26. Boersma, A. J.; Bayley, H. Continuous stochastic detection of amino acid enantiomers with a protein nanopore. *Angew Chem Int Ed Engl* **2012**, *51* (38), 9606-9609. DOI: 10.1002/anie.201205687.

27. Ji, Z.; Guo, P. Channel from bacterial virus T7 DNA packaging motor for the differentiation of peptides composed of a mixture of acidic and basic amino acids. *Biomaterials* **2019**, *214*, 119222. DOI: 10.1016/j.biomaterials.2019.119222 From NLM.

28. Ouldali, H.; Sarthak, K.; Ensslen, T.; Piguet, F.; Manivet, P.; Pelta, J.; Behrends, J. C.; Aksimentiev, A.; Oukhaled, A. Electrical recognition of the twenty proteinogenic amino acids using an aerolysin nanopore. *Nat Biotechnol* **2020**, *38* (2), 176-181. DOI: 10.1038/s41587-019-0345-2 From NLM.

29. Wang, S.; Zhou, Z.; Zhao, Z.; Zhang, H.; Haque, F.; Guo, P. Channel of viral DNA packaging motor for real time kinetic analysis of peptide oxidation states. *Biomaterials* **2017**, *126*, 10-17. DOI: 10.1016/j.biomaterials.2017.01.031 From NLM.

30. Rosen, C. B.; Rodriguez-Larrea, D.; Bayley, H. Single-molecule site-specific detection of protein phosphorylation with a nanopore. *Nat Biotechnol* **2014**, *32* (2), 179-181. DOI: 10.1038/nbt.2799.

31. Zhang, L.; Gardner, M. L.; Jayasinghe, L.; Jordan, M.; Aldana, J.; Burns, N.; Freitas, M. A.; Guo, P. Detection of single peptide with only one amino acid modification via electronic fingerprinting using reengineered durable channel of Phi29 DNA packaging motor. *Biomaterials* **2021**, *276*, 121022. DOI: 10.1016/j.biomaterials.2021.121022 From NLM.

32. Zhou, Z.; Ji, Z.; Wang, S.; Haque, F.; Guo, P. Oriented single directional insertion of nanochannel of bacteriophage SPP1 DNA packaging motor into lipid bilayer via polar hydrophobicity. *Biomaterials* **2016**, *105*, 222-227. DOI: 10.1016/j.biomaterials.2016.08.002 From NLM.

33. Ji, Z.; Jordan, M.; Jayasinghe, L.; Guo, P. Insertion of channel of phi29 DNA packaging motor into polymer membrane for high-throughput sensing. *Nanomedicine* **2020**, *25*, 102170. DOI: 10.1016/j.nano.2020.102170 From NLM.

34. Yan, S.; Zhang, J.; Wang, Y.; Guo, W.; Zhang, S.; Liu, Y.; Cao, J.; Wang, Y.; Wang, L.; Ma, F.; et al. Single Molecule Ratcheting Motion of Peptides in a Mycobacterium smegmatis Porin A (MspA) Nanopore. *Nano letters* **2021**, *21* (15), 6703-6710. DOI: 10.1021/acs.nanolett.1c02371.

35. Zhang, L.; Burns, N.; Jordan, M.; Jayasinghe, L.; Guo, P. Macromolecule sensing and tumor biomarker detection by harnessing terminal size and hydrophobicity of viral DNA packaging motor channels into membranes and flow cells. *Biomater Sci* **2021**, *10* (1), 167-177. DOI: 10.1039/d1bm01264a From NLM.

36. Afshar Bakshloo, M.; Kasianowicz, J. J.; Pastoriza-Gallego, M.; Mathe, J.; Daniel, R.; Piguet, F.; Oukhaled, A. Nanopore-Based Protein Identification. *Journal of the American Chemical Society* **2022**, *144* (6), 2716-2725. DOI: 10.1021/jacs.1c11758.

37. Lucas, F. L. R.; Versloot, R. C. A.; Yakovlieva, L.; Walvoort, M. T. C.; Maglia, G. Protein identification by nanopore peptide profiling. *Nature communications* **2021**, *12* (1), 5795. DOI: 10.1038/s41467-021-26046-9.

38. Wu, J.; Wang, X.; Wang, Q.; Lou, Z.; Li, S.; Zhu, Y.; Qin, L.; Wei, H. Nanomaterials with enzyme-like characteristics (nanozymes): next-generation artificial enzymes (II). *Chem Soc Rev* **2019**, *48* (4), 1004-1076. DOI: 10.1039/c8cs00457a From NLM.

39. Shen, Xiaomei; Wang, Zhenzhen; Gao, Xingfa; Zhao, Yuliang. Density Functional Theory-Based Method to Predict the Activities of Nanomaterials as Peroxidase Mimics. *ACS Catalysis* **2020**, *10* (21), 12657-12665. DOI: 10.1021/acscatal.0c03426.

40. Wang, Zhenzhen; Shen, Xiaomei; Gao, Xingfa; Zhao, Yuliang. Simultaneous enzyme mimicking and chemical reduction mechanisms for nanoceria as a bio-antioxidant: a catalytic model bridging computations and experiments for nanozymes. *Nanoscale* **2019**, *11* (28), 13289-13299, 10.1039/C9NR03473K. DOI: 10.1039/C9NR03473K.

41. Wang, Zhenzhen; Wu, Jiangjiexing; Zheng, Jia-Jia; Shen, Xiaomei; Yan, Liang; Wei, Hui; Gao, Xingfa; Zhao, Yuliang. Accelerated discovery of superoxide-dismutase nanozymes via high-throughput computational screening. *Nature communications* **2021**, *12* (1), 6866. DOI: 10.1038/s41467-021-27194-8.

42. Kelly, J. A.; Woodside, M. T.; Dinman, J. D. Programmed -1 Ribosomal Frameshifting in coronaviruses: A therapeutic target. *Virology* **2021**, *554*, 75-82. DOI: 10.1016/j.virol.2020.12.010.

43. Dever, T. E.; Dinman, J. D.; Green, R. Translation Elongation and Recoding in Eukaryotes. *Cold Spring Harb Perspect Biol* **2018**, *10* (8). DOI: 10.1101/cshperspect.a032649.

44. Halma, M. T. J.; Ritchie, D. B.; Woodside, M. T. Conformational Shannon Entropy of mRNA Structures from Force Spectroscopy Measurements Predicts the Efficiency of -1 Programmed Ribosomal Frameshift Stimulation. *Phys Rev Lett* **2021**, *126* (3), 038102. DOI: 10.1103/PhysRevLett.126.038102.

45. Dinman, J. D.; Wickner, R. B. Ribosomal frameshifting efficiency and gag/gag-pol ratio are critical for yeast M1 double-stranded RNA virus propagation. *J Virol* **1992**, *66* (6), 3669-3676. DOI: 10.1128/JVI.66.6.3669-3676.1992.

46. Hung, M.; Patel, P.; Davis, S.; Green, S. R. Importance of ribosomal frameshifting for human immunodeficiency virus type 1 particle assembly and replication. *J Virol* **1998**, *72* (6), 4819-4824. DOI: 10.1128/JVI.72.6.4819-4824.1998.

47. Plant, E. P.; Sims, A. C.; Baric, R. S.; Dinman, J. D.; Taylor, D. R. Altering SARS coronavirus frameshift efficiency affects genomic and subgenomic RNA production. *Viruses* **2013**, *5* (1), 279-294. DOI: 10.3390/v5010279.

48. Kendra, J. A.; de la Fuente, C.; Brahms, A.; Woodson, C.; Bell, T. M.; Chen, B.; Khan, Y. A.; Jacobs, J. L.; Kehn-Hall, K.; Dinman, J. D. Ablation of Programmed -1 Ribosomal Frameshifting in Venezuelan Equine Encephalitis Virus Results in Attenuated Neuropathogenicity. *J Virol* **2017**, *91* (3). DOI: 10.1128/JVI.01766-16.

49. Omar, S. I.; Zhao, M.; Sekar, R. V.; Moghadam, S. A.; Tuszynski, J. A.; Woodside, M. T. Modeling the structure of the frameshift-stimulatory pseudoknot in SARS-CoV-2 reveals multiple possible conformers. *PLoS Comput Biol* **2021**, *17* (1), e1008603. DOI: 10.1371/journal.pcbi.1008603.

50. Zhang, K.; Zheludev, I. N.; Hagey, R. J.; Haslecker, R.; Hou, Y. J.; Kretsch, R.; Pintilie, G. D.; Rangan, R.; Kladwang, W.; Li, S.; et al. Cryo-EM and antisense targeting of the 28-kDa frameshift stimulation element from the SARS-CoV-2 RNA genome. *Nat Struct Mol Biol* **2021**, *28* (9), 747-754. DOI: 10.1038/s41594-021-00653-y.

51. Bhatt, P. R.; Scaiola, A.; Loughran, G.; Leibundgut, M.; Kratzel, A.; Meurs, R.; Dreos, R.; O'Connor, K. M.; McMillan, A.; Bode, J. W.; et al. Structural basis of ribosomal

frameshifting during translation of the SARS-CoV-2 RNA genome. *Science* **2021**, *372* (6548), 1306-1313. DOI: 10.1126/science.abf3546.

52. Chen, Y.; Tao, H.; Shen, S.; Miao, Z.; Li, L.; Jia, Y.; Zhang, H.; Bai, X.; Fu, X. A drug screening toolkit based on the -1 ribosomal frameshifting of SARS-CoV-2. *Heliyon* **2020**, *6* (8), e04793. DOI: 10.1016/j.heliyon.2020.e04793.

53. Sun, Y.; Abriola, L.; Niederer, R. O.; Pedersen, S. F.; Alfajaro, M. M.; Silva Monteiro, V.; Wilen, C. B.; Ho, Y. C.; Gilbert, W. V.; Surovtseva, Y. V.; et al. Restriction of SARS-CoV-2 replication by targeting programmed -1 ribosomal frameshifting. *Proceedings of the National Academy of Sciences of the United States of America* **2021**, *118* (26). DOI: 10.1073/pnas.2023051118.

54. Munshi, Sneha; Neupane, Krishna; Ileperuma, Sandaru M.; Halma, Matthew T. J.; Kelly, Jamie A.; Halpern, Clarissa F.; Dinman, Jonathan D.; Loerch, Sarah; Woodside, Michael T. Small-molecule ligands can inhibit −1 programmed ribosomal frameshifting in a broad spectrum of coronaviruses. **2021**. DOI: 10.1101/2021.08.06.455424.

55. Belew, A. T.; Hepler, N. L.; Jacobs, J. L.; Dinman, J. D. PRFdb: a database of computationally predicted eukaryotic programmed -1 ribosomal frameshift signals. *BMC Genomics* **2008**, *9*, 339. DOI: 10.1186/1471-2164-9-339.

56. Mikl, M.; Pilpel, Y.; Segal, E. High-throughput interrogation of programmed ribosomal frameshifting in human cells. *Nature communications* **2020**, *11* (1), 3061. DOI: 10.1038/s41467-020-16961-8.

57. Hermann, T. Small molecules targeting viral RNA. *Wiley Interdiscip Rev RNA* **2016**, *7* (6), 726-743. DOI: 10.1002/wrna.1373.

58. Nguyen, T. M.; Zhang, Y.; Pandolfi, P. P. Virus against virus: a potential treatment for 2019-nCov (SARS-CoV-2) and other RNA viruses. *Cell Res* **2020**, *30* (3), 189-190. DOI: 10.1038/s41422-020-0290-0.

59. Miao, Z.; Adamiak, R. W.; Antczak, M.; Boniecki, M. J.; Bujnicki, J.; Chen, S. J.; Cheng, C. Y.; Cheng, Y.; Chou, F. C.; Das, R.; et al. RNA-Puzzles Round IV: 3D structure predictions of four ribozymes and two aptamers. *RNA* **2020**, *26* (8), 982-995. DOI: 10.1261/rna.075341.120.

60. Sun, L. Z.; Zhang, D.; Chen, S. J. Theory and Modeling of RNA Structure and Interactions with Metal Ions and Small Molecules. *Annu Rev Biophys* **2017**, *46*, 227-246. DOI: 10.1146/annurev-biophys-070816-033920.

61. Brierley, I. Ribosomal frameshifting viral RNAs. *J Gen Virol* **1995**, *76 (Pt 8)*, 1885-1892. DOI: 10.1099/0022-1317-76-8-1885.

62. Atkins, J. F.; Loughran, G.; Bhatt, P. R.; Firth, A. E.; Baranov, P. V. Ribosomal frameshifting and transcriptional slippage: From genetic steganography and cryptography to adventitious use. *Nucleic Acids Res* **2016**, *44* (15), 7007-7078. DOI: 10.1093/nar/gkw530.

63. Staple, D. W.; Butcher, S. E. Solution structure of the HIV-1 frameshift inducing stem-loop RNA. *Nucleic Acids Res* **2003**, *31* (15), 4326-4331. DOI: 10.1093/nar/gkg654.

64. Brierley, I.; Digard, P.; Inglis, S. C. Characterization of an efficient coronavirus ribosomal frameshifting signal: requirement for an RNA pseudoknot. *Cell* **1989**, *57* (4), 537-547. DOI: 10.1016/0092-8674(89)90124-4.

65. Somogyi, P.; Jenner, A. J.; Brierley, I.; Inglis, S. C. Ribosomal pausing during translation of an RNA pseudoknot. *Molecular and Cellular Biology* **1993**, *13* (11), 6931-6940. DOI: 10.1128/mcb.13.11.6931.

66. Namy, O.; Moran, S. J.; Stuart, D. I.; Gilbert, R. J.; Brierley, I. A mechanical explanation of RNA pseudoknot function in programmed ribosomal frameshifting. *Nature* **2006**, *441* (7090), 244-247. DOI: 10.1038/nature04735.

67. Ritchie, D. B.; Foster, D. A.; Woodside, M. T. Programmed -1 frameshifting efficiency correlates with RNA pseudoknot conformational plasticity, not resistance to mechanical unfolding. *Proceedings of the National Academy of Sciences of the United States of America* **2012**, *109* (40), 16167-16172. DOI: 10.1073/pnas.1204114109.

68. Ritchie, D. B.; Soong, J.; Sikkema, W. K.; Woodside, M. T. Anti-frameshifting ligand reduces the conformational plasticity of the SARS virus pseudoknot. *Journal of the American Chemical Society* **2014**, *136* (6), 2196-2199. DOI: 10.1021/ja410344b.

69. Trinity, Luke; Lansing, Lance; Jabbari, Hosna; Stege, Ulrike. SARS-CoV-2 ribosomal frameshifting pseudo- knot: Improved secondary structure prediction and detection of inter-viral structural similarity. **2020**. DOI: 10.1101/2020.09.15.298604.

70. Huston, N. C.; Wan, H.; de Cesaris Araujo Tavares, R.; Wilen, C.; Pyle, A. M. Comprehensive in-vivo secondary structure of the SARS-CoV-2 genome reveals novel regulatory motifs and mechanisms. *bioRxiv* **2020**. DOI: 10.1101/2020.07.10.197079.

71. Lan, Tammy C. T.; Allan, Matthew F.; Malsick, Lauren E.; Khandwala, Stuti; Nyeo, Sherry S. Y.; Sun, Yu; Guo, Junjie U.; Bathe, Mark; Griffiths, Anthony; Rouskin, Silvi. Insights into the secondary structural ensembles of the full SARS-CoV-2 RNA genome in infected cells. *bioRxiv* **2021**, 2020.2006.2029.178343. DOI: 10.1101/2020.06.29.178343.

72. Manfredonia, I.; Nithin, C.; Ponce-Salvatierra, A.; Ghosh, P.; Wirecki, T. K.; Marinus, T.; Ogando, N. S.; Snijder, E. J.; van Hemert, M. J.; Bujnicki, J. M.; et al. Genome-wide mapping of SARS-CoV-2 RNA structures identifies therapeutically-relevant elements. *Nucleic Acids Res* **2020**, *48* (22), 12436-12452. DOI: 10.1093/nar/gkaa1053.

73. Morandi, E.; Manfredonia, I.; Simon, L. M.; Anselmi, F.; van Hemert, M. J.; Oliviero, S.; Incarnato, D. Genome-scale deconvolution of RNA structure ensembles. *Nature methods* **2021**, *18* (3), 249-252. DOI: 10.1038/s41592-021-01075-w.

74. Sun, L.; Li, P.; Ju, X.; Rao, J.; Huang, W.; Ren, L.; Zhang, S.; Xiong, T.; Xu, K.; Zhou, X.; et al. In vivo structural characterization of the SARS-CoV-2 RNA genome

identifies host proteins vulnerable to repurposed drugs. *Cell* **2021**, *184* (7), 1865-1883 e1820. DOI: 10.1016/j.cell.2021.02.008.

75. Sanders, W.; Fritch, E. J.; Madden, E. A.; Graham, R. L.; Vincent, H. A.; Heise, M. T.; Baric, R. S.; Moorman, N. J. Comparative analysis of coronavirus genomic RNA structure reveals conservation in SARS-like coronaviruses. *bioRxiv* **2020**. DOI: 10.1101/2020.06.15.153197.

76. Iserman, C.; Roden, C. A.; Boerneke, M. A.; Sealfon, R. S. G.; McLaughlin, G. A.; Jungreis, I.; Fritch, E. J.; Hou, Y. J.; Ekena, J.; Weidmann, C. A.; et al. Genomic RNA Elements Drive Phase Separation of the SARS-CoV-2 Nucleocapsid. *Mol Cell* **2020**, *80* (6), 1078-1091 e1076. DOI: 10.1016/j.molcel.2020.11.041.

77. Andrews, R. J.; O'Leary, C. A.; Tompkins, V. S.; Peterson, J. M.; Haniff, H. S.; Williams, C.; Disney, M. D.; Moss, W. N. A map of the SARS-CoV-2 RNA structurome. *NAR Genom Bioinform* **2021**, *3* (2), lqab043. DOI: 10.1093/nargab/lqab043.

78. Ahmed, F.; Sharma, M.; Al-Ghamdi, A. A.; Al-Yami, S. M.; Al-Salami, A. M.; Refai, M. Y.; Warsi, M. K.; Howladar, S. M.; Baeshen, M. N. A Comprehensive Analysis of cis-Acting RNA Elements in the SARS-CoV-2 Genome by a Bioinformatics Approach. *Front Genet* **2020**, *11*, 572702. DOI: 10.3389/fgene.2020.572702.

79. Dinman, J. D.; Ruiz-Echevarria, M. J.; Czaplinski, K.; Peltz, S. W. Peptidyl-transferase inhibitors have antiviral properties by altering programmed -1 ribosomal frameshifting efficiencies: development of model systems. *Proceedings of the National Academy of Sciences of the United States of America* **1997**, *94* (13), 6606-6611. DOI: 10.1073/pnas.94.13.6606.

80. Goss Kinzy, T.; Harger, J. W.; Carr-Schmid, A.; Kwon, J.; Shastry, M.; Justice, M.; Dinman, J. D. New targets for antivirals: the ribosomal A-site and the factors that interact with it. *Virology* **2002**, *300* (1), 60-70. DOI: 10.1006/viro.2002.1567.

81. Park, S. J.; Kim, Y. G.; Park, H. J. Identification of RNA pseudoknot-binding ligand that inhibits the -1 ribosomal frameshifting of SARS-coronavirus by structure-based virtual screening. *Journal of the American Chemical Society* **2011**, *133* (26), 10094-10100. DOI: 10.1021/ja1098325.

82. Kelly, J. A.; Olson, A. N.; Neupane, K.; Munshi, S.; San Emeterio, J.; Pollack, L.; Woodside, M. T.; Dinman, J. D. Structural and functional conservation of the programmed -1 ribosomal frameshift signal of SARS coronavirus 2 (SARS-CoV-2). *J Biol Chem* **2020**, *295* (31), 10741-10748. DOI: 10.1074/jbc.AC120.013449.

83. Haniff, H. S.; Tong, Y.; Liu, X.; Chen, J. L.; Suresh, B. M.; Andrews, R. J.; Peterson, J. M.; O'Leary, C. A.; Benhamou, R. I.; Moss, W. N.; et al. Targeting the SARS-CoV-2 RNA Genome with Small Molecule Binders and Ribonuclease Targeting Chimera (RIBOTAC) Degraders. *ACS Cent Sci* **2020**, *6* (10), 1713-1721. DOI: 10.1021/acscentsci.0c00984.

84. Schlick, T.; Zhu, Q.; Jain, S.; Yan, S. Structure-altering mutations of the SARS-CoV-2 frameshifting RNA element. *Biophys J* **2021**, *120* (6), 1040-1053. DOI: 10.1016/j.bpj.2020.10.012.

85. Deigan, K. E.; Li, T. W.; Mathews, D. H.; Weeks, K. M. Accurate SHAPE-directed RNA structure determination. *Proceedings of the National Academy of Sciences of the United States of America* **2009**, *106* (1), 97-102. DOI: 10.1073/pnas.0806929106.

86. Smola, M. J.; Weeks, K. M. In-cell RNA structure probing with SHAPE-MaP. *Nature protocols* **2018**, *13* (6), 1181-1195. DOI: 10.1038/nprot.2018.010.

87. Wacker, A.; Weigand, J. E.; Akabayov, S. R.; Altincekic, N.; Bains, J. K.; Banijamali, E.; Binas, O.; Castillo-Martinez, J.; Cetiner, E.; Ceylan, B.; et al. Secondary structure determination of conserved SARS-CoV-2 RNA elements by NMR spectroscopy. *Nucleic Acids Res* **2020**, *48* (22), 12415-12435. DOI: 10.1093/nar/gkaa1013.

88. Rangan, R.; Zheludev, I. N.; Hagey, R. J.; Pham, E. A.; Wayment-Steele, H. K.; Glenn, J. S.; Das, R. RNA genome conservation and secondary structure in SARS-CoV-2 and SARS-related viruses: a first look. *RNA* **2020**, *26* (8), 937-959. DOI: 10.1261/rna.076141.120.

89. Ziv, O.; Price, J.; Shalamova, L.; Kamenova, T.; Goodfellow, I.; Weber, F.; Miska, E. A. The Short- and Long-Range RNA-RNA Interactome of SARS-CoV-2. *Mol Cell* **2020**, *80* (6), 1067-1077 e1065. DOI: 10.1016/j.molcel.2020.11.004.

90. Schlick, Tamar. *Molecular Modeling: An Interdisciplinary Guide*; Springer, 2010.

91. Schlick, T. Adventures with RNA graphs. *Methods* **2018**, *143*, 16-33. DOI: 10.1016/j.ymeth.2018.03.009.

92. Bayrak, C. S.; Kim, N.; Schlick, T. Using sequence signatures and kink-turn motifs in knowledge-based statistical potentials for RNA structure prediction. *Nucleic Acids Res* **2017**, *45* (9), 5414-5422. DOI: 10.1093/nar/gkx045.

93. Meng, G.; Tariq, M.; Jain, S.; Elmetwaly, S.; Schlick, T. RAG-Web: RNA structure prediction/design using RNA-As-Graphs. *Bioinformatics* **2020**, *36* (2), 647-648. DOI: 10.1093/bioinformatics/btz611.

94. Zhu, Qiyao; Petingi, Louis; Schlick, Tamar. RNA-As-Graphs Motif Atlas –Dual Graph Library of RNA Modules and Viral Frameshifting-Element Applications. In *International Journal of Molecular Sciences*, 2022; Vol. 23.

95. Chen, S. J. Graph, pseudoknot, and SARS-CoV-2 genomic RNA: A biophysical synthesis. *Biophys J* **2021**, *120* (6), 980-982. DOI: 10.1016/j.bpj.2021.01.030.

96. Schlick, T.; Zhu, Q.; Dey, A.; Jain, S.; Yan, S.; Laederach, A. To Knot or Not to Knot: Multiple Conformations of the SARS-CoV-2 Frameshifting RNA Element. *Journal of the American Chemical Society* **2021**, *143* (30), 11404-11422. DOI: 10.1021/jacs.1c03003.

97. Yan, S.; Zhu, Q.; Jain, S.; Schlick, T. Length-dependent motions of SARS-CoV-2 frameshifting RNA pseudoknot and alternative conformations suggest avenues for frameshifting suppression. *Res Sq* **2022**. DOI: 10.21203/rs.3.rs-1160075/v1.

98. Singh, J.; Hanson, J.; Paliwal, K.; Zhou, Y. RNA secondary structure prediction using an ensemble of two-dimensional deep neural networks and transfer learning. *Nature communications* **2019**, *10* (1), 5407. DOI: 10.1038/s41467-019-13395-9.

99. Nawrocki, E. P.; Eddy, S. R. Infernal 1.1: 100-fold faster RNA homology searches. *Bioinformatics* **2013**, *29* (22), 2933-2935. DOI: 10.1093/bioinformatics/btt509.

100. Zhang, T.; Singh, J.; Litfin, T.; Zhan, J.; Paliwal, K.; Zhou, Y. RNAcmap: A Fully Automatic Pipeline for Predicting Contact Maps of RNAs by Evolutionary Coupling Analysis. *Bioinformatics* **2021**. DOI: 10.1093/bioinformatics/btab391.

101. Singh, J.; Paliwal, K.; Zhang, T.; Singh, J.; Litfin, T.; Zhou, Y. Improved RNA Secondary Structure and Tertiary Base-pairing Prediction Using Evolutionary Profile, Mutational Coupling and Two-dimensional Transfer Learning. *Bioinformatics* **2021**. DOI: 10.1093/bioinformatics/btab165.

102. J. Singh, K. Paliwal, T. Litfin, J. Singh, and Y. Zhou. Predicting RNA distance-based contact maps by integrated deep learning on physics-inferred secondary structure and evolutionary-derived mutational coupling. *submitted (2022)* **2022**.

103. Singh, J.; Paliwal, K.; Singh, J.; Zhou, Y. RNA Backbone Torsion and Pseudotorsion Angle Prediction Using Dilated Convolutional Neural Networks. *J Chem Inf Model* **2021**, *61* (6), 2610-2622. DOI: 10.1021/acs.jcim.1c00153.

104. Hanumanthappa, A. K.; Singh, J.; Paliwal, K.; Singh, J.; Zhou, Y. Single-sequence and profile-based prediction of RNA solvent accessibility using dilated convolutional neural network. *Bioinformatics* **2021**, *36* (21), 5169-5176. DOI: 10.1093/bioinformatics/btaa652.

105. Xiong, P.; Wu, R.; Zhan, J.; Zhou, Y. Pairing a high-resolution statistical potential with a nucleobase-centric sampling algorithm for improving RNA model refinement. *Nature communications* **2021**, *12* (1), 2777. DOI: 10.1038/s41467-021-23100-4.

106. Townshend, R. J. L.; Eismann, S.; Watkins, A. M.; Rangan, R.; Karelina, M.; Das, R.; Dror, R. O. Geometric deep learning of RNA structure. *Science* **2021**, *373* (6558), 1047-1051. DOI: 10.1126/science.abe5650.

107. Ganser, L. R.; Kelly, M. L.; Herschlag, D.; Al-Hashimi, H. M. The roles of structural dynamics in the cellular functions of RNAs. *Nat Rev Mol Cell Biol* **2019**, *20* (8), 474-489. DOI: 10.1038/s41580-019-0136-0 From NLM.

108. Yesselman, J. D.; Eiler, D.; Carlson, E. D.; Gotrik, M. R.; d'Aquino, A. E.; Ooms, A. N.; Kladwang, W.; Carlson, P. D.; Shi, X.; Costantino, D. A.; et al. Computational design of three-dimensional RNA structure and function. *Nat Nanotechnol* **2019**, *14* (9), 866-873. DOI: 10.1038/s41565-019-0517-8.

109. Westhof, E.; Masquida, B.; Jaeger, L. RNA tectonics: towards RNA design. *Fold Des* **1996**, *1* (4), R78-88. DOI: 10.1016/S1359-0278(96)00037-5.

110. Jaafar, Z. A.; Kieft, J. S. Viral RNA structure-based strategies to manipulate translation. *Nat Rev Microbiol* **2019**, *17* (2), 110-123. DOI: 10.1038/s41579-018-0117-x.

111. Twarock, Reidun; Bingham, Richard J.; Dykeman, Eric C.; Stockley, Peter G. A modelling paradigm for RNA virus assembly. *Current Opinion in Virology* **2018**, *31*, 74-81. DOI: https://doi.org/10.1016/j.coviro.2018.07.003.

112. Twarock, Reidun; Stockley, Peter G. RNA-Mediated Virus Assembly: Mechanisms and Consequences for Viral Evolution and Therapy. *Annual Review of Biophysics* **2019**, *48* (1), 495-514. DOI: 10.1146/annurev-biophys-052118-115611 (acccessed 2022/10/24).

113. Tetter, Stephan; Terasaka, Naohiro; Steinauer, Angela; Bingham, Richard J.; Clark, Sam; Scott, Andrew J. P.; Patel, Nikesh; Leibundgut, Marc; Wroblewski, Emma; Ban, Nenad; et al. Evolution of a virus-like architecture and packaging mechanism in a repurposed bacterial protein. *Science* **2021**, *372* (6547), 1220-1224. DOI: 10.1126/science.abg2822 (acccessed 2022/10/24).

114. Dreher, T. W. Role of tRNA-like structures in controlling plant virus replication. *Virus Res* **2009**, *139* (2), 217-229. DOI: 10.1016/j.virusres.2008.06.010.

115. Dreher, T. W. Viral tRNAs and tRNA-like structures. *Wiley Interdiscip Rev RNA* **2010**, *1* (3), 402-414. DOI: 10.1002/wrna.42.

116. Bonilla, S. L.; Sherlock, M. E.; MacFadden, A.; Kieft, J. S. A viral RNA hijacks host machinery using dynamic conformational changes of a tRNA-like structure. *Science* **2021**, *374* (6570), 955-960. DOI: 10.1126/science.abe8526.

117. Merino, E. J.; Wilkinson, K. A.; Coughlan, J. L.; Weeks, K. M. RNA structure analysis at single nucleotide resolution by selective 2'-hydroxyl acylation and primer extension (SHAPE). *Journal of the American Chemical Society* **2005**, *127* (12), 4223-4231. DOI: 10.1021/ja043822v.

118. Chandler-Bostock, Rebecca; Bingham, Richard J.; Clark, Sam; Scott, Andrew J. P.; Wroblewski, Emma; Barker, Amy; White, Simon J.; Dykeman, Eric C.; Mata, Carlos P.; Bohon, Jen; et al. RNA X-ray footprinting reveals the consequences of an in vivo acquired determinant of viral infectivity. *bioRxiv* **2021**, 2021.2008.2010.455819. DOI: 10.1101/2021.08.10.455819.

119. Hurst, T.; Xu, X.; Zhao, P.; Chen, S. J. Quantitative Understanding of SHAPE Mechanism from RNA Structure and Dynamics Analysis. *J Phys Chem B* **2018**, *122* (18), 4771-4783. DOI: 10.1021/acs.jpcb.8b00575.

120. Hurst, T.; Chen, S. J. Sieving RNA 3D Structures with SHAPE and Evaluating Mechanisms Driving Sequence-Dependent Reactivity Bias. *J Phys Chem B* **2021**, *125* (4), 1156-1166. DOI: 10.1021/acs.jpcb.0c11365.

121. Zhou, Y.; Li, J.; Hurst, T.; Chen, S. J. SHAPER: A Web Server for Fast and Accurate SHAPE Reactivity Prediction. *Front Mol Biosci* **2021**, *8*, 721955. DOI: 10.3389/fmolb.2021.721955.

122. Cao, S.; Giedroc, D. P.; Chen, S. J. Predicting loop-helix tertiary structural contacts in RNA pseudoknots. *RNA* **2010**, *16* (3), 538-552. DOI: 10.1261/rna.1800210.

123. Li, J.; Chen, S. J. RNA 3D Structure Prediction Using Coarse-Grained Models. *Front Mol Biosci* **2021**, *8*, 720937. DOI: 10.3389/fmolb.2021.720937.

124. Zhang, D.; Chen, S. J. IsRNA: An Iterative Simulated Reference State Approach to Modeling Correlated Interactions in RNA Folding. *J Chem Theory Comput* **2018**, *14* (4), 2230-2239. DOI: 10.1021/acs.jctc.7b01228.

125. Zhang, D.; Li, J.; Chen, S. J. IsRNA1: De Novo Prediction and Blind Screening of RNA 3D Structures. *J Chem Theory Comput* **2021**, *17* (3), 1842-1857. DOI: 10.1021/acs.jctc.0c01148.

126. Zhang, D.; Chen, S. J.; Zhou, R. Modeling Noncanonical RNA Base Pairs by a Coarse-Grained IsRNA2 Model. *J Phys Chem B* **2021**, *125* (43), 11907-11915. DOI: 10.1021/acs.jpcb.1c07288.

127. Cao, S.; Chen, S. J. Free energy landscapes of RNA/RNA complexes: with applications to snRNA complexes in spliceosomes. *J Mol Biol* **2006**, *357* (1), 292-312. DOI: 10.1016/j.jmb.2005.12.014.

128. Cao, S.; Chen, S. J. Structure and stability of RNA/RNA kissing complex: with application to HIV dimerization initiation signal. *RNA* **2011**, *17* (12), 2130-2143. DOI: 10.1261/rna.026658.111.

129. Zhang, X.; Xu, X.; Yang, Z.; Burcke, A. J.; Gates, K. S.; Chen, S. J.; Gu, L. Q. Mimicking Ribosomal Unfolding of RNA Pseudoknot in a Protein Channel. *Journal of the American Chemical Society* **2015**, *137* (50), 15742-15752. DOI: 10.1021/jacs.5b07910.

130. Zhang, X.; Zhang, D.; Zhao, C.; Tian, K.; Shi, R.; Du, X.; Burcke, A. J.; Wang, J.; Chen, S. J.; Gu, L. Q. Nanopore electric snapshots of an RNA tertiary folding pathway. *Nature communications* **2017**, *8* (1), 1458. DOI: 10.1038/s41467-017-01588-z.

131. Sun, T. T.; Zhao, C.; Chen, S. J. Predicting Cotranscriptional Folding Kinetics For Riboswitch. *J Phys Chem B* **2018**, *122* (30), 7484-7496. DOI: 10.1021/acs.jpcb.8b04249.

132. Zhao, P.; Zhang, W.; Chen, S. J. Cotranscriptional folding kinetics of ribonucleic acid secondary structures. *J Chem Phys* **2011**, *135* (24), 245101. DOI: 10.1063/1.3671644 From NLM Medline.

133. Sun, L. Z.; Jiang, Y.; Zhou, Y.; Chen, S. J. RLDOCK: A New Method for Predicting RNA-Ligand Interactions. *J Chem Theory Comput* **2020**, *16* (11), 7173-7183. DOI: 10.1021/acs.jctc.0c00798.

134. Jiang, Y.; Chen, S. J. RLDOCK method for predicting RNA-small molecule binding modes. *Methods* **2022**, *197*, 97-105. DOI: 10.1016/j.ymeth.2021.01.009.

135. Zhou, Y. Z.; Jiang, Y. W.; Chen, S. J. RNA-ligand molecular docking: Advances and challenges. *Wires Comput Mol Sci* **2021**. DOI: ARTN e1571

10.1002/wcms.1571.

136. Hurst, Travis; Zhou, Yuanzhe; Chen, Shi-Jie. Analytical modeling and deep learning approaches to estimating RNA SHAPE reactivity from 3D structure. *Communications in Information and Systems* **2019**, *19* (3), 299-319. DOI: 10.4310/CIS.2019.v19.n3.a4.

137. Chen, Y.; Pollack, L. SAXS studies of RNA: structures, dynamics, and interactions with partners. *Wiley Interdiscip Rev RNA* **2016**, *7* (4), 512-526. DOI: 10.1002/wrna.1349 From NLM Medline.

138. Oliver, Ryan C.; Rolband, Lewis A.; Hutchinson-Lundy, Alanna M.; Afonin, Kirill A.; Krueger, Joanna K. Small-Angle Scattering as a Structural Probe for Nucleic Acid Nanoparticles (NANPs) in a Dynamic Solution Environment. In *Nanomaterials*, 2019; Vol. 9.

139. Sponer, J.; Bussi, G.; Krepl, M.; Banas, P.; Bottaro, S.; Cunha, R. A.; Gil-Ley, A.; Pinamonti, G.; Poblete, S.; Jurecka, P.; et al. RNA Structural Dynamics As Captured by Molecular Simulations: A Comprehensive Overview. *Chem Rev* **2018**, *118* (8), 4177-4338. DOI: 10.1021/acs.chemrev.7b00427.

140. Rozycki, B.; Kim, Y. C.; Hummer, G. SAXS ensemble refinement of ESCRT-III CHMP3 conformational transitions. *Structure* **2011**, *19* (1), 109-116. DOI: 10.1016/j.str.2010.10.006.

141. Kofinger, J.; Hummer, G. Atomic-resolution structural information from scattering experiments on macromolecules in solution. *Phys Rev E Stat Nonlin Soft Matter Phys* **2013**, *87* (5), 052712. DOI: 10.1103/PhysRevE.87.052712.

142. Chen, P. C.; Hub, J. S. Validating solution ensembles from molecular dynamics simulation by wide-angle X-ray scattering data. *Biophys J* **2014**, *107* (2), 435-447. DOI: 10.1016/j.bpj.2014.06.006.

143. Mlynsky, V.; Bussi, G. Exploring RNA structure and dynamics through enhanced sampling simulations. *Curr Opin Struct Biol* **2018**, *49*, 63-71. DOI: 10.1016/j.sbi.2018.01.004.

144. Bernetti, M.; Hall, K. B.; Bussi, G. Reweighting of molecular simulations with explicit-solvent SAXS restraints elucidates ion-dependent RNA ensembles. *Nucleic Acids Res* **2021**, *49* (14), e84. DOI: 10.1093/nar/gkab459.

145. Welty, R.; Pabit, S. A.; Katz, A. M.; Calvey, G. D.; Pollack, L.; Hall, K. B. Divalent ions tune the kinetics of a bacterial GTPase center rRNA folding transition from secondary to tertiary structure. *RNA* **2018**, *24* (12), 1828-1838. DOI: 10.1261/rna.068361.118.

146. Bussi, Giovanni; Laio, Alessandro. Using metadynamics to explore complex free-energy landscapes. *Nature Reviews Physics* **2020**, *2* (4), 200-212. DOI: 10.1038/s42254-020-0153-0.

147. Paissoni, Cristina; Jussupow, Alexander; Camilloni, Carlo. Martini bead form factors for nucleic acids and their application in the refinement of protein–nucleic acid complexes against SAXS data. *Journal of Applied Crystallography* **2019**, *52* (2), 394-402. DOI: 10.1107/s1600576719002450.

148. Cesari, Andrea; Reißer, Sabine; Bussi, Giovanni. Using the Maximum Entropy Principle to Combine Simulations and Solution Experiments. *Computation* **2018**, *6* (1). DOI: 10.3390/computation6010015.

149. He, Weiwei; Chen, Yen-Lin; Pollack, Lois; Kirmizialtin, Serdal. The structural plasticity of nucleic acid duplexes revealed by WAXS and MD. *Science Advances 7* (17), eabf6106. DOI: 10.1126/sciadv.abf6106 (acccessed 2022/06/07).

150. Wang, Yihang; Lamim Ribeiro, João Marcelo; Tiwary, Pratyush. Machine learning approaches for analyzing and enhancing molecular dynamics simulations. *Current Opinion in Structural Biology* **2020**, *61*, 139-145. DOI: https://doi.org/10.1016/j.sbi.2019.12.016.

151. Šponer, Jiří; Bussi, Giovanni; Krepl, Miroslav; Banáš, Pavel; Bottaro, Sandro; Cunha, Richard A.; Gil-Ley, Alejandro; Pinamonti, Giovanni; Poblete, Simón; Jurečka, Petr; et al. RNA Structural Dynamics As Captured by Molecular Simulations: A Comprehensive Overview. *Chemical Reviews* **2018**, *118* (8), 4177-4338. DOI: 10.1021/acs.chemrev.7b00427.

152. Binzel, D.W.; Khisamutdinov, E.F.; Guo, P. Entropy-driven one-step formation of Phi29 pRNA 3WJ from three RNA fragments. *Biochemistry* **2014**, *53* (14), 2221-2231.

153. Hall, K. B. RNA in motion. *Curr Opin Chem Biol* **2008**, *12* (6), 612-618. DOI: 10.1016/j.cbpa.2008.09.033 From NLM.

154. Hansen, A. L.; Al-Hashimi, H. M. Dynamics of large elongated RNA by NMR carbon relaxation. *Journal of the American Chemical Society* **2007**, *129* (51), 16072-16082. DOI: 10.1021/ja0757982 From NLM.

155. Sun, X.; Zhang, Q.; Al-Hashimi, H. M. Resolving fast and slow motions in the internal loop containing stem-loop 1 of HIV-1 that are modulated by Mg2+ binding: role in the kissing-duplex structural transition. *Nucleic Acids Res* **2007**, *35* (5), 1698-1713. DOI: 10.1093/nar/gkm020 From NLM.

156. Zhang, Q.; Stelzer, A. C.; Fisher, C. K.; Al-Hashimi, H. M. Visualizing spatially correlated dynamics that directs RNA conformational transitions. *Nature* **2007**, *450* (7173), 1263-1267. DOI: 10.1038/nature06389 From NLM.

157. Zhang, Q.; Sun, X.; Watt, E. D.; Al-Hashimi, H. M. Resolving the motional modes that code for RNA adaptation. *Science* **2006**, *311* (5761), 653-656. DOI: 10.1126/science.1119488 From NLM.

158. Ferner, J.; Villa, A.; Duchardt, E.; Widjajakusuma, E.; Wöhnert, J.; Stock, G.; Schwalbe, H. NMR and MD studies of the temperature-dependent dynamics of RNA YNMG-tetraloops. *Nucleic Acids Res* **2008**, *36* (6), 1928-1940. DOI: 10.1093/nar/gkm1183 From NLM.

159. Ilin, S.; Hoskins, A.; Ohlenschläger, O.; Jonker, H. R.; Schwalbe, H.; Wöhnert, J. Domain reorientation and induced fit upon RNA binding: solution structure and dynamics of ribosomal protein L11 from Thermotoga maritima. *Chembiochem* **2005**, *6* (9), 1611-1618. DOI: 10.1002/cbic.200500091 From NLM.

160. Isambert, H. The jerky and knotty dynamics of RNA. *Methods* **2009**, *49* (2), 189-196. DOI: S1046-2023(09)00156-X [pii];10.1016/j.ymeth.2009.06.005 [doi].

161. Al-Hashimi, H.M.; Walter, N.G. RNA dynamics: it is about time. *Curr. Opin. Struct Biol* **2008**, *18* (3), 321-329.

162. Larsen, K. P.; Choi, J.; Prabhakar, A.; Puglisi, E. V.; Puglisi, J. D. Relating Structure and Dynamics in RNA Biology. *Cold Spring Harb Perspect Biol* **2019**, *11* (7). DOI: 10.1101/cshperspect.a032474 From NLM.

163. Chan, Y.; Haverkamp, R. G.; Hill, J. M. Force-extension formula for the worm-like chain model from a variational principle. *J Theor Biol* **2010**, *262* (3), 498-504. DOI: 10.1016/j.jtbi.2009.10.009 From NLM.

164. Li, X.; Bhullar, A. S.; Binzel, D. W.; Guo, P. The dynamic, motile and deformative properties of RNA nanoparticles facilitate the third milestone of drug development. *Adv Drug Deliv Rev* **2022**, *186*, 114316. DOI: 10.1016/j.addr.2022.114316 From NLM.

165. Ding, J.; Swain, M.; Yu, P.; Stagno, J. R.; Wang, Y. X. Conformational flexibility of adenine riboswitch aptamer in apo and bound states using NMR and an X-ray free electron laser. *J Biomol NMR* **2019**, *73* (8-9), 509-518. DOI: 10.1007/s10858-019-00278-w From NLM.

166. Spitale, R. C.; Wedekind, J. E. Exploring ribozyme conformational changes with X-ray crystallography. *Methods* **2009**, *49* (2), 87-100. DOI: 10.1016/j.ymeth.2009.06.003 From NLM.

167. Kim, H.; Abeysirigunawarden, S. C.; Chen, K.; Mayerle, M.; Ragunathan, K.; Luthey-Schulten, Z.; Ha, T.; Woodson, S. A. Protein-guided RNA dynamics during early ribosome assembly. *Nature* **2014**, *506* (7488), 334-338. DOI: 10.1038/nature13039 From NLM.

168. Voith von Voithenberg, L.; Sánchez-Rico, C.; Kang, H. S.; Madl, T.; Zanier, K.; Barth, A.; Warner, L. R.; Sattler, M.; Lamb, D. C. Recognition of the 3' splice site RNA by the U2AF heterodimer involves a dynamic population shift. *Proceedings of the National Academy of Sciences of the United States of America* **2016**, *113* (46), E7169-e7175. DOI: 10.1073/pnas.1605873113 From NLM.

169. Lee, D.; Walsh, J. D.; Yu, P.; Markus, M. A.; Choli-Papadopoulou, T.; Schwieters, C. D.; Krueger, S.; Draper, D. E.; Wang, Y. X. The structure of free L11 and functional dynamics of L11 in free, L11-rRNA(58 nt) binary and L11-rRNA(58 nt)-thiostrepton ternary complexes. *J Mol Biol* **2007**, *367* (4), 1007-1022. DOI: 10.1016/j.jmb.2007.01.013 From NLM.

170. Mitra, K.; Frank, J. Ribosome dynamics: insights from atomic structure modeling into cryo-electron microscopy maps. *Annu Rev Biophys Biomol Struct* **2006**, *35*, 299-317. DOI: 10.1146/annurev.biophys.35.040405.101950 From NLM.

171. Ghimire, C.; Wang, H.; Li, H.; Vieweger, M.; Xu, C.; Guo, P. RNA Nanoparticles as Rubber for Compelling Vessel Extravasation to Enhance Tumor Targeting and for Fast Renal Excretion to Reduce Toxicity. *ACS Nano* **2020**, *14* (10), 13180-13191. DOI: 10.1021/acsnano.0c04863.

172. Li, H.; Zhang, K.; Binzel, D. W.; Shlyakhtenko, L. S.; Lyubchenko, Y. L.; Chiu, W.; Guo, P. RNA nanotechnology to build a dodecahedral genome of single-stranded RNA virus. *RNA Biol* **2021**, *18* (12), 2390-2400. DOI: 10.1080/15476286.2021.1915620.

173. Nazim Uddin, M.; Kim, J. Y. Intercellular and systemic spread of RNA and RNAi in plants. *Wiley Interdiscip Rev RNA* **2013**, *4* (3), 279-293. DOI: 10.1002/wrna.1160 From NLM.

174. Haimovich, G.; Ecker, C. M.; Dunagin, M. C.; Eggan, E.; Raj, A.; Gerst, J. E.; Singer, R. H. Intercellular mRNA trafficking via membrane nanotube-like extensions in mammalian cells. *Proceedings of the National Academy of Sciences of the United States of America* **2017**, *114* (46), E9873-e9882. DOI: 10.1073/pnas.1706365114 From NLM.

175. Melnyk, C. W.; Molnar, A.; Baulcombe, D. C. Intercellular and systemic movement of RNA silencing signals. *Embo j* **2011**, *30* (17), 3553-3563. DOI: 10.1038/emboj.2011.274 From NLM.

176. Homan, P. J.; Favorov, O. V.; Lavender, C. A.; Kursun, O.; Ge, X.; Busan, S.; Dokholyan, N. V.; Weeks, K. M. Single-molecule correlated chemical probing of RNA. *Proceedings of the National Academy of Sciences of the United States of America* **2014**, *111* (38), 13858-13863. DOI: 10.1073/pnas.1407306111 From NLM.

177. Puglisi, J. D.; Wyatt, J. R.; Tinoco, I., Jr. Conformation of an RNA pseudoknot. *J Mol Biol* **1990**, *214* (2), 437-453. DOI: 10.1016/0022-2836(90)90192-o From NLM.

178. Williamson, J. R. Induced fit in RNA-protein recognition. *Nat Struct Biol* **2000**, *7* (10), 834-837. DOI: 10.1038/79575 From NLM.

179. Kudla, G.; Wan, Y.; Helwak, A. RNA Conformation Capture by Proximity Ligation. *Annu Rev Genomics Hum Genet* **2020**, *21*, 81-100. DOI: 10.1146/annurev-genom-120219-073756 From NLM.

180. Andronescu, M.; Condon, A.; Turner, D. H.; Mathews, D. H. The determination of RNA folding nearest neighbor parameters. *Methods Mol Biol* **2014**, *1097*, 45-70. DOI: 10.1007/978-1-62703-709-9_3 From NLM.

181. Robertson, M. P.; Joyce, G. F. The origins of the RNA world. *Cold Spring Harb Perspect Biol* **2012**, *4* (5). DOI: 10.1101/cshperspect.a003608 From NLM.

182. Guo, Peixuan. The emerging field of RNA nanotechnology. *Nature Nanotechnology* **2010**, *5* (12), 833-842. DOI: 10.1038/nnano.2010.231.

183. Ke, Weina; Chandler, Morgan; Cedrone, Edward; Saito, Renata F.; Rangel, Maria Cristina; de Souza Junqueira, Mara; Wang, Jian; Shi, Da; Truong, Nguyen; Richardson, Melina; et al. Locking and Unlocking Thrombin Function Using Immunoquiescent Nucleic Acid Nanoparticles with Regulated Retention In Vivo. *Nano letters* **2022**, *22* (14), 5961-5972. DOI: 10.1021/acs.nanolett.2c02019.

184. Hong, F.; Sulc, P. An emergent understanding of strand displacement in RNA biology. *J Struct Biol* **2019**, *207* (3), 241-249. DOI: 10.1016/j.jsb.2019.06.005 From NLM Medline.

185. Srinivas, N.; Ouldridge, T. E.; Sulc, P.; Schaeffer, J. M.; Yurke, B.; Louis, A. A.; Doye, J. P.; Winfree, E. On the biophysics and kinetics of toehold-mediated DNA strand displacement. *Nucleic Acids Res* **2013**, *41* (22), 10641-10658. DOI: 10.1093/nar/gkt801.

186. Liu, H.; Hong, F.; Smith, F.; Goertz, J.; Ouldridge, T.; Stevens, M. M.; Yan, H.; Sulc, P. Kinetics of RNA and RNA:DNA Hybrid Strand Displacement. *ACS Synth Biol* **2021**, *10* (11), 3066-3073. DOI: 10.1021/acssynbio.1c00336 From NLM Medline.

187. Sulc, P.; Ouldridge, T. E.; Romano, F.; Doye, J. P.; Louis, A. A. Modelling toehold-mediated RNA strand displacement. *Biophys J* **2015**, *108* (5), 1238-1247. DOI: 10.1016/j.bpj.2015.01.023.

188. Panigaj, M.; Dobrovolskaia, M. A.; Afonin, K. A. 2021: an immunotherapy odyssey and the rise of nucleic acid nanotechnology. *Nanomedicine (Lond)* **2021**, *16* (19), 1635-1640. DOI: 10.2217/nnm-2021-0097.

189. Johnson, M. Brittany; Chandler, Morgan; Afonin, Kirill A. Nucleic acid nanoparticles (NANPs) as molecular tools to direct desirable and avoid undesirable immunological effects. *Advanced Drug Delivery Reviews* **2021**, *173*, 427-438. DOI: 10.1016/j.addr.2021.04.011.

190. Saito, R. F.; Rangel, M. C.; Halman, J. R.; Chandler, M.; de Sousa Andrade, L. N.; Odete-Bustos, S.; Furuya, T. K.; Carrasco, A. G. M.; Chaves-Filho, A. B.; Yoshinaga, M. Y.; et al. Simultaneous silencing of lysophosphatidylcholine acyltransferases 1-4 by nucleic acid nanoparticles (NANPs) improves radiation response of melanoma cells. *Nanomedicine* **2021**, *36*, 102418. DOI: 10.1016/j.nano.2021.102418.

191. Afonin, K. A.; Viard, M.; Koyfman, A. Y.; Martins, A. N.; Kasprzak, W. K.; Panigaj, M.; Desai, R.; Santhanam, A.; Grabow, W. W.; Jaeger, L.; et al. Multifunctional RNA nanoparticles. *Nano letters* **2014**, *14* (10), 5662-5671. DOI: 10.1021/nl502385k.

192. Afonin, Kirill A.; Kasprzak, Wojciech K.; Bindewald, Eckart; Kireeva, Maria; Viard, Mathias; Kashlev, Mikhail; Shapiro, Bruce A. In silico design and enzymatic synthesis of functional RNA nanoparticles. *Accounts of chemical research* **2014**, *47* (6), 1731-1741. DOI: 10.1021/ar400329z From PubMed.

193. Hong, E.; Halman, J. R.; Shah, A. B.; Khisamutdinov, E. F.; Dobrovolskaia, M. A.; Afonin, K. A. Structure and Composition Define Immunorecognition of Nucleic Acid Nanoparticles. *Nano letters* **2018**, *18* (7), 4309-4321. DOI: 10.1021/acs.nanolett.8b01283.

194. Avila, Yelixza I.; Chandler, Morgan; Cedrone, Edward; Newton, Hannah S.; Richardson, Melina; Xu, Jie; Clogston, Jeffrey D.; Liptrott, Neill J.; Afonin, Kirill A.; Dobrovolskaia, Marina A. Induction of Cytokines by Nucleic Acid Nanoparticles (NANPs) Depends on the Type of Delivery Carrier. *Molecules* **2021**, *26* (3), 652. DOI: 10.3390/molecules26030652 (acccessed 2021-01-28T18:30:11).

195. Dobrovolskaia, Marina A.; Afonin, Kirill A. Use of human peripheral blood mononuclear cells to define immunological properties of nucleic acid nanoparticles. *Nature protocols* **2020**, *15* (11), 3678-3698. DOI: 10.1038/s41596-020-0393-6 (acccessed 2021-01-28T18:07:44).

196. Johnson, Morgan Brittany; Halman, Justin R; Miller, Daniel K; Cooper, Joseph S; Khisamutdinov, F, Emil; Marriott, Ian; Afonin, Kirill A. The immunorecognition, subcellular compartmentalization, and physicochemical properties of nucleic acid nanoparticles can be controlled by composition modification. *Nucleic Acids Research* **2020**, *48* (20), 11785-11798. DOI: 10.1093/nar/gkaa908 (acccessed 2021-01-28T18:04:55).

197. Ke, W.; Hong, E.; Saito, R. F.; Rangel, M. C.; Wang, J.; Viard, M.; Richardson, M.; Khisamutdinov, E. F.; Panigaj, M.; Dokholyan, N. V.; et al. RNA-DNA fibers and polygons with controlled immunorecognition activate RNAi, FRET and transcriptional regulation of NF-kappaB in human cells. *Nucleic Acids Res* **2019**, *47* (3), 1350-1361. DOI: 10.1093/nar/gky1215.

198. Rackley, L.; Stewart, J. M.; Salotti, J.; Krokhotin, A.; Shah, A.; Halman, J. R.; Juneja, R.; Smollett, J.; Lee, L.; Roark, K.; et al. RNA Fibers as Optimized Nanoscaffolds for siRNA Coordination and Reduced Immunological Recognition. *Adv Funct Mater* **2018**, *28* (48). DOI: 10.1002/adfm.201805959.

199. Halman, J. R.; Satterwhite, E.; Roark, B.; Chandler, M.; Viard, M.; Ivanina, A.; Bindewald, E.; Kasprzak, W. K.; Panigaj, M.; Bui, M. N.; et al. Functionally-interdependent shape-switching nanoparticles with controllable properties. *Nucleic Acids Res* **2017**, *45* (4), 2210-2220. DOI: 10.1093/nar/gkx008 From NLM.

200. Johnson, M. B.; Halman, J. R.; Satterwhite, E.; Zakharov, A. V.; Bui, M. N.; Benkato, K.; Goldsworthy, V.; Kim, T.; Hong, E.; Dobrovolskaia, M. A.; et al. Programmable Nucleic Acid Based Polygons with Controlled Neuroimmunomodulatory Properties for Predictive QSAR Modeling. *Small (Weinheim an der Bergstrasse, Germany)* **2017**, *13* (42). DOI: 10.1002/smll.201701255 From NLM.

201. Chandler, Morgan; Rolband, Lewis; Johnson, M. Brittany; Shi, Da; Avila, Yelixza I.; Cedrone, Edward; Beasock, Damian; Danai, Leyla; Stassenko, Elizabeth; Krueger, Joanna K.; et al. Expanding Structural Space for Immunomodulatory Nucleic Acid Nanoparticles via Spatial Arrangement of Their Therapeutic Moieties. *Advanced Functional Materials* **2022**, *32* (43), 2205581, https://doi.org/10.1002/adfm.202205581. DOI: https://doi.org/10.1002/adfm.202205581 (acccessed 2022/10/25).

202. Zhovmer, Alexander S.; Chandler, Morgan; Manning, Alexis; Afonin, Kirill A.; Tabdanov, Erdem D. Programmable DNA-augmented hydrogels for controlled activation of human lymphocytes. *Nanomedicine: Nanotechnology, Biology and Medicine* **2021**, *37*, 102442. DOI: https://doi.org/10.1016/j.nano.2021.102442.

203. Chandler, Morgan; Minevich, Brian; Roark, Brandon; Viard, Mathias; Johnson, M. Brittany; Rizvi, Mehedi H.; Deaton, Thomas A.; Kozlov, Seraphim; Panigaj, Martin; Tracy, Joseph B.; et al. Controlled Organization of Inorganic Materials Using Biological Molecules for Activating Therapeutic Functionalities. *ACS applied materials & interfaces* **2021**, *13* (33), 39030-39041. DOI: 10.1021/acsami.1c09230.

204. Hong, E.; Halman, J. R.; Shah, A.; Cedrone, E.; Truong, N.; Afonin, K. A.; Dobrovolskaia, M. A. Toll-Like Receptor-Mediated Recognition of Nucleic Acid Nanoparticles (NANPs) in Human Primary Blood Cells. *Molecules* **2019**, *24* (6). DOI: 10.3390/molecules24061094.

3 CHAPTER 3: BREAK TO BUILD – ISOTHERMAL ASSEMBLY OF NUCLEIC ACID NANOPARTICLES (NANPs) VIA ENZYMATIC DEGRADATION

3.1 Introduction

The intrinsic properties of RNA and DNA biopolymers emphasized by engineered nucleic acid nanoparticles (NANPs) offer accelerated development of next-generation therapies. The rational design of NANPs brings about reproducible architectures intended for regulated molecular and cellular interactions. The conventional bottom-up assembly of NANPs relies on the thermal annealing of individual strands. Here, we introduce a concept of nuclease-driven production of NANPs where selective digestion of functionally inert structures leads to isothermal self-assembly of liberated constituents. The working principles, morphological changes, and assembly kinetics as well as the retention of structural integrity for system components, subjected to anhydrous processing and storage, are assessed. Furthermore, the experiments with immune reporter cells show that the developed protocol retains the functionality of tested NANPs. This approach enables exploiting the advantages of various conditionally produced NANPs and that NANPs' stability, immunorecognition, and assembly can be regulated to allow for a more robust functional system.

Self-assembly is a ubiquitous natural process where molecules spontaneously organize themselves in higher-order structures based on non-covalent interactions [1]. This phenomenon encompasses a broad spectrum of assembly examples involving many types of molecular structures, including nucleic acids, proteins, and lipids making their self-assembled structures indispensable for life [2]. Many assemblies, such as the cytoskeleton, are in a continual dynamic process of regulated assembly and disassembly. Although the molecular

rearrangement of this system is spontaneous, cells maintain substantial control over molecular associations [3]. The working principles of these active structures have already inspired the development of responsive, shape-switching protein and nucleic acid-based nanosystems [4, 5].

The self-assembling nucleic acid nanoparticles (NANPs) are an advanced class of biomaterials comprised of programmable combinations of structural and functional RNA and DNA motifs embedded within the same unique architectures. Assembled NANPs often gain new physicochemical properties that can be quite distinct from their original constituents but still retain the functional roles of nucleic acids [6]. Significantly, the immunomodulatory properties of NANPs also differ from the unassembled monomers and can be rationally designed to illicit expected immune responses [7-9].

The bottom-up assembly of NANPs is typically a multistep process that requires the combination of individually synthesized and characterized constituent strands subjected to different assembly protocols characteristic to individual NANPs' design principles and composition [10]. The correctly assembled 3D structures play a prominent role in NANPs not only by spatially organizing multiple functional moieties but also by dictating the immunomodulatory responses to different NANPs [11, 12]. While widely used, the high level of technicality of the existing assembly protocols and the lack of control over the conditional formation of NANPs at isothermal conditions preclude broader biomedical applications of NANPs.

We report a novel method for NANP self-assembly that relies on a single incubation step involving the substrate-specific nucleases to selectively digest the intended constituents of the precursor structures. Cleaving only the selected strands within the inert structures releases

complementary sequences that adopt the next most thermodynamically stable conformation corresponding to a particular NANP. Notably, cleavage and self-assembly occur simultaneously and under the same conditions at 37°C.

3.2 Nuclease Driven Assembly

This approach represents a crucial step forward since 37°C is the normal temperature of the human body and a benchmark temperature for all therapeutics. In our opinion, this proof of concept study will originate a new branch of nucleic acid nanotechnology where different enzymes can govern the selective degradation of delivered material to initiate the assembly of expected functional NANPs within the cells.

The standard bottom-up approach for NANPs construction relies on one-pot annealing of purified single-stranded monomers under specific thermal conditions that differ for various NANPs (Figure 1a). Our approach examined a new method that depends on the selective digestion of precursor hybrid DNA/RNA material. Upon addition of RQ1 DNase or RNase H, corresponding nucleic acids are degraded, and remaining intact RNA or DNA strands are free to re-assemble into the intended cubic structure. This new method for the formation of DNA or RNA cubes circumvents multiple incubation steps and allows both assemblies to occur in a single step by an isothermal incubation at a physiological temperature of 37°C (Figure 1a). This could provide an advantage for the upscaled production of NANPs. Furthermore, this approach allows the production of NANPs without any advanced lab equipment or complex protocols.

The addition of RQ1 DNase to hybrid RNA/DNA duplexes leads to the assembly of RNA cubes since subsequent treatment of RNA cubes with RNase ONE degrades all RNA assemblies, as shown by native-PAGE experiments (Figure 1b). Similarly, RNase H releases

DNA monomers from hybrid duplexes that create DNA cubes that can then be degraded by RQ1 DNase (Figure 1b). If we conjugate individual RNA and DNA cube monomers with Alexa488 or Alexa546, respectively, we can observe the shift in gel migration and color change after individual strands bind to their complementary counterparts (Figure 1b). After applying relevant enzymes, corresponding strands are degraded, and DNA or RNA cubes are formed (Figure 1b).

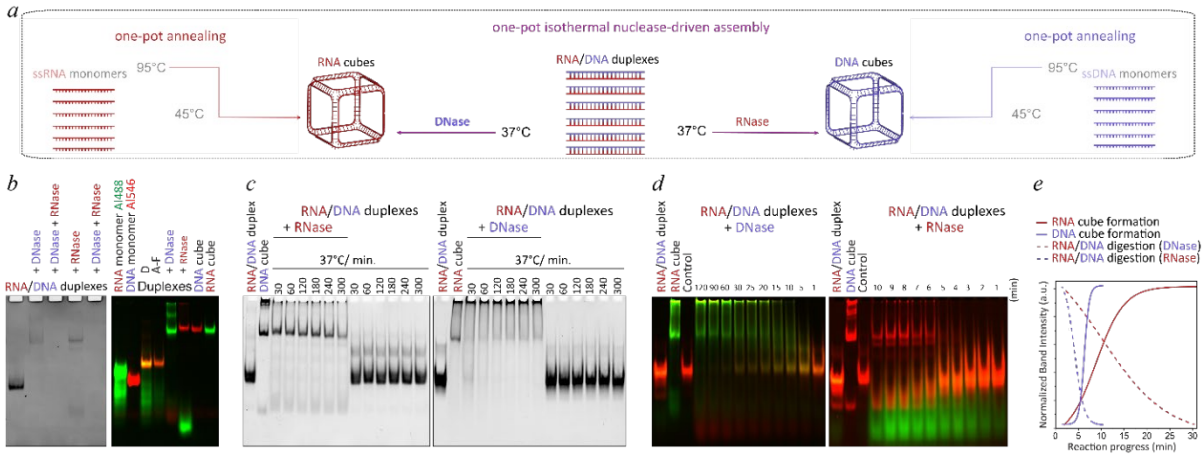

Figure 1: Dynamics of nuclease-driven DNA or RNA cube assembly. (a) The schematic idea of the proposed assembly of nucleic acid nanoparticles via enzymatic degradation by the "break to build" approach. (b) Confirmation of cube origin by nuclease treatment after ethidium bromide staining (left) and by fluorescent labeling (right). (c) Time course-dependent DNA and RNA cube nuclease-driven assembly. Duplexes were treated with nucleases at 37°C for up to 5 hours. In highlighted time points, assemblies were moved to 4°C until 5 hours. (d) Short-term assembly dynamics of fluorescently labeled RNA or DNA strands. (e) Kinetics are calculated based on assemblies depicted in figure (d).

3.3 Kinetics of Degradation and Assembly

Depending on the composition of intact strands, DNA or RNA cubes are assembled at different rates at physiological temperatures. Traditional assembly of NANPs was used as a standard for comparison to nuclease-driven assembly reactions. In both cases, cubes created by nuclease-driven assembly have the same molecular weight as cubes formed by the traditional bottom-up method. The first DNA cubes are formed within 30 minutes after

RNase addition, as seen by non-denaturing polyacrylamide gel electrophoresis (Figure 1c). Interestingly, prolonged incubation of up to 5 hours does not lead to higher yields; however, after 5 hours, the yield of DNA cubes was lower. Extended storage of DNA cubes at 4°C seems to ensure higher yield. We have not observed any changes during similar conditions of intact RNA/DNA duplexes without nucleases. It should also be noted that DNA cubes show less aggregation remaining in the loading well compared to cubes prepared by the traditional assembly protocol. This could be attributed to the slow equimolar release of cube monomers while incubated near the melting point of the cube consisting of DNA only.

Observation of assembly dynamics less than 35 minutes showed that RNase-driven assembly of DNA cube starts forming as soon as after 5 minutes, and all monomers are assembled in 10 minutes (SI Figure S1). Interestingly, the second band is visible in nuclease-driven assembly but not in control DNA cubes. The likely explanation is that the two bands appear as an artifact arising from snap freezing in liquid nitrogen that caused cold-denaturation leading to destabilization of the DNA cube structure.

Assembly of RNA cubes requires a significantly longer time; after 30 minutes, we can still observe monomer hybrid blocks, and RNA cubes only appeared after 1 hour (Figure 1c). Compared with the control assembly, the proportion of RNA material trapped in wells is higher.

Further analysis of nuclease-driven assembly kinetics shows that DNase RQ1 is significantly slower in the degradation of DNA monomers (~ 30 minutes) and thus releasing ssRNA strands, while RNase H degrades its RNA substrate in DNA-RNA hybrids much faster (~ 10 minutes) (Figure 1d-e). Although DNA monomers are degraded after 15 minutes, we observe the first RNA assemblies not sooner than after 60 minutes. We speculate that the incubation

temperature below the melting temperature of the RNA cube may allow secondary structures. These unwanted interactions take additional time to overcome during RNA cube assembly. The presence of partially cleaved DNA strands that are still hybridized to their RNA counterparts may be another hindrance that may reduce the speed of RNA cube assembly.

3.4 Structural Characterization

Finally, we confirmed the homogeneity of structure and the morphology of RNA/DNA duplexes and RNA or DNA cubes by atomic force microscopy (AFM) (Figure 2). The short linear strands of the duplexes were no longer present, indicating that the nucleic acid was restructured after the nuclease digestion.

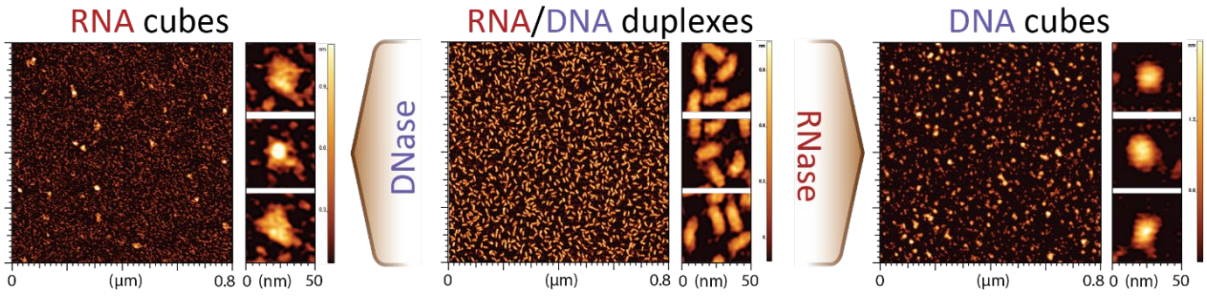

Figure 2: AFM images of RNA and DNA cubes assembled upon selective nuclease cleavage of RNA/DNA hybrid duplexes.

3.5 NANP Storage Stability

Currently, the standard storage and transportation of NANPs require a cold chain that is costly and, under some circumstances, challenging. Previously we found out that diverse NANPs react differently to various dehydration methods and subsequent storage conditions [13]. SpeedVac is one of the simplest available laboratory techniques with the most promise for future upscaling and cost-effectiveness when addressing storage possibilities outside the cold chain. However, from examined dehydration techniques (lyophilization and Light-assisted drying), SpeedVac has the most negative impact on the structure and recovery of cubes (DNA

and RNA) or rings (RNA), no matter the storage conditions. While DNA cubes were restored to some extent, RNA cubes and rings were completely lost.

The advantage of the presented “break to build” approach is that from one simple structure, we create two different NANPs. Duplexes are highly stable when dried by any dehydration method. Therefore, we investigated how the SpeedVac dehydration method affects nuclease-driven reassembly (SI Figure S2a). Possible harsh conditions during shipping and storage outside of the cold chain were simulated by storage of dried duplexes at 50°C for 25 hours. As expected, duplexes resisted elevated temperature either dried or in solution as determined by native-PAGE. Similar resistance was observed for DNA cubes. DNA cubes created by RNase H-driven assembly, regardless of the duplex storage, assembled efficiently to the expected structure even without the presence of any trapped complexes in the wells (SI Figure 2b). Unlike DNA cubes, dried RNA cubes by SpeedVac have not been recovered after rehydration. However, assembled DNA cubes stored at 50°C for 25 hours in solution maintained their structure. Remarkably, duplexes stored at 50°C in a dry or soluble state were re-assembled to RNA cubes after DNase treatment (SI Figure S2b).

3.6 Cube Reassociation from a Single Duplex

Next, we hypothesized that accommodating all six monomers into one long duplex might improve the stoichiometry of individual cube components, thus enhancing equimolar assembly. To test this hypothesis, we designed six holding DNA strands that were complementary to RNA monomers as well as a 15-mer overhang complementary to adjacent holding DNA strands. The addition of RQ1 DNase should lead first to the degradation of dsDNA toeholds that connect all six hybrid duplexes. In the follow-up step, DNase should degrade DNA in duplexes (Figure 3a). Assembly of DNA holding strands with RNA cube

components should create 396 bp long fibers, as confirmed by agarose electrophoresis (Figure 4b). Our assumption of step-wise degradation of long fiber was confirmed by time course treatment of fibers with DNase and native PAGE analysis. DNase first degrades the long fiber structure into hybrid duplexes and then, in a slower fashion, degrades DNA in RNA/DNA hybrid duplexes. The RNA cubes are visible after one hour, corresponding with previous results (Figure 4c). The nuclease-driven transition of long fibers to RNA cubes was finally confirmed by AFM (Figure 3d).

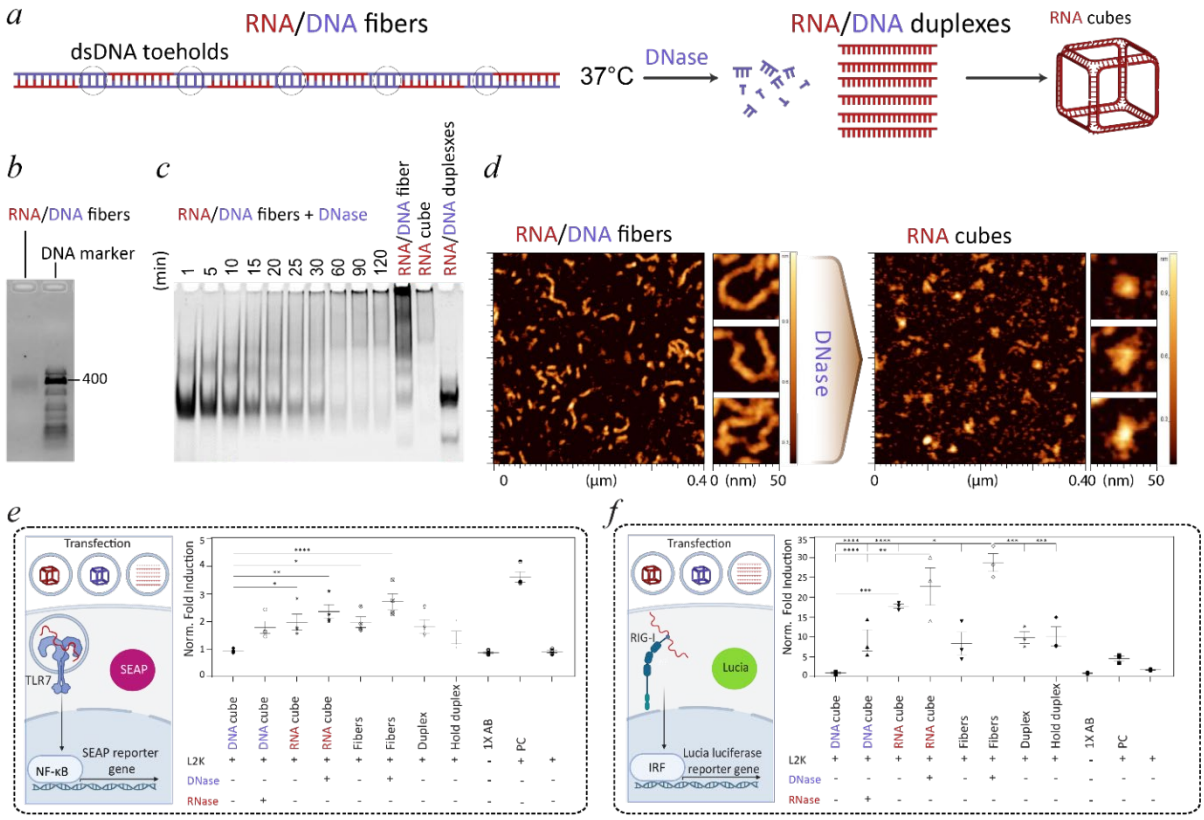

Figure 3: DNase-driven assembly of RNA cubes from long fibers and immunostimulation of RIG-I and TLR7 in reporter HEK-Lucia RIG-I or HEK-Blue hTLR7 reporter cell lines by transfected cubes, fibers, and duplexes. (a) Schematics of long fiber composed from hybrid RNA/DNA duplexes interconnected through DNA toehold interactions. The proposed degradation mechanism assumes two-step DNA cleavage- first, dsDNA toeholds are degraded, followed by hybrid duplexes. (b) Confirmation of RNA/DNA fiber assembly. (c) Gradual stepwise fiber degradation by DNase and assembly of RNA cubes over time. (d) AFM

confirmation of fibers and resulting RNA cubes. (e) Scheme of RIG-I activation with subsequent expression of Lucia luciferase that is secreted to cell media and normalized fold induction of RIG-I by individual treatments. n= 3, ± SEM. Statistical analysis by ordinary one-way ANOVA. (f) Scheme of TLR7 activation with subsequent expression and secretion of SEAP to cell media. Normalized fold induction of TLR7 by individual treatments. n= 4, ± SEM. Statistical analysis by ordinary one-way ANOVA.

3.7 Effect of Enzyme Treatment on Immunorecognition

Functionalized and scaffolded DNA and RNA cube nanostructures have been tested to induce selected pattern recognition receptors. We examined the immunostimulatory properties of our assemblies in reporter cell lines that express TLR7 or RIG-I. The TLR7 is endosomal receptor sensing ssRNAs, while RIG-I is a cytosolic receptor recognizing RNA with triphosphate on the 5' end of RNA. Naturally, the outcome of signaling pathways triggered through both receptors is Interferon type I production. Stimulation of TLR7 or RIG-I in engineered cell lines activates expression and secretion of SEAP (secreted embryonic alkaline phosphatase) or Luciferase, respectively (Figure 3e and 3f). None of our constructs activated TLR7 signaling higher than a positive control R848, suggesting that no or minimal free RNA monomers were present in our nucleic acid-carrier complexes (3f), though all RNA-containing structures, except A to F and hold duplexes, activated TLR7 significantly higher than DNA cubes. The cell viability in HEK-Blue hTLR7 cells treated with our constructs, except duplexes A to F and Hold-duplexes, was substantially lower compared to cells incubated with positive control or transfection reagent (SI Figure S3a). A more interesting situation was observed in HEK-Lucia RIG-I reporter cells. Transfected DNA cubes prepared from pure DNA strands or RNase H-driven DNA cubes have not elicited RIG-I stimulation compared to hybrid RNA/DNA duplexes (Figure 3f). Both RNA cube assemblies, control, and DNase-driven, stimulated RIG-I similarly and significantly higher than DNA cubes and corresponding duplexes or positive control 3php-RNA. Interestingly,

the most stimulatory RNA assembly arose from degraded long fibers. Except for DNase-driven RNA cubes, the level of secreted Luciferase upon transfection of DNase-driven RNA cubes from long fibers was significantly higher than any compared cube assembly or control sample (Figure 3f). The viability of HEK-Lucia RIG-I cells was similar for all transfected cells without any significant difference from cells incubated with control reagents (SI Figure S3b).

3.8 Computational Analysis

We employed molecular dynamics (MD) simulations to investigate the stability and dynamics of RNA structures at two different temperatures, 37°C and 45°C. Our findings (Figure 4a and 4b) indicate that the root-mean-square deviation (RMSD) and root-mean-square fluctuation (RMSF) values of the RNA cube structure at 45°C were higher than those at 37°C, suggesting that the thermostability of the cube structure was reduced at the higher temperature. To further explore the effects of digested DNA on RNA structures, we conducted simulations for RNA-only and RNA with digested DNA structures—the RNA-only configuration comprised 6 RNA chains arranged at random. In contrast, the RNA-DNA hybrid structure encompassed multiple 5-mer DNA fragments that were complementary to the residues present in the 6 RNA chains. The RMSD and RMSF analyses (Figures 4c and 4d) revealed that the interaction between the RNA chains and digested DNA led to an elevation in the thermostability of the RNA chains, hindering their ability to form the cube structure due to base pairing interactions between RNA and DNA residues. Finally, we performed simulations for DNase with dsDNA and DNase with RNA/DNA complexes. The RMSD and RMSF analyses (Figures 4e and 4f) revealed that the RNA/DNA complex was more stable than dsDNA upon binding the DNase. In addition, the radius of gyration of

dsDNA (Figure 4h) was observed to be greater than that of the RNA/DNA complex. This observation suggests that the DNase exerted a more pronounced stretching effect (Figure 4g) on the double-stranded DNA, which may have increased the likelihood of the DNase cleavage site encountering the DNA chains. Conversely, the RNA chains in the RNA/DNA complex imparted a higher degree of rigidity compared to dsDNA. Notably, we computed the distances between the active site of the DNase (H134) and the DNA chains and observed that the distances in the DNase/dsDNA complex were significantly shorter than those in the RNA/DNA complex (Figure 4i). This finding elucidates the mechanism underlying the faster rate of DNase-mediated cleavage of dsDNA compared to the RNA/DNA complex.

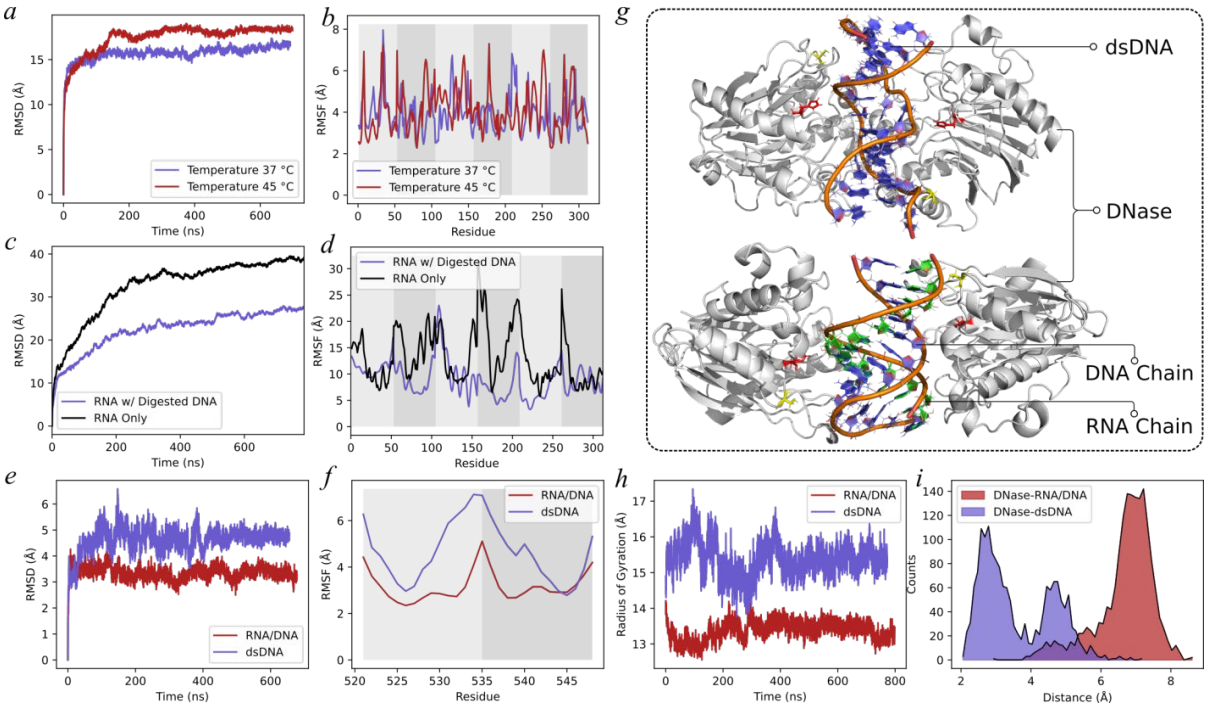

Figure 4: The molecular dynamics simulation results. (a) and (b) are the root-mean-square deviation (RMSD) and root-mean-square fluctuation (RMSF) analyses of the RNA cube structure under 37°C and 45°C. (c) and (d) are RMSD and RMSF analyses of the RNA-only structure and the RNA with digested DNA structure. The striped shading of the background in (b) and (d) indicates different RNA chains. (e) and (f) are the RMSD and RMSF analyses of the DNase/RNA/DNA complex and the DNase/dsDNA complex. The striped shading of the background in (f) indicates different RNA and DNA chains. (g) is the centroid structure of the

largest cluster from the simulation of the DNase/RNA/DNA complex and the DNase/dsDNA complex. (h) is the radius of gyration analysis of the two complexes. (i) is the distribution of the distances between the active site (H134) in the DNase and the DNA chains.

3.9 Conclusions

In summary, we described a new one-step protocol for the assembly of cube nanoparticles with distinct immunostimulatory profiles. Formation of DNA or RNA cubes requires only physiological temperature and the addition of substrate-specific nucleases. Together with the temperature stability of source material, our approach allows storage and assembly independent of cold chain and complex laboratory equipment. The further development of the “break to build” method besides the streamlining of NANPs assembly may result in the design of particles that will assemble intracellularly by using cellular enzyme machinery.

3.10 References

1. Whitesides, G. M.; Mathias, J. P.; Seto, C. T. Molecular self-assembly and nanochemistry: a chemical strategy for the synthesis of nanostructures. *Science* **1991**, *254* (5036), 1312-1319. DOI: 10.1126/science.1962191.

2. Mendes, A. C.; Baran, E. T.; Reis, R. L.; Azevedo, H. S. Self-assembly in nature: using the principles of nature to create complex nanobiomaterials. *Wiley Interdiscip Rev Nanomed Nanobiotechnol* **2013**, *5* (6), 582-612. DOI: 10.1002/wnan.1238.

3. Fletcher, D. A.; Mullins, R. D. Cell mechanics and the cytoskeleton. *Nature* **2010**, *463* (7280), 485-492. DOI: 10.1038/nature08908.

4. Agarwal, S.; Franco, E. Enzyme-Driven Assembly and Disassembly of Hybrid DNA-RNA Nanotubes. *Journal of the American Chemical Society* **2019**, *141* (19), 7831-7841. DOI: 10.1021/jacs.9b01550.

5. Zhan, P.; Jahnke, K.; Liu, N.; Gopfrich, K. Functional DNA-based cytoskeletons for synthetic cells. *Nat Chem* **2022**, *14* (8), 958-963. DOI: 10.1038/s41557-022-00945-w.

6. Shu, Y.; Haque, F.; Shu, D.; Li, W.; Zhu, Z.; Kotb, M.; Lyubchenko, Y.; Guo, P. Fabrication of 14 different RNA nanoparticles for specific tumor targeting without accumulation in normal organs. *RNA (New York, N.Y.)* **2013**, *19* (6), 767-777. DOI: 10.1261/rna.037002.112.

7. Johnson, M. Brittany; Chandler, Morgan; Afonin, Kirill A. Nucleic acid nanoparticles (NANPs) as molecular tools to direct desirable and avoid undesirable immunological effects. *Advanced Drug Delivery Reviews* **2021**, *173*, 427-438. DOI: 10.1016/j.addr.2021.04.011.

8. Chandler, Morgan; Johnson, Morgan Brittany; Panigaj, Martin; Afonin, Kirill A. Innate immune responses triggered by nucleic acids inspire the design of immunomodulatory nucleic acid nanoparticles (NANPs). *Current Opinion in Biotechnology* **2020**, *63*, 8-15. DOI: 10.1016/j.copbio.2019.10.011 (acccessed 2021-02-02T12:23:47).

9. Afonin, Kirill A.; Dobrovolskaia, Marina A.; Church, George; Bathe, Mark. Opportunities, Barriers, and a Strategy for Overcoming Translational Challenges to Therapeutic Nucleic Acid Nanotechnology. *ACS Nano* **2020**, *14* (8), 9221-9227. DOI: 10.1021/acsnano.0c04753 (acccessed 2021-01-04T20:59:11).

10. Afonin, K. A.; Grabow, W. W.; Walker, F. M.; Bindewald, E.; Dobrovolskaia, M. A.; Shapiro, B. A.; Jaeger, L. Design and self-assembly of siRNA-functionalized RNA nanoparticles for use in automated nanomedicine. *Nature protocols* **2011**, *6* (12), 2022-2034. DOI: 10.1038/nprot.2011.418.

11. Afonin, K. A.; Viard, M.; Koyfman, A. Y.; Martins, A. N.; Kasprzak, W. K.; Panigaj, M.; Desai, R.; Santhanam, A.; Grabow, W. W.; Jaeger, L.; et al. Multifunctional RNA nanoparticles. *Nano letters* **2014**, *14* (10), 5662-5671. DOI: 10.1021/nl502385k.

12. Hong, E.; Halman, J. R.; Shah, A. B.; Khisamutdinov, E. F.; Dobrovolskaia, M. A.; Afonin, K. A. Structure and Composition Define Immunorecognition of Nucleic Acid Nanoparticles. *Nano letters* **2018**, *18* (7), 4309-4321. DOI: 10.1021/acs.nanolett.8b01283.

13. Tran, Allison N.; Chandler, Morgan; Halman, Justin; Beasock, Damian; Fessler, Adam; McKeough, Riley Q.; Lam, Phuong Anh; Furr, Daniel P.; Wang, Jian; Cedrone, Edward; et al. Anhydrous Nucleic Acid Nanoparticles for Storage and Handling at Broad Range of Temperatures. *Small (Weinheim an der Bergstrasse, Germany)* **2022**, *n/a* (n/a), 2104814, https://doi.org/10.1002/smll.202104814. DOI: https://doi.org/10.1002/smll.202104814 (acccessed 2022/03/11).

3.11 Appendix A: Supporting Information for Break to build: isothermal assembly of nucleic acid nanoparticles (NANPs) via enzymatic degradation

Sequences used in this project:

RNA cube:

rA- 5'- GGCAACUUUGAUCCCUCGGUUUAGCGCCGGCCUUUUCUCCCACACUUUCACG

rB- 5'- GGGAAAUUUCGUGGUAGGUUUUGUUGCCCGUGUUUCUACGAUUACUUUGGUC

rC- 5'- GGACAUUUUCGAGACAGCAUUUUUUCCCGACCUUUGCGGAUUGUAUUUUAGG

rD- 5'- GGCGCUUUUGACCUUCUGCUUUAUGUCCCCUAUUUCUUAAUGACUUUUGGCC

rE- 5'- GGGAGAUUUAGUCAUUAAGUUUUACAAUCCGCUUUGUAAUCGUAGUUUGUGU

rF- 5'- GGGAUCUUUACCUACCACGUUUUGCUGUCUCGUUUGCAGAAGGUCUUUCCGA

rD-Al488-

5'- GGCGCUUUUGACCUUCUGCUUUAUGUCCCCUAUUUCUUAAUGACUUUUGGCC/Al488/

DNA cubes with three As at each corner (all starnds are complementary to corresponding cube strands):

anti-dA- 5'- CGTGAAAGTGTGGGAGAAAAGGCCGGCGCTAAACCGAGGGATCAAAGTTGCC

anti-dB- 5'- GACCAAAGTAATCGTAGAAACACGGGCAACAAAACCTACCACGAAATTTCCC

anti-dC- 5'- CCTAAAATACAATCCGCAAAGGTCGGGAAAAAATGCTGTCTCGAAAATGTCC

anti-dD- 5'- GGCCAAAAGTCATTAAGAAATAGGGGACATAAAGCAGAAGGTCAAAAGCGCC

anti-dE- 5’-
ACACAAACTACGATTACAAAGCGGATTGTAAAACTTAATGACTAAATCTCCC

anti-dF- 5’- TCGGAAAGACCTTCTGCAAACGAGACAGCAAAACGTGGTAGGTAAAGATCCC

anti-dDAl546:

5’- /Al546/GGCCAAAAGTCATTAAGAAATAGGGGACATAAAGCAGAAGGTCAAAAGCGCC

DNA strands equired to form RNA/DNA fibers when mixed with RNA cube strands

For the RNA/DNA fibers, the 15mer overlaps have been color-coded to reflect their intended interactions.

Holding A
5'TAGGCACCTTGCTAACGTGAAAGTGTGGGAGAAAAGGCCGGCGCTAAACCGAGGGATCAAA
GTTGCC

a’

Holding B
5'TTAGCAAGGTGCCTAGACCAAAGTAATCGTAGAAACACGGGCAACAAAACCTACCACGAAA
TTTCCCGTATACGACGCGCTA

b’

Holding C
5'CTACGGTCATATTGCCCTAAAATACAATCCGCAAAGGTCGGGAAAAAATGCTGTCTCGAAA
ATGTCCTAGCGCGTCGTATAC

c’

Holding D
5'GCAATATGACCGTAGGGCCAAAAGTCATTAAGAAATAGGGGACATAAAGCAGAAGGTCAAA
AGCGCCGTCACTGATGTCAGA

d'

Holding E
5'ACGACTGTCAGGTCAACACAAACTACGATTACAAAGCGGATTGTAAAACTTAATGACTAAA
TCTCCCTCTGACATCAGTGAC

e'

Holding F
5'TGACCTGACAGTCGTTCGGAAAGACCTTCTGCAAACGAGACAGCAAAACGTGGTAGGTAAA
GATCCC

Supporting Figures:

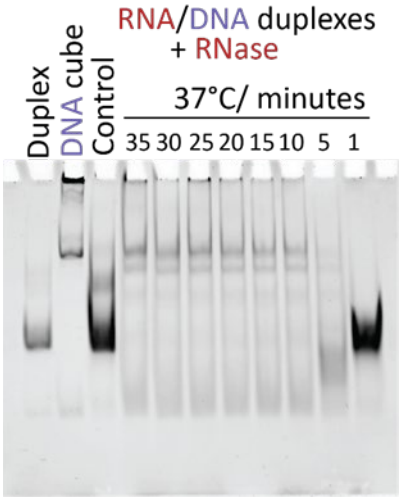

Supporting Figure S1: Kinetics of DNA cube RNase-driven assembly.

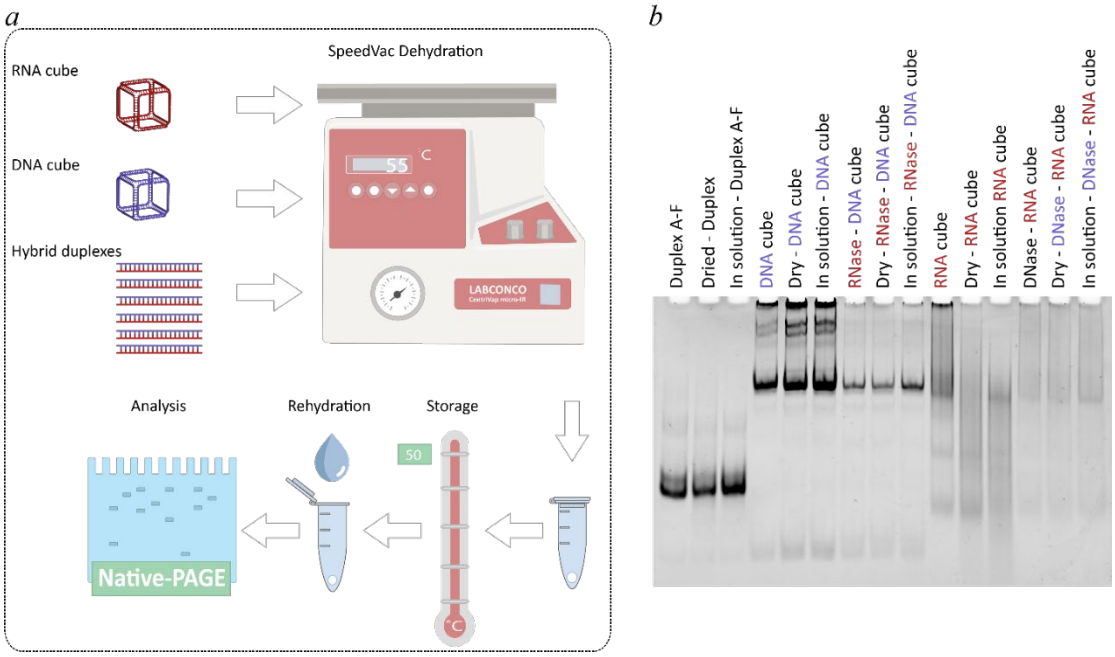

Supporting Figure S2: Effect of storage on duplex and cube assembly's stability. (a) Scheme of simulation test for RNA, DNA cubes or duplexes storage under elevated temperature. (b) Native PAGE analysis of DNA, RNA cubes, and duplexes stability after storage at 50°C in soluble or dehydrated state.

a

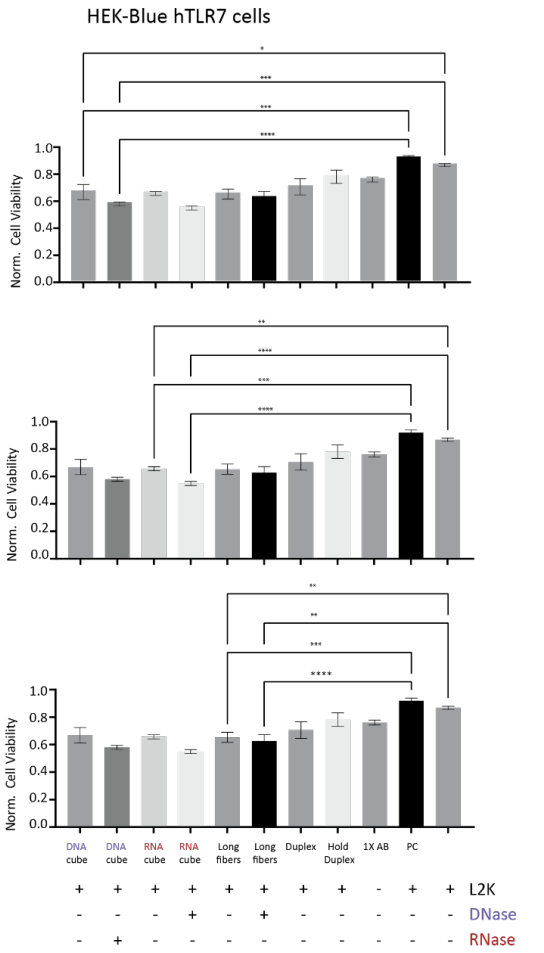

b

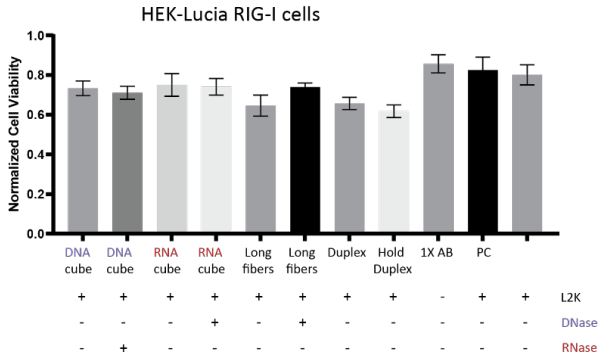

Supporting Figure S3: Cell viability of reporter HEK-Blue hTLR7 and HEK-Lucia RIG-I reporter cell line by transfected cubes, fibers, and duplexes. (a) Normalized cell viability in treated HEK-Blue hTLR7 cell line. n= 4, ±SEM. (b) HEK-Lucia RIG-I viability, n= 3, ±SEM.

Material and methods

NANP Synthesis.All template DNA and primers for PCRs and DNA cube monomers were purchased from IDT. PCR was used to amplify transcription templates using MyTaq Mix (Bioline). PCR product was then purified by DNA Clean and Concentrator kit (Zymo Research). RNA cube monomers were transcribed by in vitro run-off transcription with T7 RNA polymerase in 80 mm HEPES-KOH (pH 7.5), 2.5 mm spermidine, 50 mM DTT, 25 mm MgCl2, and 25 mM of each rNTP at 37 °C for 3.5hr. RQ1 RNase-free DNase (Promega) was used to degrade DNA templates before RNA purification by 8 M urea PAGE 8%AA (29:1). Excised bands were cut and overnight eluted in crush and soak buffer (300 mm NaCl, 89 mm tris-borate [pH = 8.2], 2 mm EDTA). Eluted RNA in crush and soak buffer was mixed with 100% EtOH in 1:1.5 ratio and placed in -20 °C for at least 4 hours. Mixture was centrifuged at 14,000 rcf for 30 min. Pellets were rinsed three times with 90% ethanol. Samples were finally dried by SpeedVac at 55°C and RNA pellets were resuspended in endotoxin free water. Absorbances were checked using a NanoDrop 2000. NANPs were assembled in equimolar ratio of each monomer. DNA or RNA monomers were denatured at 95 °C for 2 min after that assembly buffer (89 mm tris-borate [pH 8.2], 2 mm MgCl2, 50 mm KCl) was added, and solution was incubated at 45°C for 30 min. Similarly, duplexes were treated but incubation in assembly buffer was at room temperature for 20 mins. Long fibers were assembled by first assembling duplexes of each RNA cube monomer and the complementary DNA holding strand. All separate duplexes were then added in an equimolar ratio to a single solution and allowed to assemble at 37°C. Assemblies were confirmed on an 8% (37.5:1) non-denaturing (native-PAGE) polyacrylamide gel with running buffer

containing 89 mm tris-borate (pH 8.2) and 2 mm MgCl2. The gels were run in a Mini-PROTEAN electrophoretic apparatus at 200V for 40 minutes and stained with ethidium bromide for 5 min.

AFM. AFM was carried out on a freshly cleaved mica surface submerged in an aqueous solution of APS (10(3-aminopropyl)-silatrane). AFM imaging was performed with a MultiMode AFM Nanoscope IV system (Bruker Instruments) in tapping mode. Images were processed by FemtoScan Online software package (Advanced Technologies Center, Moscow, Russia).

Nuclease treatment. The 3 μL of RQ1 DNase or RNase H were used to treat 60 μL of mixed duplex A-F solution at 1 μM. Samples were incubated at 37°C for the duration of the experiment. For control solutions, 3 μL of H2O was added instead of nuclease. 2 μL aliquots were taken from the reaction tube at specific time points and added to labeled PCR tubes. Time point aliquots were stored at 4°C to inhibit nuclease activity.

Kinetics. Quantification of band intensities was performed using ImageLab software version 6.0.1. Lanes and bands were manually defined. Kinetics were graphed using OriginPro 2023 and sigmoidal fit was performed using a Boltzmann function.

Stability experiments. An IR Vacuum Concentrator (Labconco) was used to dry all structures at 55°C and with IR radiation until no liquid remained. Sample tubes were placed on a heat block at 50°C for the reported length of experiment. Samples were resuspended back to the original volumes using endotoxin free water.

Reporter cell assays. HEK-Blue hTLR7 and HEK-Lucia RIG-I cells were all purchased from InvivoGen and maintained according to the supplier's guidelines in an incubator at 37°C and

5% CO2. Cells were plated at 10,000 cells per well in a 96-well plate 24 h prior to transfection. All NANPs were complexed with Lipofectamine 2000 (to ensure 0.375 μL per well) at room temperature for 30 minutes before adding to cells. Positive controls were 10 ng mL of 3p-hpRNA for HEK-Lucia RIG-I and 2 μg mL of R848 for HEK-Blue hTLR7 cells. Immunostimulation was visualized by QUANTI-Blue for HEK-Blue cell line or QUANTI-Luc for HEK-Lucia RIG-I cell line. For the QUANTI-Blue assay 180 μL of the reagent was added with 20 μL of cell supernatant in a 96-well plate and incubated for 3 h at 37°C. The plate was read on a Tecan Spark plate reader at an absorbance of 638 nm. All well values were the averages of 16-point reads. For the QUANTI-Luc assay, 50 μL of the reagent was added with 20 μL of cell supernatant in a black-walled 96-well plate. The plate was read immediately on a Tecan Spark plate reader for luminescence with a 100 ms reading time.

Computational simulations. The MD simulations were conducted using the pmemd.cuda program within the Amber 18 software package. We utilized the Amber RNA OL3 force field and protein ff14sb force field, which has been previously demonstrated to yield satisfactory results when studying the stability and dynamics of RNAs. The starting structures of RNA-only and RNA with digested DNAs were generated using iFoldRNA program [1-3]. The structure of DNase I - DNA complex (PDB ID: 2DNJ) was used as a template to build the initial structure of DNase/dsDNA and the DNase/RNA/DNA complex. All the structures were prepared using the teLeap module in Amber 18. The molecules were solvated in an octahedral box containing TIP3P water molecules, with a distance of 9Å maintained between atoms and the box boundary. We added potassium ions to neutralize the system, followed by additional K^+ and Cl^- ions to achieve a concentration of approximately 0.3 M. We conducted several energy minimization steps before the actual simulation. Firstly, we employed the

steepest descent method for 1000 steps followed by 1000 steps using the conjugate gradient method to perform energy minimization of the entire system. During the MD simulation phase, we initially applied weak restraints to the molecules and allowed the system to heat up from 0 K to the designated temperatore (37 °C or 45 °C) over 200 ps. Afterward, we removed the restraints on the RNA molecules and performed explicit solvent MD under constant pressure using the isothermal-isobaric (NPT) ensemble, with a time step of 2 fs. The length of hydrogen bonds was constrained using the shake algorithm, while the temperature was maintained, and pressure was kept constant at 1 bar throughout the simulation.

4 CHAPTER 4: DNA-TEMPLATED FLUORESCENT SILVER NANOCLUSTER INHIBIT BACTERIAL GROWTH WHILE BEING NON-TOXIC TO MAMMALIAN CELLS

4.1 Introduction

Silver has a long history of antibacterial effectiveness. The combination of atomically precise metal nanoclusters with the field of nucleic acid nanotechnology has given rise to DNA-templated silver nanoclusters (DNA-AgNCs) which can be engineered with reproducible and unique fluorescent properties and antibacterial activity. Furthermore, cytosine-rich single-stranded DNA oligonucleotides designed to fold into hairpin structures improve the stability of AgNCs and additionally modulate their antibacterial properties and the quality of observed fluorescent signals. In this work, we characterize sequence-specific fluorescence of four representative DNA-AgNCs, com-pare their corresponding antibacterial effectiveness at different pH, and assess cytotoxicity to several mammalian cell lines.

The formation of silver nanoclusters (AgNC) on single-stranded (ss) DNA templates has been shown to promote the unique optical properties defined by the sequences of the DNA strands.[1-3] Out of all available coordination sites on nucleobases, silver cations demonstrate the highest affinity for the N3 of cytosines,[4] and therefore cytosine-rich ssDNAs become efficient capping-agents for AgNC formation. The size and shape of AgNCs are regulated by rationally designed DNAs with different numbers of single-stranded cytosines embedded in secondary and tertiary DNA structures such as hairpin loops, i-motifs, and G-quadruplexes, to name a few.[3, 4] The optical properties of DNA-AgNCs are dictated by their size, as the appearance of the characteristic fluorescence is possible for nanoclusters comprised of only a few silver atoms. At this nanometer size, a continuous density of

electronic energy states present in bulk silver breaks up and a band gap in the material becomes apparent.[1-6] This, in turn, causes a molecule-like behavior of AgNCs with discrete energy states allowing for size-dependent fluorescence to occur.[5-7] DNA-capped AgNCs are also generally more resistant to photobleaching when compared to traditional organic fluorophores or fluorescent proteins, and this property begets the application of DNA-AgNCs in a variety of nanophotonics and biosensing/biomedical applications.[8-11] While nanophotonic and biosensing with DNA-AgNCs' advantageous optical properties have been widely probed and studied, other practical uses of AgNCs remain unexplored. Since the main functional component of DNA-AgNCs is silver, applications based on effects known for this element may prove useful. Various forms of silver, including ions and silver nanoparticles, are well-documented to have antibacterial efficacy.[12-15] Several groups have shown DNA-AgNCs to be effective against both Gram-negative and Gram-positive bacteria in liquid cultures[16-18] and against the formation of biofilms when aptamers for increased targeting and binding of the bacteria of interest were introduced.[19, 20] However, the underlying mechanisms and relationship between the fluorescent properties of AgNCs and their antibacterial actions are still understudied and poorly understood. AgNCs offer a large surface-to-volume ratio and are composed of both forms of silver: cationic (Ag^{+}) and neutral (Ag^{0}), thereby providing further advantages over solid silver, silver salts, or silver nanoparticles.

We reason that understanding and linking optical and antibacterial properties of DNA-AgNCs may pave the way to the development of next generation antibacterial agents with high potency and regulated activity. Our current work includes four representative DNA hairpins that template the formation of DNA-AgNCs with four distinct colors and investigates their optical properties in relation to antibacterial activity measured at different

pH, as well as in relation to cytotoxicity assessed for several human cell lines. The use of antibacterial DNA-AgNCs formed on DNA hairpins becomes advantageous for various antibacterial formulations and opens broader possibilities for DNA nanotechnology due to the relative structural stability of the hairpins and their inability to participate in any undesirable base-pairings, thus not interfering with any other DNA nanodesigns. As proof-of-concept work, we explore the use of DNA-AgNC forming hairpins with odd numbers of consecutive cytosines (C7, C9, C11, or C13) in their loop compositions.

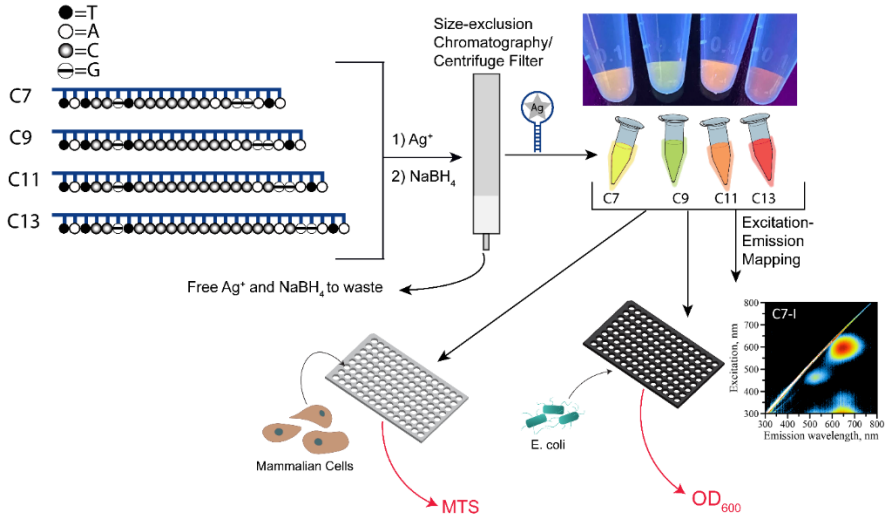

Figure 1. Experimental flow of DNA-AgNC synthesis, purification, and analysis. The embedded image shows DNA-AgNCs after their purification upon UV excitation on a transilluminator.

4.2 Results

4.2.1 Template design

Cytosine-rich ssDNAs are suitable capping agents for templating stable DNA-AgNCs due to cytosine's high affinity for silver ions, Ag^{+}. Various sequences have been reported to stabilize clusters with unique optical properties, including bright emission bands in the visible part of the spectrum and excitation bands in the UV and visible regions. The emission wavelengths can be modulated by choosing a specific DNA sequence and various colors (e.g., blue, green,

red as shown in Figure 1) of DNA-AgNCs have been reported based on prevalent emission wavelengths for a particular nanocluster. While the parameters that define emissive properties of DNA-AgNCs are still not well understood, it is generally accepted that shape, size, and overall charge state of the AgNC are among the main contributors. We hypothesize that the same factors are responsible for modulating the antibacterial activity of the DNA-AgNCs. While cytosine-rich ssDNAs have been widely used in synthesizing AgNCs, these sequences are prone to forming alternative DNA structures.[21] Such alternative structures include i-motif and non-canonical C-Ag-C base paring facilitated by the presence of silver cations. We have compared properties of two C12-containing templates in which one is an opened ssDNA and another is a sequence embedded in a hairpin loop. The results (Supporting Figure S1) clearly show the differences observed for these two sequences after DNA-AgNC formation. As evident from AFM images (Supporting Figure S1A-B), the single-stranded template shows various degrees of polymerization, while the hairpin-loop template does not polymerize, forming isolated DNA-AgNCs. These results agree well with our recent study demonstrating that the formation of alternative DNA structures in the presence of Ag+ drives the polymerization of various sequences containing single stranded C-rich stretches.[21] Additionally, such polymerization also alters fluorescence properties of AgNCs (Supporting Figure S1C-D). Hairpin-looped structures feature one single fluorescence peak while single-stranded templates shows multiple peaks, suggesting the formation of AgNC with various sizes and shapes due to variety in the polymerized templates.[21] To avoid structural and functional uncertainties associated with ss-C_N template sequences and to make the structures suitable for further implementation in nanodesign, we have chosen to work only with DNA hairpin templates wherein the C_N sequence forms the

loop of the hairpin structure. Four representative templates were constructed with the same double-stranded stem and a loop with a variable number of cytosines (C7, C9, C11, and C13). This design gradually increases the number of binding sites for silver and makes the size of the loop larger (Figure 1).[3, 22] An odd number of cytosines in the loop with +2C steps was intended to noticeably alter properties of the DNA-AgNCs with fluorescent colors covering the entire visible spectral region (Figure 1). We reasoned that such substantial optical differences would provide an insight into which factors modulate the antibacterial activity of the DNA-AgNCs and how antibacterial activity correlates with the optical signatures of individual DNA-AgNCs. Incubation of the looped DNA templates with silver nitrate and subsequent reduction of silver using sodium borohydride results in the formation of optically active nanoclusters with bright emission (Figures 1and 2).

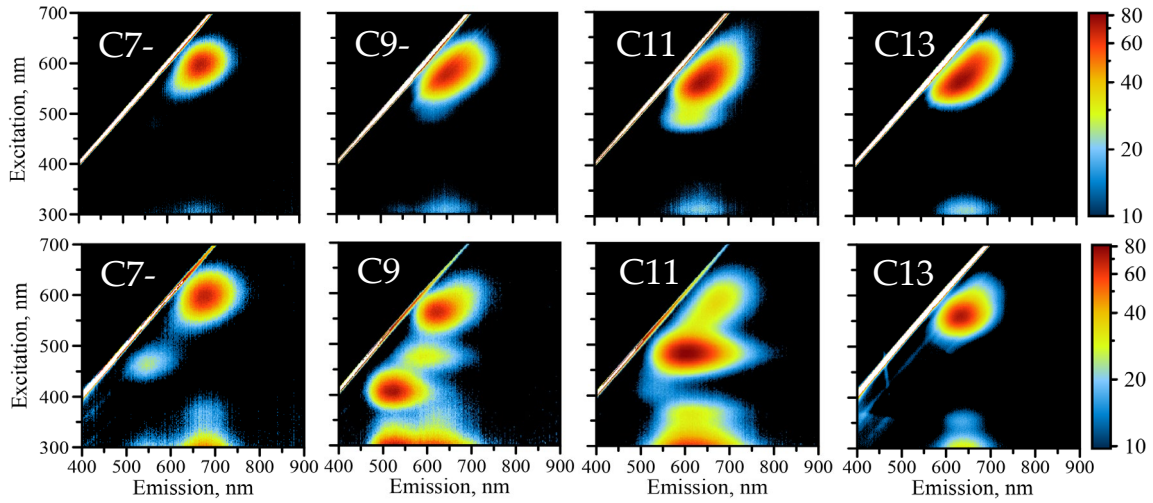

Figure 2. Fluorescence measurements of DNA-AgNCs. Excitation-Emission Matrix Spectroscopy: top panel shows the initial readings of freshly made DNA-AgNCs, bottom panel corresponds to the analysis of samples aged over a period of two weeks (dual fluorescence pattern with both green and red peaks is typical for freshly prepared AgNCs producing distinct colors shown in Figure 1).

4.2.2 Fluorescence

The formation of DNA-AgNCs is tracked by the changes in solution that are observed within a few hours after the addition of silver nitrate and sodium borohydride reducing agent and incubation in the dark. We have characterized the optical properties of these DNA-AgNCs using fluorescence excitation-emission matrix spectroscopy (EEM). EEM represents the excitation/emission relationships of the optical response of the DNA-AgNCs presented as 2D contour maps.[23] Figure 2 shows EEM maps for all four DNA-AgNCs in the 300-800 nm range for the excitation while recording the emission spectrum spanning 300-800 nm wavelengths. Initial reading of the EEMs after purification (top panel of Figure 2) indicates that all four samples show a great degree of similarity in the behavior of emission. All four samples are dominated by one peak in the red part of the spectrum. While similar in general, the peaks show detectable differences.

In Table 1, we summarize peak positions for the maximum of excitation and maximum of emission for all four DNA-AgNCs. It appears that smaller loop DNA-AgNCs have maxima for both excitation and emission shifted to higher wavelengths. It is very pronounced for C7 and C9 with $\lambda_{EXC}/\lambda_{EM}$=600/685 nm and $\lambda_{EXC}/\lambda_{EM}$=580/661 nm, respectively. Further shift to $\lambda_{EXC}/\lambda_{EM}$=562/647 nm and $\lambda_{EXC}/\lambda_{EM}$=562/645 nm is observed for C11 and C13, respectively. C11 DNA-AgNC also features an extra shoulder of emission at lower excitation wavelengths. C9, C11, and C13 peaks appear to be elongated featuring red edge emission shift (REES) as reported previously and as is common for AgNCs.[21, 24, 25] Interestingly, C7 DNA-AgNC does not have REES-based elongation of the emission peak which is well-pronounced for other samples. These observations emphasize the differences of

DNA-AgNCs formed by the four looped templates despite all samples having "red" emission.

Table 1. Spectral position of excitation and emission for "red" emitting peak in initial EEMs.

Wavelength, nm	C7	C9	C11	C13
EXC_{MAX}	600	580	562	562
FLU_{MAX}	685	661	647	645

The differences in observed optical properties intensify further as samples are allowed to age. Changes in emission pattern with time develop quickly and represent conversion of AgNCs upon interaction with ambient conditions. We have previously reported that aging of DNA-AgNCs leads to the conversion of "red" to "green" emission.[24] Such changes can be linked to the interactions of AgNCs with species dissolved in the solution that are capable of oxidizing silver atoms ($Ag^0 \rightarrow Ag^+$), such as molecular oxygen.[24] Many reports documented the "blue" shift with aging and some protocols call for bubbling oxygen through to stimulate this transition.[26] All four of our samples also experience such "blue" shift and eventually develop a pattern of multi-peaked emission with some samples more noticeable that others, for example C9 vs C13. Figure 2 summarizes in detail all changes in emission patterns when C7-C13 DNA-AgNCs age over a period of two weeks. The appearance of additional emission peaks in the "green" region are obvious for C7, C9, and C11, while C13 remained primarily as a single peak. The changes in C13 DNA-AgNCs include the loss of elongated shape with the near-IR part of the peak disappearing over time. Shorter loops C7, C9, and C11 develop an obvious multipeak excitation-emission pattern over time. These new peaks appear in the "orange" and "green" spectral region. Also, these peaks differ significantly in their position and intensity. C7 DNA-AgNCs have only one new peak of $\lambda_{EXC}/\lambda_{EM}$=465/547 nm – "green". The intensity of this new peak is 27% the intensity

of the original “red” peak. Both C9 and C11 have multi-peak patterns of newly appeared “orange” and “green” emission labeled O (longer wavelengths) and G (shorter wavelengths). The positions of these two new peaks are very similar for both C9 and C11 DNA-AgNCs: $\lambda_{EXC}/\lambda_{EM}$=475/606 nm (O-C9), $\lambda_{EXC}/\lambda_{EM}$=480/606 nm (O-C11), $\lambda_{EXC}/\lambda_{EM}$=408/530 nm (G-C9), and $\lambda_{EXC}/\lambda_{EM}$=410/536 nm (G-C11). Similar spectral positions indicate the same nature of “green” states for both C9 and C11 DNA-AgNCs. The differences for these two samples, however, include the position of the “red” peak as listed in Table 1. Another major difference is the relative intensities of green peaks, both O and G. O peak dominates in the C11 sample, while G is more pronounced in the C9 sample. The following are the relative intensities as compared to the original “red” peak: 22% (O-C9), 360% (O-C11), 112% (G-C9), and 29% (G-C11). The observed intensities suggest that C9 DNA-AgNCs primarily stabilize G state while C11 DNA-AgNCs prefer O. O peak is not observed in the fluorescence of the aged C7 sample, while C13 remains “red” during aging.

To complete the description of emissive properties of C7-C13 templated AgNCs, we also visualized the emission of nanoclusters under UV excitation on a trans-illuminator (at 254 nm). Such excitation is typically discussed as a means of excitation via DNA bases that contact silver atoms in the nanocluster. 254 nm excitation results in a color palette of the employed samples (colors under trans-illuminator excitation, Figure 1- top). This picture reflects the rich emission pattern observed for C7-C13 samples in the visible part of the spectrum.

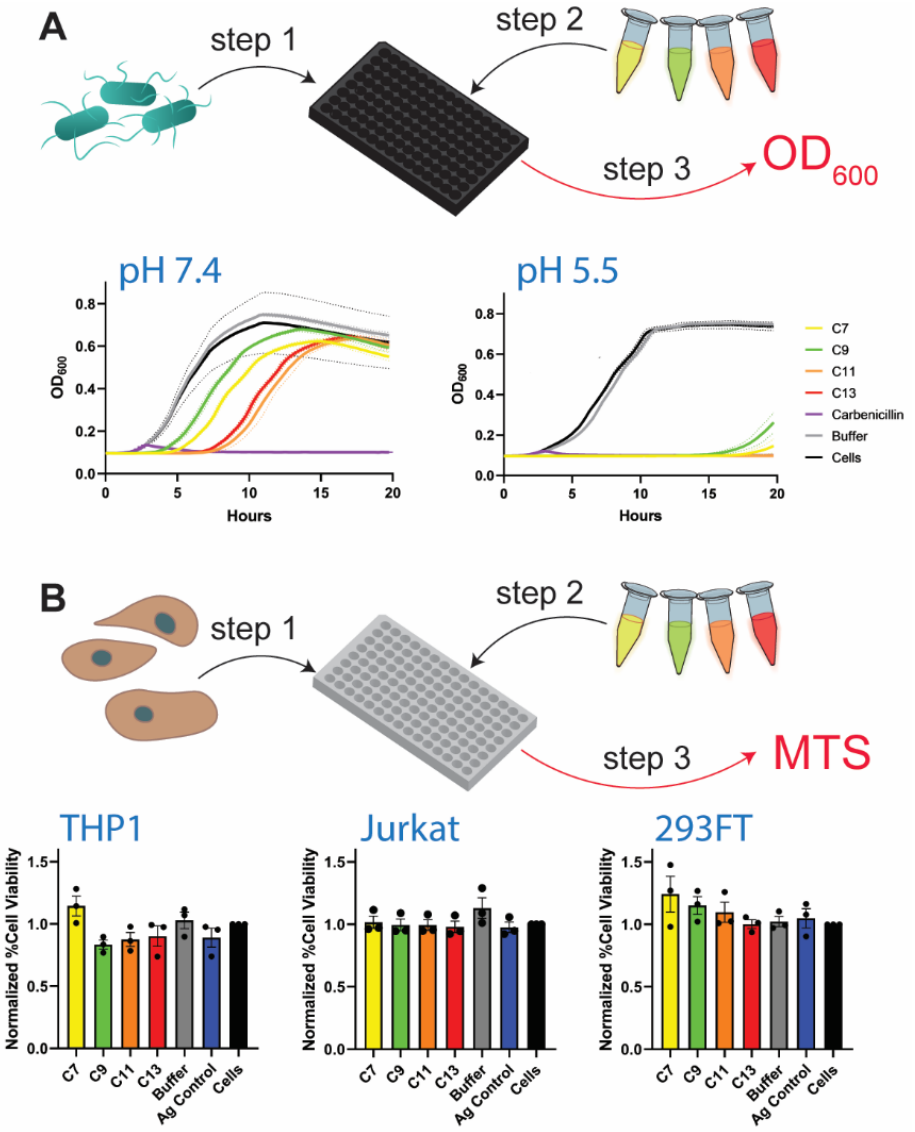

Figure 3. Biological activity of AgNCs. (A) The growth curves of E. coli when treated with 4 µM DNA-AgNC are shown at pH 7.4 (the pH of standard LB) and pH 5.5. The standard deviation of each measurement is shown as a dotted line on both sides of the solid line in the same color. The lines for C11, C13, and Carbenicillin overlap at pH 5.5. (B) The normalized cell viability of THP1-DualTM, Jurkat, and 293FT cells after incubation with 4 µM AgNC for 20 hours, as assessed by an MTS assay.

4.2.3 Cell Culture

To assess the relative effects of representative DNA-AgNCs on bacterial cells, TOP10F' *E. coli* were grown in liquid cultures and were treated with the panel of DNA-AgNCs at a final concentration of 4 µM (Figure 3A). A decrease in the bacterial growth was

observed over a 20-hour period for all *E. coli* cultures treated with AgNCs when compared to the non-treated control. There was a strong dose dependence noted for all AgNCs (Supporting Figure S3) with 4 μM showing moderate effectiveness for all of them. As such, all further experiments were carried out at 4 μM in order to best resolve differences between individual clusters. In order to quantitatively examine the inhibition of *E. coli* growth, we compared the change in the amount of time required for bacteria cultured with each AgNC to grow to half of their maximum optical density ($\Delta t_{1/2}$). As compared to bacteria alone, C11 was the most effective with a $\Delta t_{1/2}$ of 6.3 ± 0.4 hours. The other AgNCs showed a lesser extent of inhibition with $\Delta t_{1/2}$ values of 3.5 ± 0.5 hours, 1.5 ± 0.3 hours, and 5.6 ± 0.4 hours for C7, C9, and C13 respectively. The effect of free-silver ions or nanoparticles at the concentrations used to synthesize the AgNCs can be considered minimal since the control experiment with 650 μM of Ag^+, the highest of the concentrations used for C_N synthesis, was found to have a minimal effect on the growth curve after being reduced with $NaBH_4$ (Supporting Figure S4). The antibacterial effect of the AgNCs greatly increased with a drop in pH. When *E. coli* grown in pH 5.5 buffered LB were treated with 4 μM of each DNA-AgNC, the growth was nearly fully inhibited over the entire 20 hours (Figure 3A). From all of these experiments, an interesting pattern appears that C7 outperforms C9 and C11 outperforms C13 in bacterial growth inhibition. It is clear from these data that the number of cytosines in the loop does not directly play a role in the antibacterial effectiveness of a particular DNA-AgNC complex.

In order to test these same conditions in mammalian cells, several human cell lines were used. All AgNCs were again introduced at a 4 μM final concentration and the cell viability was assessed after 20 hours of incubation using an MTS assay. No statistically

significant reduction in cell viability was found after incubation with AgNCs for Jurkat, THP1, or 293FT cells (Figure 3B). In order to ensure the AgNCs were relatively safe for mammalian cells, these experiments were repeated at a final concentration of 8 µM AgNC with all three cell lines. Again, no statistically significant decrease in cell viability was found at the higher AgNC concentration (Supporting Figure S5). Therefore, AgNCs remain harmless to mammalian cells at concentrations required to inhibit bacterial growth.

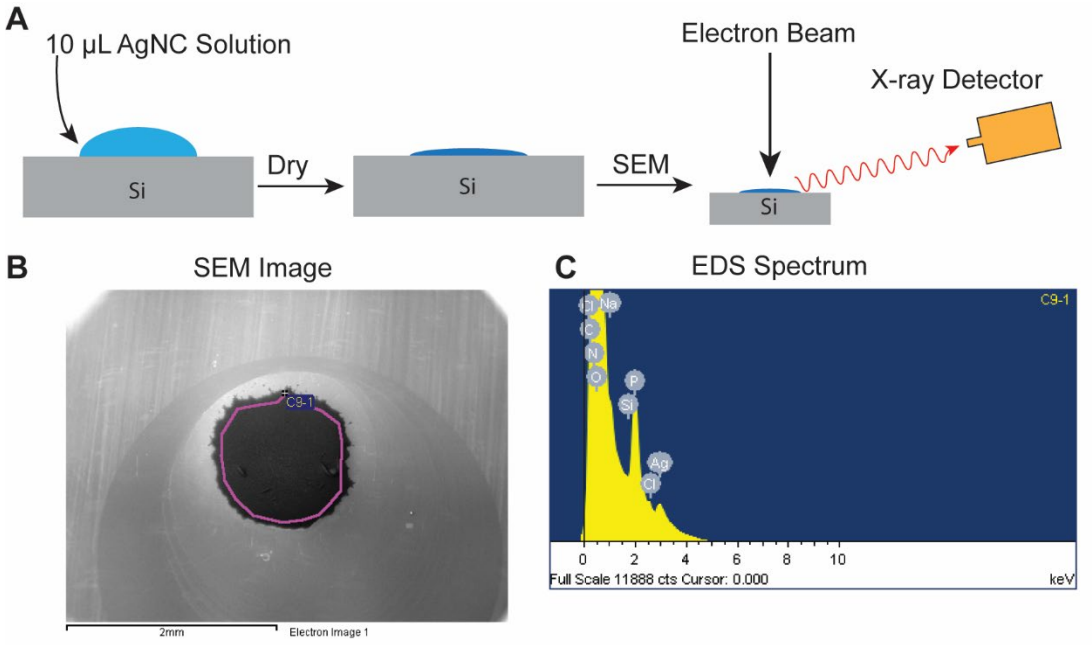

Figure 4. (A) The general workflow for the SEM and EDS experiments is shown. The drying step took place at ambient conditions with the silicon wafer covered by a petri dish. (B) A representative SEM image is shown of an AgNC C9 sample and the (C) raw EDS spectrum of the same sample. The purple ring defines the outer perimeter of the area that was scanned to obtain the EDS spectrum.

4.2.4 Stoichiometry determination

In order to quantify the number of silver atoms bound to each ssDNA oligonucleotide, EDS was performed and micrographs of dried AgNC solutions were recorded using SEM. The ratio of the relative atomic percentages of the Ag and P in the EDS spectrum were used for evaluating stoichiometric ratio of silver per hairpin-loop DNA

template. DNA-AgNCs with the highest (C11) and the lowest (C9) antibacterial activity were examined. From these experiments, we determined that C9 DNA-AgNC binds an average of 8.5 ± 0.5 silver atoms while C11 DNA-AgNC binds an average of 11.7 ± 0.5 silver atoms. Representative micrographs are shown in Figure 4 and the supplementary information (Supporting Figure S6).

4.3 Discussion

Silver has long been used as a disinfectant. The most recent applications include the use of silver nanoparticles in many different areas including food packaging, water and air disinfection, the textile sector, and medical applications (Silver Soaker® Catheters, Acticoat™, SilvaSorb® Gel).[27, 28] The search for new therapeutic agents to combat multi-drug resistant (MDR) bacteria is ongoing. While silver nanoparticles have been recently extensively studied for their use as antibacterial agents,[29] novel silver nanoclusters have been largely overlooked[16] primarily because most studies have focused on biosensing applications due to the unique optical properties of AgNCs.[25, 30, 31] DNA-AgNCs have several advantages which position them as excellent candidates for antibacterial applications. First, DNA-AgNCs are small in size – they are comprised of only a few atoms of silver capped with stabilizing cytosine-rich ssDNA oligonucleotides. Since DNA-AgNCs are bound to DNA, in addition to serving as a host for AgNCs, DNA can also be utilized for embedding AgNCs into a structured network of functional assemblies leading to novel properties and functions of hybrid nanomaterials.[21, 24] In this study, we show that AgNCs are capable of inhibiting bacterial growth at a much lower concentration (4 μM) than carbenicillin (132 μM), which is a bactericidal antibiotic from the penicillin group and was used as a positive control in this study. Additionally, we confirm that DNA-AgNCs show very little toxicity against human

cells and that the DNA templates contribute to the solubility and biocompatibility of DNA-AgNCs, which is one of the biggest advantages of nanoclusters. Thus, DNA-AgNCs could potentially be used against a broad range of various bacteria without harmful side effects. Furthermore, robust fluorescence of AgNCs can be coupled with biocompatibility and antibacterial properties to produce label-free bioimaging agents with dual purpose. Our additional experiments indicate that DNA-AgNCs exhibit antibacterial activity against *Lactobacilli* (Supporting Figure S2), suggesting that AgNCs might cause undesirable effects to the gut microbiota, and should be avoided in applications involving oral ingestion of these materials, *e.g.* in food packaging.

Our results show that C11 and C13 DNA-AgNCs produce the highest antibacterial activity among all four studied sequences, while C7 and C9 DNA-AgNCs show lower activity (Figure 3A). It is of note that the smaller of each of these pairs is the highest performer. While there are several factors that might contribute to antibacterial activity, the number of cytosines in the templating sequence does not appear to be the decisive factor. Since the amount of silver was matched in our experiments with the number of cytosines in the loop, which was confirmed by EDS analysis to match a 1:1 ratio of Ag:C, it is also unlikely that the amount of silver in the cluster determines the antibacterial properties of AgNCs. Our conclusion is supported by a previous report which also ruled out the number of cytosines in a sequence and the amount of silver atoms per cluster.[16] Emission color has been proposed to correlate with DNA-AgNCs' antibacterial properties with "red" emissive clusters being the most active.[16] We also turned to fluorescence properties in search of a possible explanation for the antibacterial activity of DNA-AgNCs. It is unclear how exactly silver nanoclusters act in terms of antibacterial properties and this uncertainty in the mechanism of

antibacterial action for DNA-AgNCs has triggered the current study. There are clear changes in fluorescent properties of DNA-AgNCs which we can correlate with the increased antibacterial activity of AgNCs. It appears that a multi-peak emission pattern might be the key. The mere presence of "red" fluorescence does not define antibacterial properties; all samples are "red" initially, but the abilities to inhibit bacterial growth differ among C11, C13 and C9, C7. C13 remains "red" during aging while C11 effectively converts to "orange." At the same time, C11 provides better antibacterial efficacy as compared to C13. Also, C7 remains primarily "red" while its activity is lower than C11 and C13. C9 is the only sample that develops a "green" peak with high intensity, but it is also less effective at inhibiting bacterial growth.

It is commonly accepted that DNA-AgNCs include both Ag^0 and Ag^+ atoms in their composition. The ratio of Ag^0/Ag^+ defines the overall charge state and the color of the nanocluster's emission.[32] It has been proposed that distinct "green" and "red" fluorescence occurs for a "magic number" of neutral silver atoms in the nanocluster.[32, 33] Four neutral atoms produce green fluorescence and six neutral Ag atoms produce red fluorescence regardless of the number of Ag^+.[32] Recent studies indicated that such conversion does not change the overall number of silver, *N*, in the cluster as this conversion is reversible.[24, 29] "Red," "orange," and "green" emissive states of AgNCs we observe may represent different ratios of Ag^+ to Ag^0. Aging of the samples can therefore be explained by the interaction of AgNCs with species dissolved in the solution that are capable of oxidizing silver atoms ($Ag^0 \rightarrow Ag^+$). For example, dissolved "molecular oxygen" might effectively convert "red" to "orange" and to "green" emitting species. Controlled oxidation with hydrogen peroxide confirms our conclusion (Supporting Figure 7). The addition of hydrogen peroxide gradually

converts emissive patterns which resembles “aging” of all samples. Many studies relate the antibacterial activity of silver nanoparticles to oxidative release of Ag^{+}.[34] In this regard, AgNCs already have silver ions in their composition and can therefore act as antibacterial agents. Furthermore, the ratio of Ag^{+}/Ag^{0} can modulate the antibacterial activity of AgNCs. It is tempting to suggest that the increased number of silver ions in AgNCs may explain higher antibacterial activity. However, C9 is dominated by “green” emitting species which would supposedly have the highest number of cations in the AgNC composition, while we observe that C9 has the lowest antibacterial effect. It is possible that the looped hairpin templates used herein while varying in the length may have different protective properties for AgNCs depending on the final conformation of the loop wrapping around silver clusters. For example, faster conversion of C11 to “orange” emitting species might indicate lesser protection of the clusters and thus correlate better with higher antibacterial activity of C11. Additional studies will be required to identify whether intact DNA-AgNCs act as the antibacterial agent or if their activity requires nanocluster dissolution with the release of silver ions into the solution.

Another possible explanation for different activities observed for the four samples studied is that the nature of emissive and non-emissive states may be important. We observed that all four samples age and react with H_2O_2 very differently. It is also apparent that partial oxidation is involved in “red” to “orange” or “red” to “green” conversion of emissive AgNC states. We have evaluated the rate of “red” peak conversion as a function of H_2O_2 concentration (Figure 5) for all four C_N-AgNCs using a modified Stern-Volmer relationship.[35]

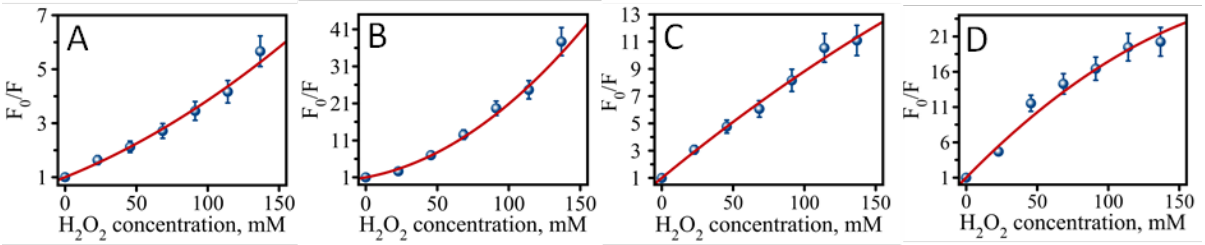

Figure 5. Stern-Volmer plots for (A) C7 – AgNC, (B) C9 – AgNC, (C) C11 – AgNC, (D) C13 – AgNC. Data points were fitted with equation 1 which considers two possible quenching mechanisms: static and dynamic.

Generally, a linear Stern-Volmer plot indicates a single class of fluorophores which are all equally vulnerable to quenching by H_2O_2.[35] All four AgNC samples show non-linear F_0/F vs C_{H2O2} dependence (Figure 5), suggesting a complex nature of fluorescence quenching with at least two deactivation pathways: intermolecular quenching due to H_2O_2 (dynamic quenching, K_D, most likely due to intersystem crossing from singlet S* to triplet T*) and intramolecular conversion of "red" to "orange" or "green" (static quenching, K_S, due to change of the overall charge state of AgNC). While C7 and C9 exhibit slightly upward curvature, C11 and C13 show clear downward curvature. This observation indicates that these two groups have different mechanisms of quenching while interacting with H_2O_2. Typically, downward curvature is associated with fluorophores which are inaccessible to the quencher, suggesting a more protective nature of larger loops.[35] Interestingly, C11 and C13 also show higher antibacterial activity. While it is difficult to specify exact details of interactions between the "quencher" and certain states of AgNCs without further studies, it is apparent that the charge state of the AgNC can play a critical role in defining the antibacterial activity of nanoclusters. Several reports have indicated that silver nanoclusters are capable of generating excessive amounts of intracellular reactive oxygen species which is proposed as the major contributing factor defining AgNCs' antibacterial ability.[16, 36] It is also becoming increasingly apparent from recent studies both theoretical[37] and experimental[38] that certain

shape, composition, and charge states of AgNCs can increase the chances of optically “dark” states to exist with high spin multiplicity (doublet and triplet). Therefore, it is not unreasonable to propose that high spin AgNC states may interact with highly abundant triplet oxygen removing the "spin-forbidden" condition and stimulating the transition of triplet to singlet oxygen: $^{3}O_2 \rightarrow {}^{1}O_2$. Since singlet oxygen is far more reactive compared to triplet oxygen, this can explain various antibacterial properties of different AgNCs and the generation of reactive oxygen species.

In conclusion, nucleic acid-based nanomaterials are often designed based on two rationales: the delivery of functional moieties which can be implemented into the nanoscaffolds and the patterns in recognition of nucleic acids which contribute to the cellular response. DNA-templated AgNCs offer an approach by which functional fluorescent moieties can contribute to selective growth inhibition of bacterial culture. The results of this study suggest that the rich optical behavior of the AgNCs is tightly linked to the antibacterial properties of this novel class of nanostructures. Multiple emission peaks, their interconversion, and connection with environmental changes are the keys to understanding the mechanism of AgNC inhibitive action. The results obtained herein warrant further exploration of the antimicrobial effects of DNA-templated AgNCs on both pathogenic and non-pathogenic bacteria species.

4.4 Materials and Methods

4.4.1 Synthesis of DNA-AgNCs

All DNA oligonucleotides were purchased from Integrated DNA Technologies (IDT), Inc. (Coralville, IA, USA) as desalted products and used without further purification. All sequences are listed in the Supporting Information. Nuclease-free water was obtained from

IDT. Sodium borohydride was purchased from TCI America, Inc. In a typical preparation, DNA template (C13, C11, C9, or C7) and $AgNO_3$ aqueous solutions were mixed and incubated for 25 min at room temperature in ammonium acetate buffer (100 mM NH_4OAc , pH 6.9). Next, $NaBH_4$ aqueous solution was added and samples were placed on ice and stirred vigorously. The final concentrations (C) of the components were as follows: $C_{DNA\text{-}template}$ = 50 μM; C_{AgNO3} was adjusted to match the number of cytosines in the loop according to n*$AgNO_3$:C_n;C_{NaBH4}:C_{AgNO3} was taken at 1:1 ratio and C_{NH4Ac} = 4 mM. The solution was then incubated in the dark for 24 h at 4°C. Synthesized DNA-AgNCs were then purified *via* a NAP-5 (Cytiva) filtration gel column purchased from Sigma-Aldrich, Inc. for fluorescence measurements. Purification was performed according to the protocol supplied by the manufacturer. Final concentrations of DNA-AgNC obtained after filtration varied between 8 – 15 μM and were evaluated by taking DNA absorption at 265 nm wavelength. For antibacterial and mammalian cell viability experiments, DNA-AgNCs were purified using 3 kDa Amicon centrifugal filters by washing twice with buffer and diluting to 50 μM DNA-AgNC.

4.4.2 Fluorescence measurements

The excitation and emission spectra were acquired on a Duetta – Fluorescence and Ab-sorbance Spectrometer (Horiba, Inc., Chicago, IL, USA). In all the measurements, the con-centration of the templating sequence was kept the same at ~6 μM. Fluorescence meas-urements were carried out in a Sub-Micro Fluorometer Cell, model 16.40F-Q-10 (from StarnaCells, Inc., Atascadero, CA, USA) at room temperature of ~22 °C. The excitation–emission matrix spectra (EEMS) were recorded with 0.5 nm resolution. Fluorescence spec-tra were recorded with the emission wavelength range from 300 nm to 1000 nm, the initial

excitation wavelength was set to 280 nm, and the final excitation wavelength was set to 800 nm with an increment of 0.5 nm. Matrix data were then used for 2D contour plot using MagicPlot Pro software.

4.4.3 Bacterial growth assays

TOP10F' *E. coli* were purchased from ThermoFisher Scientific and grown in Luria broth (LB) purchased from Sigma. Where shown, the pH of LB was adjusted to pH 5.5 with 100 mM 2-morpholin-4-ylethanesulfonic acid (MES). *E. coli* were grown in LB from single colonies while shaking at 200 rpm at 37 °C in a GeneMate Incubated Shaker. For treatment with AgNCs, bacteria were diluted in LB to an optical density at 600 nm (OD_{600}) of 0.018-0.020. Next, 50 μL of diluted bacteria were added to each well of a 96-well flat-bottom black-walled plate. Purified DNA-AgNCs were added with LB to reach a final volume of 100 μL in each well with 4 μM final concentration of AgNC. Carbenicillin was used as a positive control at a final concentration of 50 μg/mL (132 μM). The lids of the plates were hydrophobically treated by filling them with 10 mL of 20% ethanol, 0.05% Triton X-100 for 30 seconds.[39] The excess liquid was drained, and the lid was leaned against the back of a fume hood to dry for 30 minutes.[39] The lids were parafilmed to the microwell plates to prevent excess evaporation. Microplate optical density measurements were recorded using a Tecan Spark microwell plate reader. The plates were shaken for 30 seconds between each measurement and were incubated at 37 °C with OD_{600} measurements taken every 15 minutes over 20 hours. A minimum of six technical repeats and two biological repeats of each experiment were performed. The time required for each growth curve to reach half its maximum optical density, $t_{1/2}$, was calculated with GraphPad Prism 9 using a non-linear fit of the data. The difference between the untreated control $t_{1/2}$ and the treatment $t_{1/2}$ is reported as

$\Delta t_{1/2}$. Additional experiments in *Lactobacillus* cultures were conducted to understand the effects of DNA-AgNCs on normal microflora (Supporting Information).

4.4.4 Mammalian cell viability assays

For all experiments, cells were maintained and cultured at 37°C, 5% CO_2. THP1-Dual™ cells were purchased from InvivoGen and were maintained in RPMI 1640, 2 mM L-glutamine, 25 mM HEPES, 10% heat-inactivated fetal bovine serum (FBS), and PenStrep (100 U/mL,100 μg/mL). 293FT cells were cultured in DMEM, 2 mM L-glutamine, 10% FBS, and PenStrep (100 U/mL, 100 μg/mL). Jurkat cells were cultured in RPMI 1640, 2 mM L-glutamine, 25 mM HEPES, 10% FBS, and PenStrep (100 U/mL,100 μg/mL). For cell viability studies, cells were plated in a 96-well flat-bottom plate at a density of 40,000 cells per well along with DNA-AgNC solution at final concentrations of 4, or 8 μM and final well volumes of 100 μL. After incubation with AgNC treatments for 20 hours, 20 μL of CellTiter 96® AQueous One Solution Cell Proliferation Assay (MTS) were added to each well. Plates were incubated for an additional 75 minutes at 37 °C, 5% CO_2. The plates were then read on a Tecan Spark microplate reader for absorbance at 490 nm. Sixteen reads per well were averaged for each value.

4.4.5 Scanning electron microscopy (SEM) and energy-dispersive x-ray spectroscopy (EDS)

Solutions of 50μM C9 and C11, in buffer, were pipetted on a polished silicon wafer as 10 μL droplets. Droplets were allowed to dry in a covered petri dish overnight at room temperature. The solid residue was analyzed with SEM/EDS to determine the atomic ratio between P and Ag. Dried solutions on the Si substrate were analyzed with a JEOL JSM-6480 SEM. Micrographs were taken in secondary electron mode with an accelerating voltage of

5kV. EDS spectra were collected using an Oxford Instruments INCA EDS behind a beryllium window. Atomic percentages were calculated by the INCA instrument software from P Kα (2.013 keV) and Ag Lα (2.984 keV) characteristic x-rays.

4.4.6 Statistical analysis

All data is presented as the mean ± standard error of the mean (SEM) for a minimum of N=3 independent biological replicates. For statistical analysis, a one-way ANOVA was performed, followed by a t-test using GraphPad Prism 9.0.0 for Windows, GraphPad Software, San Diego, California USA, www.graphpad.com. P-values of $p<0.05$ were considered statistically significant.

4.5 References

1. Ritchie, Caroline M.; Johnsen, Kenneth R.; Kiser, John R.; Antoku, Yasuko; Dickson, Robert M.; Petty, Jeffrey T. Ag Nanocluster Formation Using a Cytosine Oligonucleotide Template. *The Journal of Physical Chemistry C* **2007**, *111* (1), 175-181. DOI: 10.1021/jp0648487.

2. Petty, Jeffrey T.; Zheng, Jie; Hud, Nicholas V.; Dickson, Robert M. DNA-Templated Ag Nanocluster Formation. *Journal of the American Chemical Society* **2004**, *126* (16), 5207-5212. DOI: 10.1021/ja031931o.

3. Chandler, Morgan; Shevchenko, Oleg; Vivero-Escoto, Juan L.; Striplin, Caryn D.; Afonin, Kirill A. DNA-Templated Synthesis of Fluorescent Silver Nanoclusters. *Journal of Chemical Education* **2020**, *97* (7), 1992-1996. DOI: 10.1021/acs.jchemed.0c00158.

4. New, S. Y.; Lee, S. T.; Su, X. D. DNA-templated silver nanoclusters: structural correlation and fluorescence modulation. *Nanoscale* **2016**, *8* (41), 17729-17746. DOI: 10.1039/c6nr05872h From NLM.

5. O'Neill, Patrick R.; Gwinn, Elisabeth G.; Fygenson, Deborah Kuchnir. UV Excitation of DNA Stabilized Ag Cluster Fluorescence via the DNA Bases. *The Journal of Physical Chemistry C* **2011**, *115* (49), 24061-24066. DOI: 10.1021/jp206110r.

6. Lee, Tae-Hee; Gonzalez, Jose I.; Zheng, Jie; Dickson, Robert M. Single-Molecule Optoelectronics. *Accounts of chemical research* **2005**, *38* (7), 534-541. DOI: 10.1021/ar040146t.

7. Gwinn, E. G; O'Neill, P.; Guerrero, A. J; Bouwmeester, D.; Fygenson, D. K. Sequence-Dependent Fluorescence of DNA-Hosted Silver Nanoclusters. *Advanced Materials* **2008**, *20* (2), 279-283. DOI: 10.1002/adma.200702380.

8. Gwinn, Elisabeth; Schultz, Danielle; Copp, Stacy; Swasey, Steven. DNA-Protected Silver Clusters for Nanophotonics. *Nanomaterials* **2015**, *5* (1), 180-207. DOI: 10.3390/nano5010180.

9. Yin, Na; Yuan, Shuai; Zhang, Man; Wang, Jingyi; Li, Ye; Peng, Yuan; Bai, Jialei; Ning, Baoan; Liang, Jun; Gao, Zhixian. An aptamer-based fluorometric zearalenone assay using a lighting-up silver nanocluster probe and catalyzed by a hairpin assembly. *Microchimica Acta* **2019**, *186* (12). DOI: 10.1007/s00604-019-3984-6.

10. Afonin, Kirill A.; Schultz, Danielle; Jaeger, Luc; Gwinn, Elisabeth; Shapiro, Bruce A. Silver Nanoclusters for RNA Nanotechnology: Steps Towards Visualization and Tracking of RNA Nanoparticle Assemblies. Springer New York, 2015; pp 59-66.

11. Afonin, Kirill A.; Dobrovolskaia, Marina A.; Church, George; Bathe, Mark. Opportunities, Barriers, and a Strategy for Overcoming Translational Challenges to Therapeutic Nucleic Acid Nanotechnology. *ACS Nano* **2020**, *14* (8), 9221-9227. DOI: 10.1021/acsnano.0c04753 (acccessed 2021-01-04T20:59:11).

12. Feng, Q. L.; Wu, J.; Chen, G. Q.; Cui, F. Z.; Kim, T. N.; Kim, J. O. A mechanistic study of the antibacterial effect of silver ions on Escherichia coli and Staphylococcus aureus. *Journal of Biomedical Materials Research* **2000**, *52* (4), 662-668. DOI: https://doi.org/10.1002/1097-4636(20001215)52:4<662::AID-JBM10>3.0.CO;2-3 (acccessed 2020/12/05).

13. Sondi, I.; Salopek-Sondi, B. Silver nanoparticles as antimicrobial agent: a case study on E-coli as a model for Gram-negative bacteria. *Journal of Colloid and Interface Science* **2004**, *275* (1), 177-182, Article. DOI: 10.1016/j.jcis.2004.02.012.

14. Morones, J. R.; Elechiguerra, J. L.; Camacho, A.; Holt, K.; Kouri, J. B.; Ramirez, J. T.; Yacaman, M. J. The bactericidal effect of silver nanoparticles. *Nanotechnology* **2005**, *16* (10), 2346-2353, Article. DOI: 10.1088/0957-4484/16/10/059.

15. Banerjee, Indrani; Pangule, Ravindra C.; Kane, Ravi S. Antifouling Coatings: Recent Developments in the Design of Surfaces That Prevent Fouling by Proteins, Bacteria, and Marine Organisms. *Advanced Materials* **2011**, *23* (6), 690-718. DOI: 10.1002/adma.201001215.

16. Javani, Siamak; Lorca, Romina; Latorre, Alfonso; Flors, Cristina; Cortajarena, Aitziber L.; Somoza, Álvaro. Antibacterial Activity of DNA-Stabilized Silver Nanoclusters Tuned by Oligonucleotide Sequence. *ACS applied materials & interfaces* **2016**, *8* (16), 10147-10154. DOI: 10.1021/acsami.6b00670.

17. Yang, Lu; Yao, Chi; Li, Feng; Dong, Yuhang; Zhang, Zhikun; Yang, Dayong. Synthesis of Branched DNA Scaffolded Super-Nanoclusters with Enhanced Antibacterial Performance. *Small (Weinheim an der Bergstrasse, Germany)* **2018**, *14* (16), 1800185, https://doi.org/10.1002/smll.201800185. DOI: https://doi.org/10.1002/smll.201800185 (acccessed 2020/12/05).

18. Eun, Hyunmin; Kwon, Woo Young; Kalimuthu, Kalishwaralal; Kim, Yonghwan; Lee, Miran; Ahn, Jung-Oh; Lee, Hongweon; Lee, Sang Hyun; Kim, Hyung Joo; Park, Hyun Gyu; et al. Melamine-promoted formation of bright and stable DNA–silver nanoclusters and their antimicrobial properties. *Journal of Materials Chemistry B* **2019**, *7* (15), 2512-2517, 10.1039/C8TB03166E. DOI: 10.1039/C8TB03166E.

19. Sengupta, Bidisha; Sinha, Sudarson Sekhar; Garner, Bianca L.; Arany, Istvan; Corley, Christa; Cobb, Keith; Brown, Elrica; Ray, Paresh Chandra. Influence of Aptamer-Enclosed Silver Nanocluster on the Prevention of Biofilm by <I>Bacillus thuringiensis</I>. *Nanoscience and Nanotechnology Letters* **2016**, *8* (12), 1054-1060. DOI: 10.1166/nnl.2016.2243.

20. Panigaj, M.; Johnson, M. B.; Ke, W.; McMillan, J.; Goncharova, E. A.; Chandler, M.; Afonin, K. A. Aptamers as Modular Components of Therapeutic Nucleic Acid Nanotechnology. *ACS Nano* **2019**, *13* (11), 12301-12321. DOI: 10.1021/acsnano.9b06522.

21. Yourston, L. E.; Lushnikov, A. Y.; Shevchenko, O. A.; Afonin, K. A.; Krasnoslobodtsev, A. V. First Step Towards Larger DNA-Based Assemblies of Fluorescent

Silver Nanoclusters: Template Design and Detailed Characterization of Optical Properties. *Nanomaterials (Basel)* **2019**, *9* (4). DOI: 10.3390/nano9040613.

22. Guo, Yahui; Shen, Fumiao; Cheng, Yuliang; Yu, Hang; Xie, Yunfei; Yao, Weirong; Pei, Renjun; Qian, He; Li, Hung-Wing. DNA-Hairpin-Templated Silver Nanoclusters: A Study on Stem Sequence. *The Journal of Physical Chemistry B* **2020**. DOI: 10.1021/acs.jpcb.9b09741.

23. Ramsay, H.; Simon, D.; Steele, E.; Hebert, A.; Oleschuk, R. D.; Stamplecoskie, K. G. The power of fluorescence excitation–emission matrix (EEM) spectroscopy in the identification and characterization of complex mixtures of fluorescent silver clusters. *RSC Advances* **2018**, *8* (73), 42080-42086, 10.1039/C8RA08751B. DOI: 10.1039/C8RA08751B.

24. Yourston, Liam; Rolband, Lewis; Lushnikov, Alexander; West, Caroline; Afonin, Kirill; Krasnoslobodtsev, Alexey. Tuning properties of silver nanoclusters with RNA nanoring assemblies. *Nanoscale* **2020**, 10.1039/D0NR03589K. DOI: 10.1039/D0NR03589K.

25. Yourston, L. E.; Krasnoslobodtsev, A. V. Micro RNA Sensing with Green Emitting Silver Nanoclusters. *Molecules* **2020**, *25* (13). DOI: 10.3390/molecules25133026.

26. Petty, Jeffrey T.; Sergev, Orlin O.; Kantor, Andrew G.; Rankine, Ian J.; Ganguly, Mainak; David, Frederic D.; Wheeler, Sandra K.; Wheeler, John F. Ten-Atom Silver Cluster Signaling and Tempering DNA Hybridization. *Analytical Chemistry* **2015**, *87* (10), 5302-5309. DOI: 10.1021/acs.analchem.5b01265.

27. Chaloupka, Karla; Malam, Yogeshkumar; Seifalian, Alexander M. Nanosilver as a new generation of nanoproduct in biomedical applications. *Trends in Biotechnology* **2010**, *28* (11), 580-588. DOI: https://doi.org/10.1016/j.tibtech.2010.07.006.

28. Deshmukh, S. P.; Patil, S. M.; Mullani, S. B.; Delekar, S. D. Silver nanoparticles as an effective disinfectant: A review. *Materials Science and Engineering: C* **2019**, *97*, 954-965. DOI: https://doi.org/10.1016/j.msec.2018.12.102.

29. Cerretani, C.; Vosch, T. Switchable Dual-Emissive DNA-Stabilized Silver Nanoclusters. *ACS Omega* **2019**, *4* (4), 7895-7902. DOI: 10.1021/acsomega.9b00614.

30. Shah, Pratik; Rørvig-Lund, Andreas; Chaabane, Samir Ben; Thulstrup, Peter Waaben; Kjaergaard, Henrik Grum; Fron, Eduard; Hofkens, Johan; Yang, Seong Wook; Vosch, Tom. Design Aspects of Bright Red Emissive Silver Nanoclusters/DNA Probes for MicroRNA Detection. *ACS Nano* **2012**, *6* (10), 8803-8814. DOI: 10.1021/nn302633q.

31. Enkin, Natalie; Wang, Fuan; Sharon, Etery; Albada, H. Bauke; Willner, Itamar. Multiplexed Analysis of Genes Using Nucleic Acid-Stabilized Silver-Nanocluster Quantum Dots. *ACS Nano* **2014**, *8* (11), 11666-11673. DOI: 10.1021/nn504983j.

32. Copp, Stacy M.; Schultz, Danielle; Swasey, Steven; Pavlovich, James; Debord, Mark; Chiu, Alexander; Olsson, Kevin; Gwinn, Elisabeth. Magic Numbers in DNA-Stabilized

Fluorescent Silver Clusters Lead to Magic Colors. *The Journal of Physical Chemistry Letters* **2014**, *5* (6), 959-963. DOI: 10.1021/jz500146q.

33. Weerawardene, K. L. Dimuthu M.; Häkkinen, Hannu; Aikens, Christine M. Connections Between Theory and Experiment for Gold and Silver Nanoclusters. *Annual Review of Physical Chemistry* **2018**, *69* (1), 205-229. DOI: 10.1146/annurev-physchem-052516-050932 (acccessed 2020/04/22).

34. Le Ouay, Benjamin; Stellacci, Francesco. Antibacterial activity of silver nanoparticles: A surface science insight. *Nano Today* **2015**, *10* (3), 339-354. DOI: https://doi.org/10.1016/j.nantod.2015.04.002.

35. Lakowicz, Joseph R. *Principles of fluorescence spectroscopy*; Springer, NY, USA, 2006

36. Yuan, Xun; Setyawati, Magdiel Inggrid; Tan, Audrey Shu; Ong, Choon Nam; Leong, David Tai; Xie, Jianping. Highly luminescent silver nanoclusters with tunable emissions: cyclic reduction–decomposition synthesis and antimicrobial properties. *NPG Asia Materials* **2013**, *5* (2), e39-e39. DOI: 10.1038/am.2013.3.

37. Jabed, M. A.; Dandu, N.; Tretiak, S.; Kilina, S. Passivating Nucleobases Bring Charge Transfer Character to Optically Active Transitions in Small Silver Nanoclusters. *J Phys Chem A* **2020**, *124* (43), 8931-8942. DOI: 10.1021/acs.jpca.0c06974.

38. Krause, Stefan; Cerretani, Cecilia; Vosch, Tom. Disentangling optically activated delayed fluorescence and upconversion fluorescence in DNA stabilized silver nanoclusters. *Chemical Science* **2019**, *10* (20), 5326-5331, 10.1039/C9SC00865A. DOI: 10.1039/C9SC00865A.

39. Brewster, Jeffrey D. A simple micro-growth assay for enumerating bacteria. *Journal of Microbiological Methods* **2003**, *53* (1), 77-86. DOI: 10.1016/s0167-7012(02)00226-9.

4.6 Appendix B: Supporting Information for DNA-templated Fluorescent Silver Nanoclusters Inhibit Bacterial Growth while being Non-toxic to Mammalian Cells

SEQUENCES USED IN THIS PROJECT

All oligonucleotides were purchased from IDT, Inc. Names denote the numbers of cytosines in each hairpin loop, underlined below.[1, 2]

C7: 5'- TATCCGTCCCCCCCACGGATA

C9: 5'- TATCCGTCCCCCCCCCCACGGATA

C11: 5'- TATCCGTCCCCCCCCCCCCACGGATA

C13: 5'- TATCCGTCCCCCCCCCCCCCCACGGATA

From Fig. S1:

C12: 5'- TATCCGTCCCCCCCCCCCCCACGGATA

Single-stranded C12: 5'- CCCCCCCCCCCC

SUPPORTING METHODS

Bacterial growth of Lactobacilli *on LB agar.* One colony with the morphology of *Lactobacilli* was isolated from 1:100 and 1:1000 dilutions of Bulgarian yogurt (White Mountain) tested on LB agar plates in duplicate and was inoculated into SOS medium (Invitrogen) to prepare a pure culture. The culture was incubated at 42-45 °C for 36 hours to produce a turbid culture. A 100 µL aliquot of this culture was transferred into fresh SOS medium and again incubated at 42-45 °C for 36 hours to adapt *Lactobacilli* to SOS medium.

This culture was then used for all subsequent experiments and was stored at 4 °C between experiments to prevent bacterial cells from proliferating. Each DNA-templated AgNC (C7, and C9) was mixed with liquid *Lactobacilli* culture in SOS media so that the final dilutions of bacteria were 1:1000 and 1:10,000 with nanoclusters at the final concentration of 22.5 μM of silver in 100 μL. From this, 25 μL of each sample was plated per one quarter of an LB agar plate; two replicates per sample were tested. Plates were incubated at 42-45 °C for 36 hours, then individual colonies were counted.

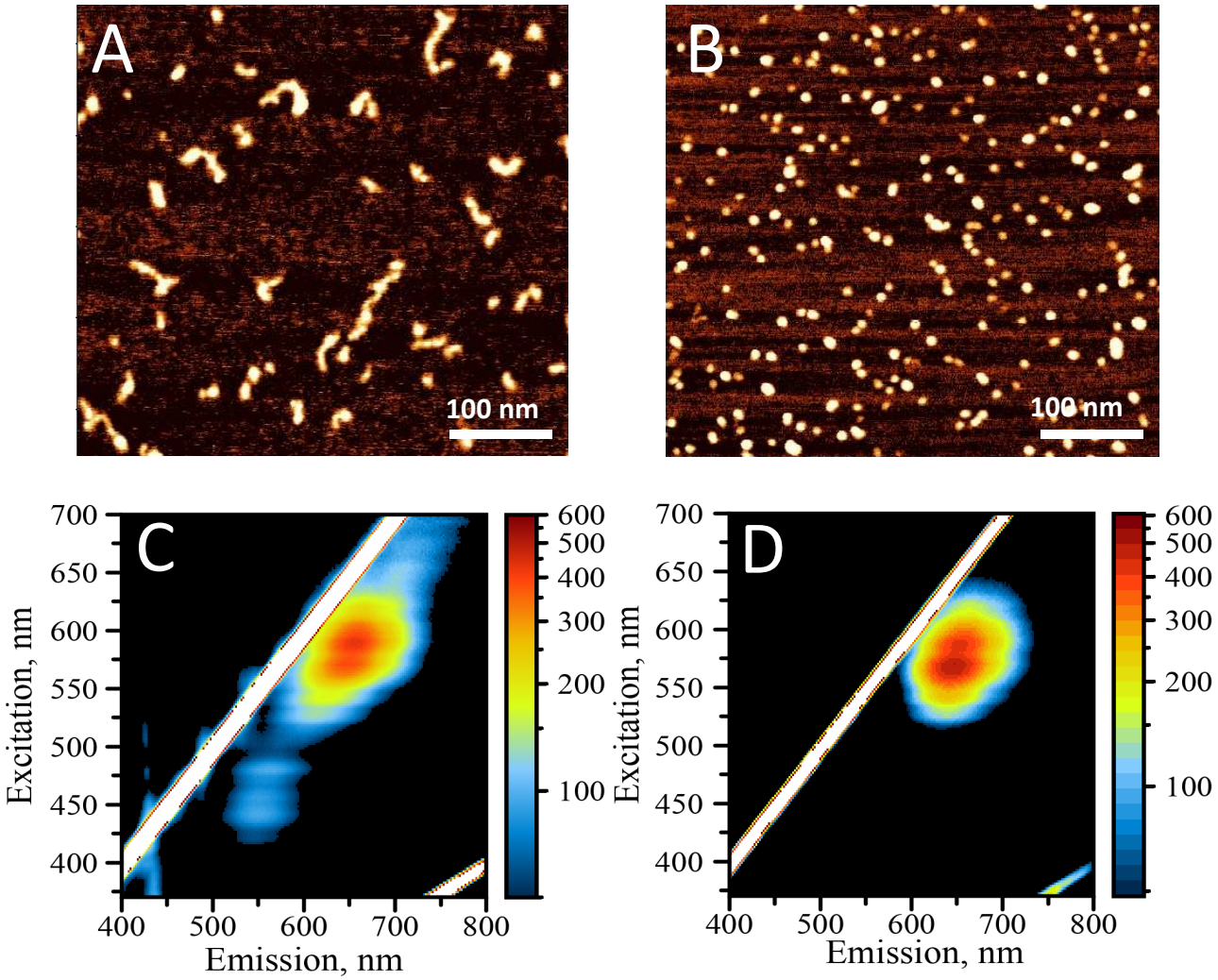

SI Figure S1. Comparison of C12 template as a single-stranded nucleotide or as a loop in a hairpin structure. (A) AFM image of AgNCs formed on a template containing single-stranded C12 sequence, (B) AFM image of AgNCs formed on a template containing C12 loop, (C) EEM of AgNCs templated on a template containing single-stranded C12 sequence, (D) EEM of AgNCs templated on a template containing C12 loop.

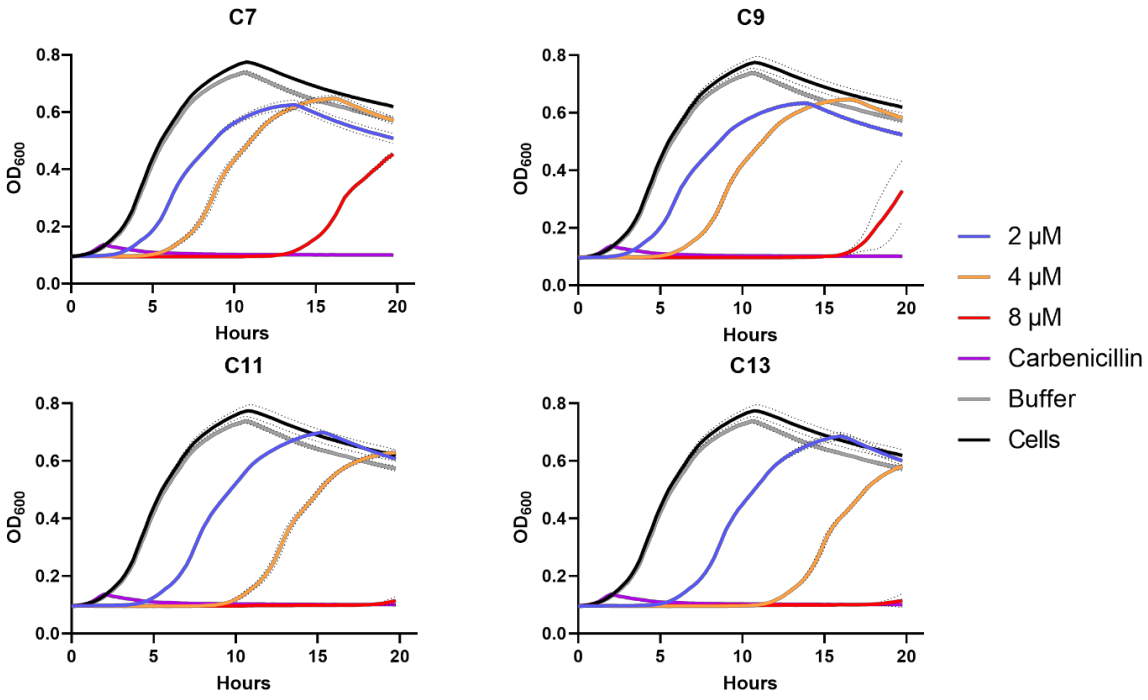

SI Figure S2. Liquid culture growth curves are shown of E. coli which have been treated with varying concentrations of AgNC. Each is shown with the standard deviation as a dotted line on either side of the solid line in the same color. There is a strong dose-dependence for each AgNC with 8 µM C11 eliminating growth for almost the full 20 hours.

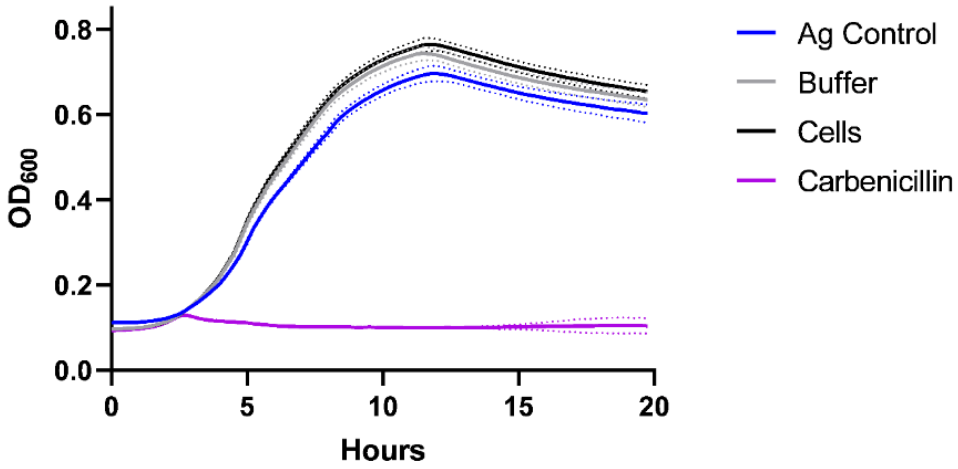

SI Figure S3. To see the effects of free silver that may not have bound to DNA, 650 µM $AgNO_3$ solution was reduced with an equimolar amount of NaBH4, just as in the synthesis of the C13 AgNC. E. coli was then treated with the same amount of this solution as would be present in 4 µM C13 AgNC treatments. While there was a slight reduction in growth rate and the maximum OD600, these were minimal compared to the effects of the C13 AgNC at 4 µM.

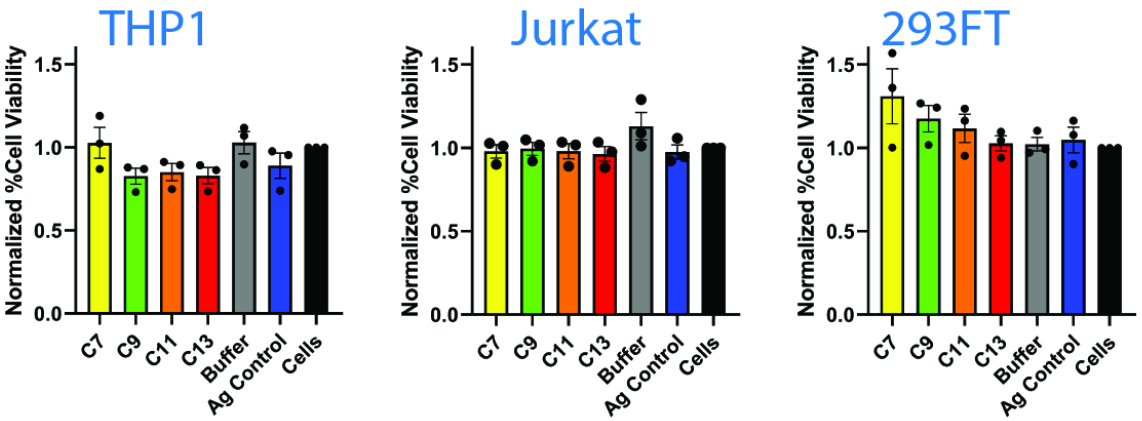

SI Figure S4. Additional mammalian cell viability assays were conducted with 8 µM AgNC concentrations following the methods described in the main text. Following 20 hours of incubation at 37 °C and 5% CO_2, MTS was added and incubated for an additional 75 minutes at the same conditions. The absorbance was recorded at 490 nm and the relative cell viability was calculated. No statistically significant reduction in cell viability was found at the elevated AgNC conditions.

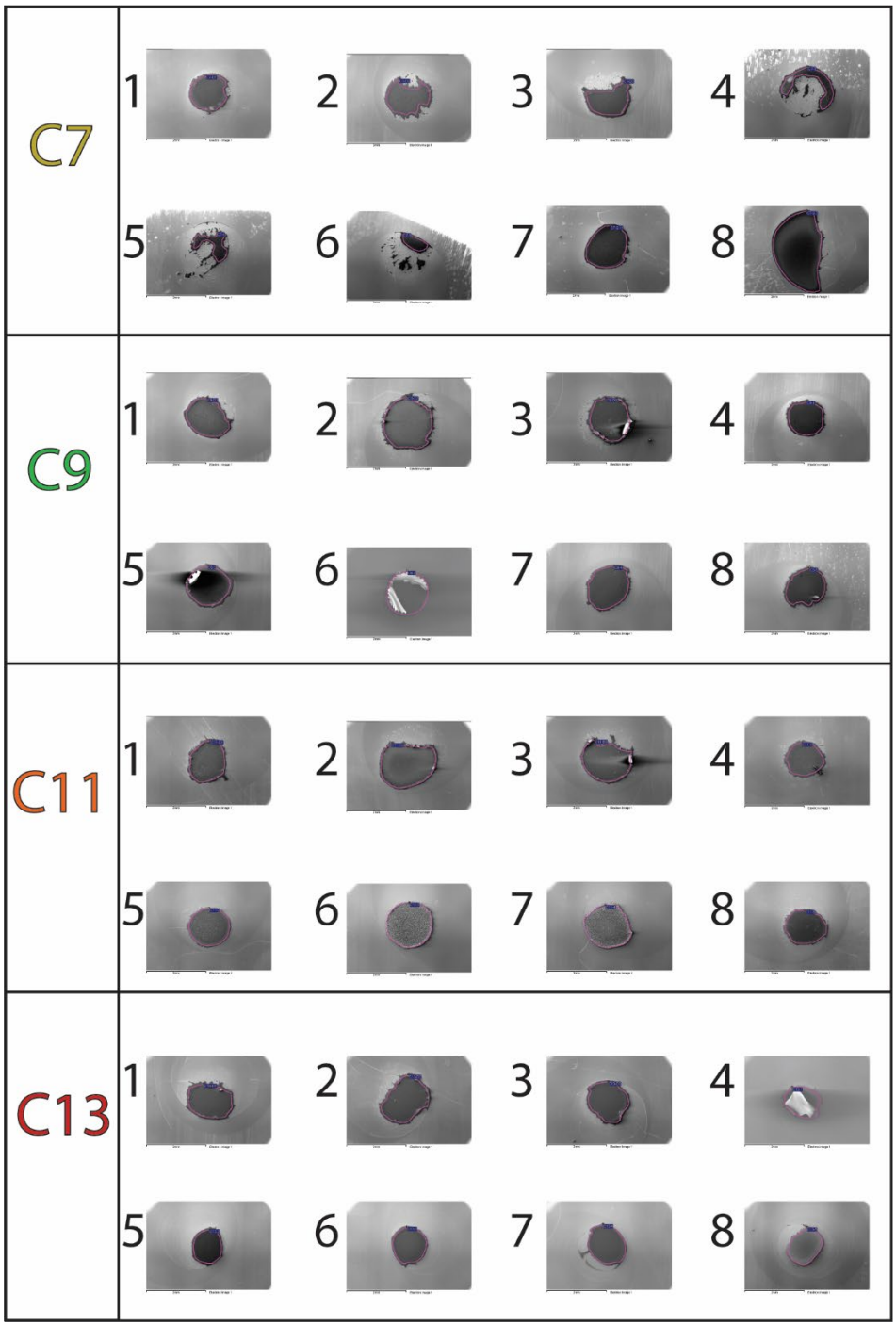

SI Figure S5. Secondary electron micrographs of all of the dried AgNC samples which were used for the stoichiometry calculations are shown.

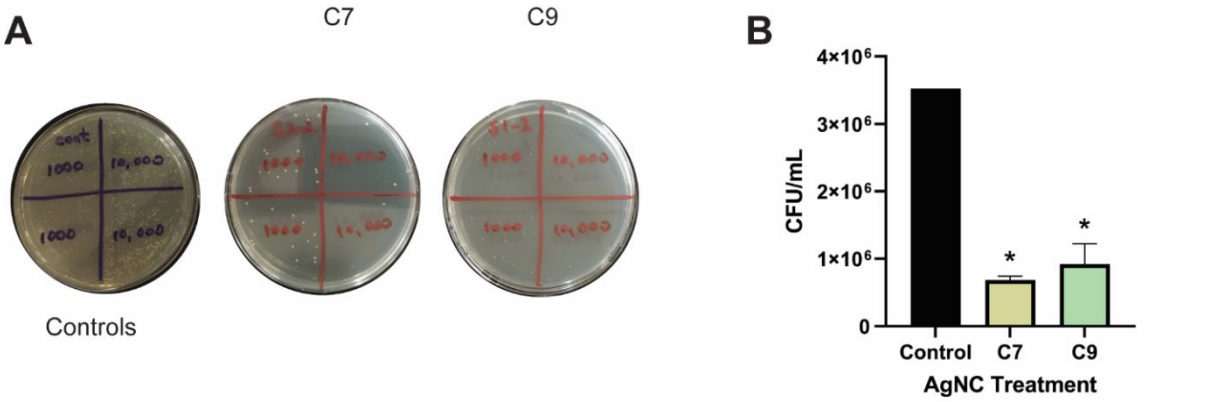

SI Figure S6. (A) Plates of Lactobacilli treated with C7 or C9 AgNCs and the resulting colonies formed. (B) Colony forming units (CFU)/mL after treatment with C7 or C9 were compared to the control sample Significance of $p<0.05$ is denoted with an asterisk.

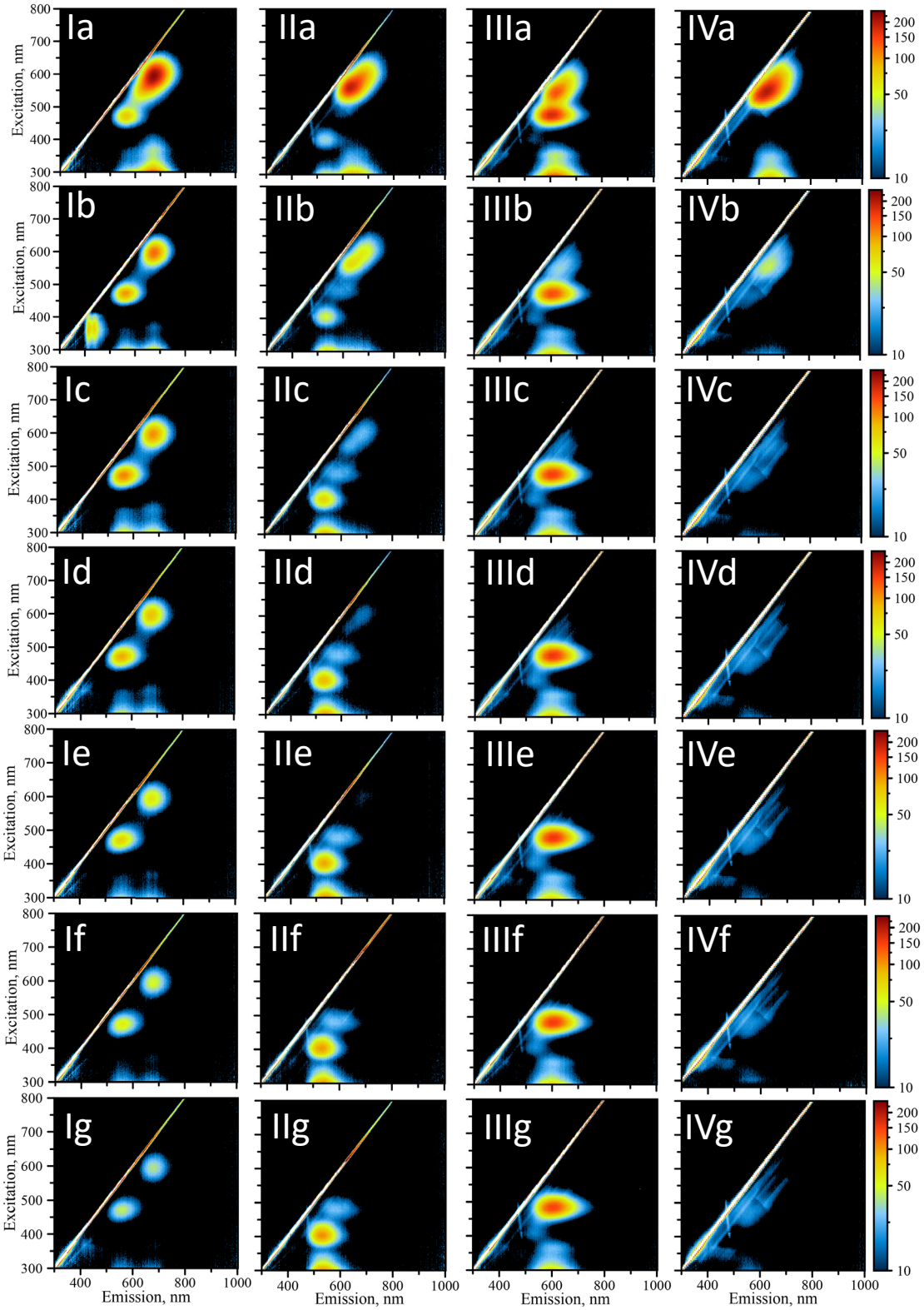

SI Figure S7. Titration of AgNCs with hydrogen peroxide. I) C7 DNA-AgNCs, II) C9 DNA-AgNCs, III) C11 DNA-AgNCs, IV) C13 DNA-AgNCs. Progressive addition of hydrogen peroxide shows changes in oxidative state of DNA-AgNCs. (a-f) are different ratios of $C_{AgNC}/C_{H_2O_2}$ = 1/0 (a), 1/1.9 (b), 1/3.8 (c), 1/5.7 (d), 1/7.6 (e), 1/9.5 (f), 1/11.4 (g).

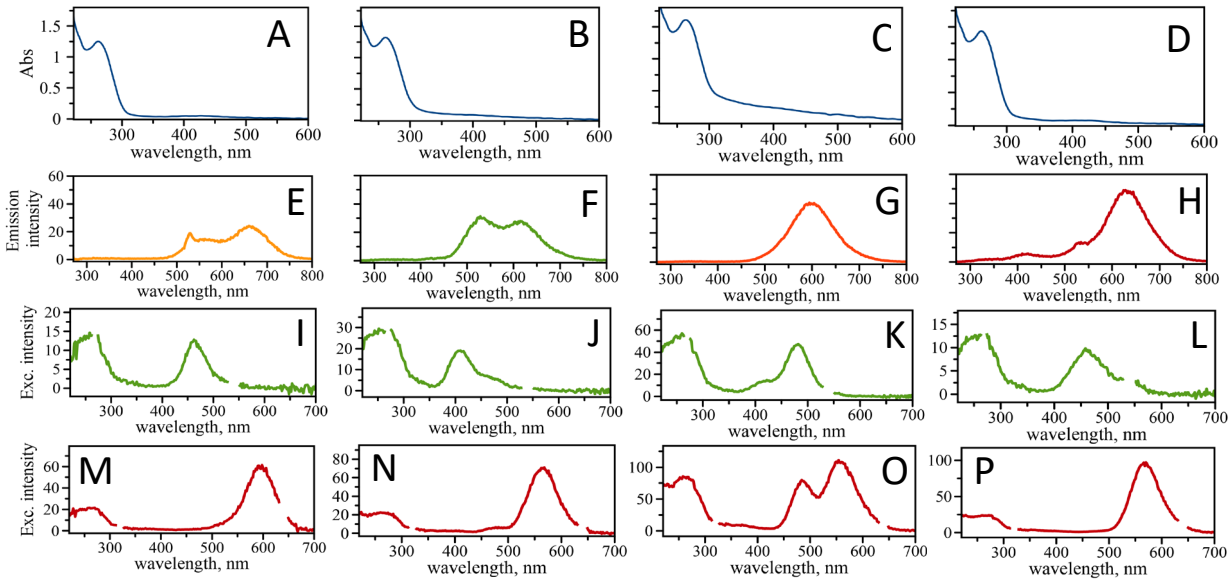

SI Figure S8. Evaluation of optical properties. UV-Vis spectra of A) C7, B) C9, C) C11, D) C13 samples immediately after purification. Emission spectra with 254 nm excitation mimicking color observation shown in Figure 1, E) C7, F) C9, G) C11, H) C13. Excitation spectra for 525 nm emission peak, I) C7, J) C9, K) C11, L) C13. Excitation spectra for 635 nm emission peak, M) C7, N) C9, O) C11, P) C13.

SI Table S1. The calculated number of silver atoms from the atomic percentages obtained from the EDS reports are shown with the average and standard error of the mean for each AgNC.

	1	2	3	4	5	6	7	8	Mean		SEM
C7	11.3	11.5	9.7	12.3	8.3	9.2	8.0	8.7	9.9	±	0.6
C9	10.2	7.9	11.4	7.4	7.8	7.6	8.0	7.7	8.5	±	0.5
C11	11.4	9.8	14.0	11.2	13.6	10.8	11.8	11.4	11.7	±	0.5
C13	11.3	13.3	10.9	8.0	7.5	7.9	8.7	13.7	10.2	±	0.9

Supporting References

1. O'Neill, Patrick R.; Gwinn, Elisabeth G.; Fygenson, Deborah Kuchnir. UV Excitation of DNA Stabilized Ag Cluster Fluorescence via the DNA Bases. *The Journal of Physical Chemistry C* **2011**, *115* (49), 24061-24066. DOI: 10.1021/jp206110r.

2. O'Neill, Patrick R.; Velazquez, Lourdes R.; Dunn, Donald G.; Gwinn, Elisabeth G.; Fygenson, D. Kuchnir. Hairpins with Poly-C Loops Stabilize Four Types of Fluorescent Agn:DNA. *The Journal of Physical Chemistry C* **2009**, *113* (11), 4229-4233. DOI: 10.1021/jp809274m.

5 CHAPTER 5: CONCLUSIONS

The work presented here presents a contribution to the field of nucleic acid nanotechnology through the propagation of knowledge, offering of ideas to contribute versatility, and optimization of molecular function to project the value of the field. NANPs are a worthy candidate for investment because of their impressive list of applications. Their biocompatibility, programmability, molecular precision, and reproducibility make them a very powerful tool for manipulating molecular systems. The list of TNAs approved by the FDA increases as their value is realized and developed. NANPs are the next generation of TNAs because their structure enables programmability. As a scaffold and as a functional agent, NANPs offers precision in structure design, functionalization choice, and degree of immune stimulation. Nucleic acid is utilized by cells as a highly dynamic material to carry out molecular functions. Utilizing the same material for therapeutic use is an avenue towards great potential. More versatile therapeutics are coming because the promise of improving medicine is becoming more evident. Although the purpose of NANPs is very clinically relevant, safety concerns regarding TNAs impedes important clinically relevant research and approval. It is essential for the success of the field to prove functional nucleic acids perform more good than harm. The most opportune approach to maximize the value of NANPs is diversifying available functions and fine tuning those functions.

In the first study, a review of the field of nucleic acid nanotechnology is presented. Current research encompasses a variety of functional nucleic acids and related nanotechnology topics. Research ranged from mechanistic studies and fundamental science to translational research actively implemented. Mechanosensing is described in the study of NompC, an ion channel that helps a cell sense mechanical change. The mechanism of a

molecular motors is discussed in relation to genome packaging. Nanopores were demonstrated as a novel method to identify proteins in solutions relevant to clinical samples. Computational approaches are able to achieve atomic resolution in determining catalytic and selectivity mechanisms of enzymes. Ribosomal frameshifting is studied and discussed as a potential target for antiviral applications include SARS-CoV-2. Computational prediction of RNA structure is approached by processing large amounts of experimental data with a deep learning model to improve secondary structure prediction. CryoEM was used to reveal high resolution details to explain RNA structures that regulate viral processes. Structure determination of RNA nanoparticles and RNA native structures was improved by combining SAXS data with computational methods. Strand displacement in DNA/RNA hybrids were systematically studied with experimental methods varying concentrations and mismatches. This review reiterates the potential of functional RNA and shares ideas in the field.

The study in chapter 3 introduces a novel phenomenon of NANP assembly by nuclease treatment. RNA/DNA hybrid duplexes were treated with substrate specific nucleases. The selective degradation allowed self-assembly of structures from the liberated monomers. Successful restructuring of duplexes to NANPs was confirmed by EMSA and AFM. Composition was confirmed by a selective degradation assay. Digestion and assembly kinetics during nuclease treatment was assessed by EMSA and quantitative image analysis. Shelf stability of NANPs was determined by rehydration after storage. EMSA confirmed the integrity of duplexes and showed the degradation of cubes. This also implied the improved storage capabilities enabled by the enzyme drive assembly method. A single long hybrid duplex structure was designed to hold RNA cube monomers with DNA holding strands. This system was confirmed to assemble cube structures after DNase treatment. Finally immune

recognition was assessed in HEK-Blue and HEK-Lucia cell lines after enzyme treatment. The results confirmed the expected immune response corresponding to previous work. This implies the ability to control the degree of immune response by nuclease. The results of this investigation offer a controllable reassociation feature for future therapeutic platforms.

The final study introduces and characterizes a novel antibacterial structure. DNA templates with repeating cytosine bases were used to synthesize AgNCs. Number of cytosines were varied to determine the dependence of the AgNC properties. EEMS confirmed expected optical properties with the literature. Cell culture experiments showed no significant effect on cell viability in mammalian cells and significant growth inhibition in e coli. There is potential for use as an antibiotic treatment. A novel method based on EDS was developed to determine the stochiometric ratio between the template and AgNC size. This information was used to determine the size of the AgNC and confirmed that our structures were consistent with the literature. The DNA template of this assembly will be compatible with NANP systems through a toehold interaction. The result of antibacterial properties would make this structure a viable moiety for NANPs and other compatible systems.

This combined work here aims to diversify and improve the functional options for nucleic acid-based therapeutics. A NANP based approach was chosen because of the advantages these structures offer. Their ration design expands versatility and functionality while characterization ascertains their safety and effectiveness. This trend will continue as the field progresses toward clinical translation of individualized medicine.

Appendix C: Previously published material

This dissertation contains previously published material. Original published articles can be found online.

Chapter 2:

Rolband, L., Beasock, D., Wang, Y., Shu, Y. G., Dinman, J. D., Schlick, T., ... & Afonin, K. A. (2022). *Biomotors, viral assembly, and RNA nanobiotechnology: Current achievements and future directions*. **Computational and Structural Biotechnology Journal**. https://doi.org/10.1021/acs.bioconjchem.3c00167

Chapter 3:

Beasock, D., Ha, A., Halman, J., Panigaj, M., Wang, J., Dokholyan, N. V., & Afonin, K. A. (2023). *Break to Build: Isothermal Assembly of Nucleic Acid Nanoparticles (NANPs) via Enzymatic Degradation*. **Bioconjugate Chemistry**. https://doi.org/10.3390/molecules26134045

Chapter 4:

Rolband, L., Yourston, L., Chandler, M., Beasock, D., Danai, L., Kozlov, S., ... & Afonin, K. A. (2021). *DNA-templated fluorescent silver nanoclusters inhibit bacterial growth while being non-toxic to mammalian cells*. **Molecules**, 26(13), 4045. https://doi.org/10.1016/j.csbj.2022.11.007